UNIVERSITY OF SÃO PAULO
FFCLRP – DEPARTMENT OF PHYSICS
Postgraduate in Applied Physics to Medicine and Biology

SAEIDEH ARSALANI

Multifunctional Nanoparticles for Ultrasound-Guided Theranostic Application

Nanopartículas Multifuncionais para Aplicações Teranósticas Guiadas por Ultrassom

Ribeirão Preto – SP
2023

SAEIDEH ARSALANI

Multifunctional Nanoparticles for Ultrasound-Guided Theranostic Applications

Thesis presented to Faculty of Philosophy, Sciences and Literature of the University of São Paulo, as part of the requirements for degree of Doctor of Sciences.

Concentration area: Physics Applied to Medicine and Biology.

Advisor: Prof. Dr. Antonio Adilton Oliveira Carneiro

Co-Advisor: Prof. Dr. Oswaldo Baffa Filho

Original Version

Available at FFCLRP-USP

Ribeirão Preto – SP

2023

FICHA CATALOGRÁFICA

Arsalani, Saeideh

Nanopartículas Multifuncionais para Aplicações Teranósticas Guiadas por Ultrassom/ Saeideh arsalani; Orientador: Prof. Dr. Antonio Adilton Oliveira Carneiro, Co- orientador: Prof. Dr. Oswaldo Baffa. Ribeirão Preto - SP, 2023.

124 f.:il.

Tese (Doutorado - Programa de Pós-Graduação em Física Aplicada à Medicina e Biologia) - Faculdade de Filosofia, Ciências e Letras de Ribeirão Preto of the Universidade de São Paulo, 2023.

1. Nanopartículas magnéticas. 2. Nanobastões de uro. 3. Magnetoacustografia. 4. Hipertermia magnética. 5. Imagem fotoacústica.

Name: Saeideh Arsalani

Title: Multifunctional Nanoparticles for Ultrasound-Guided Theranostic Applications

Thesis presented to Faculty of Philosophy, Sciences and Literature of the University of São Paulo, as part of the requirements for the degree of Doctor of Sciences.

Approved in: ___/___/___.

Examination Board

Prof. Dr.: _____, Institution: _____

Judgment: _____, Signature: _____

Prof. Dr.: _____, Institution: _____

Judgment: _____, Signature: _____

Prof. Dr.: _____, Institution: _____

Judgment: _____, Signature: _____

Prof. Dr.: _____, Institution: _____

Judgment: _____, Signature: _____

To my beloved parents, my sisters, and my brother for all their love and support

Acknowledgments

First and foremost, I would like to express my special and deepest gratitude to my supervisors Prof. Dr. Antonio Adilton Oliveira Carneiro and Prof. Dr Oswaldo Baffa for their guidance, constant encouragement, mentoring, and kindness. I am very grateful to them for their endless inspiration and generous support, which allowed me to gain invaluable experience during my PhD.

I would also like to give my gratitude to Dr. Éder José Guidelli, Dr. Ana Paula Ramos and Dr. Theo Z Pavan for their great help and valuable advice throughout this project. I learned so much from you.

I am also grateful to all of my colleagues specially Thiago, Pedro, Jose, and Berg at GIIMUS for their constant helpfulness and creating a pleasant and friendly work environment. I would also like to thank Agnelo, our GIIMUS technician, for all of his help and patience during my experiments. I also appreciate Nilza, Raquel, and Gustavo for providing me with all the information and advice I needed at the time.

I am very grateful to my close friend, Yaser who provided significant help during my PhD studies. I am really thankful to him for all of his good vibes, and for our countless talk, not only in academic life but also outside of research. Special thanks to my other great friends, especially my dear Alex, Iara, Kleython, Ricardo, Ernesto, and Emanuel, for their encouragement, kindness, and support throughout my stay in Brazil. You all gave a very unforgettable memory to me.

Finally, I would like to express my heartfelt gratitude to my beloved parents, sisters, and brother for their unending love, patience, encouragement, and inspiration in all aspects of my life. Thank you so much for always being there for me and believing in me to pursue my dreams and achieve my goals, which made the completion of thesis possible. Special thanks to my lovely sister, Sudi, for her love, kindness, caring and encouragement throughout my entire life.

I appreciate the support from the funding agency, Coordenação de Aperfeiçoamento de Pessoal de Nível Superior (CAPES) - Finance Code 001. I should also thank Conselho Nacional

de Desenvolvimento Científico e Tecnológico (CNPq) and Fundação de Amparo à Pesquisa do Estado de São Paulo (FAPESP).

Resumo

Arsalani, Saeideh. **Nanopartículas Multifuncionais para Aplicações Teranósticas Guiadas por Ultrassom.** 2023. 124 f. Tese (Doutorado – Programa de Pós-Graduação em Física Aplicada à Medicina e Biologia) - Departamento de Física da Faculdade de Filosofia, Ciências e Letras de Ribeirão Preto, Universidade de São Paulo, Ribeirão Preto; 2023.

Os materiais em nanoescala têm sido amplamente explorados em várias modalidades de imagem e terapia devido às suas notáveis propriedades físico-químicas. Por exemplo, nanopartículas magnéticas (MNPs) são de grande interesse para uma ampla gama de aplicações biomédicas devido ao seu pequeno tamanho controlável, propriedades magnéticas ajustáveis e biocompatibilidade. Nesta tese, a síntese e caracterização de nanopartículas de óxido de ferro (IONPs) foram realizadas para aplicações biomédicas por meio da rota de coprecipitação otimizada e revestidas por polietileno glicol (PEG) no procedimento de pós-síntese. Verificou-se que ambas IONPs são altamente estáveis, biocompatíveis, de forma relativamente homogênea e livres de agregação para ambos as IONPs. Curiosamente, as IONPs revestidas por PEG exibiram maior magnetização do que as IONPs nus, o que pode ser atribuído à redução da última camada atômica dessas nanopartículas. Adicionalmente, o desempenho de ambos os MNPs foram investigados para aplicações diagnósticas baseado em imagens de ultrassom por magnetomotriz (MMUS) e terapêuticas por hipertermia magnética (MH). De acordo com os resultados, não apenas as IONPs revestidas com PEG, mas também as IONPs nus mostraram um deslocamento induzido quase semelhante no MMUS. No entanto, as IONPs revestidas com PEG demonstraram maior eficiência de aquecimento em comparação com as IONPs nus, o que pode ser atribuído ao tempo de relaxação browniano das MNPs após o revestimento com PEG.

Além disso, uma combinação relativamente simples de nanopartículas de Ci-$MnFe_2O_4$ e nanobastões de ouro revestidas com brometo de cetiltrimetilamônio (CTAB-GNRs) foi sugerida para criar NPs híbridas. Por causa das superfícies de cargas opostas dos CTAB-GNRs e ferrita de manganês, ocorreu uma interação eletrostática, resultando na formação de pequenos nano aglomerados, que aumentaram consideravelmente o contraste de MMUS em relação ao uso apenas de Ci-$MnFe_2O_4$. Assim, para estudos de MH, essas NPs híbridas apresentaram uma taxa

de aquecimento quase semelhante à do Ci-$MnFe_2O_4$ e uma temperatura de equilíbrio foi maior do que apenas com a ferrita de manganês. Além disso, como os GNRs são agentes de contraste promissores em imagens óticas, essas NPs híbridas também foram examinados em imagens fotoacústicas (PA), apresentando um excelente contraste.

Palavras-chave: 1. Nanopartículas magnéticas. 2. Nanobastões de uro. 3. Magnetoacustografia. 4. Hipertermia magnética. 5. Imagem fotoacústica.

Abstract

Arsalani, Saeideh. **Multifunctional Nanoparticles for Ultrasound-guided Theranostic Applications.** 2023. 124 f. Dissertation (D.Sc- Graduate Program in Applied Physics to Medicine and Biology) - Faculty of Philosophy, Sciences and Literature, University of São Paulo, Ribeirão Preto - SP, 2023.

Nanoscale materials have been widely explored in various imaging modalities and therapy due to their remarkable physiochemical properties. For example, magnetic nanoparticles (MNPs) are of great interest for a wide range of biomedical applications owing to their controllable small size, tunable magnetic properties, and biocompatibility. In this thesis, iron oxide nanoparticles (IONPs) were synthesized and characterized, and their potential was investigated in biomedical applications. Firstly, bare IONPs were prepared through an optimized coprecipitation route and coated by polyethylene glycol (PEG) in the post-synthesis procedure. The results showed that both IONPs were highly stable, biocompatible, relatively homogeneous in shape, and free of aggregation. Interestingly, the IONPs coated by PEG exhibited relatively greater magnetization than bare IONPs, which could be attributed to the reduction of surface spine disorder after coating. Moreover, the performance of both MNPs was investigated for diagnostic (magneto-motive ultrasound imaging (MMUS)) and therapeutic (magnetic hyperthermia (MH)) applications. According to the outcomes, PEG-coated IONPs, and bare IONPs showed an almost similar induced displacement within tissue labeled with MNPs in the MMUS. However, IONPs coated with PEG demonstrated higher heating efficiency than the naked IONPs, which could be the due to the Brownian relaxation time of MNPs after PEG coating.

Furthermore, a relatively simple combination of citrate coated manganese ferrite (Ci-$MnFe_2O_4$) and cetyltrimethylammonium bromide coated gold nanorods (CTAB-GNRs) was suggested to create hybrid NPs. Because of the oppositely charged surfaces of CTAB-GNRs and Ci-$MnFe_2O_4$, an electrostatic interaction occurred, resulting in the formation of small nanoclusters, which increased the contrast of MMUS over just using Ci-$MnFe_2O_4$. Moreover, for MH studies, these hybrid NPs not only observed almost similar heating rates as Ci-$MnFe_2O_4$ but

also its equilibrium temperature was higher than just Ci-$MnFe_2O_4$ over time. Moreover, since GNRs are promising contrast agents in optical imaging, these hybrid NPs also examined in photoacoustic imaging (PA) and indicated a strong contrast.

Keywords: 1. Magnetic Nanoparticles. 2. Gold Nanorods. 3. Magneto-motive Ultrasound Imaging. 4. Magnetic Hyperthermia. 5. Photoacoustic Imaging.

Table of Figures

Table of Content

Chapter 1: General Introduction

Cancer, a type of disease with uncontrollable and persistently growing cells that spread throughout the body, is considered one of the leading causes of death worldwide [1,2]. Recently, tremendous efforts have been devoted to developing novel techniques for early and accurate diagnosis and effective therapy. In this regard, nanotechnology has been proposed to allow working at the cellular and molecular levels and promote advances in healthcare [3–5] . Nanomaterials, due to their unique size and distinctive physiochemical properties, have received considerable attention in a wide range of applications, including engineering, biology, chemistry, material science, and, most notably, nanomedicine [6–9] . Magnetic nanoparticles (MNPs), for example, are attracting significant interest as one of the most common nanoscale groups and are applied in a variety of biomedical fields such as magnetic resonance imaging (MRI), biosensors, magneto-motive ultrasound imaging (MMUS), and magnetic hyperthermia (MH) [10–17] . Moreover, gold nanorods (GNRs), one of the most widely used noble metal NPs, have been paid much attention in recent years in imaging and therapy modalities owing to their fascinating optical properties [18–21] . The combination of these NPs is the promise for creation of hybrid nanoparticles with potential for non-ionizing theragnostic application based on ultrasound, magnetism and optical.

1.1. Magnetic Nanoparticles

Generally, iron oxides are formed when iron metal reacts with oxygen in the atmosphere. Thus, iron oxides have existed on earth for as long as there have been iron and oxygen. Iron oxide nanoparticles (IONPs) exhibit a wide range of crystal phases, including magnetite (Fe_3O_4), maghemite (γ-Fe_2O_3), Hematite (Fe_2O_3), and wüstite (FeO) [22] . Among all, Fe_3O_4 is one of the most studied NPs in cancer theranostic applications due to their excellent magnetic properties, low toxicity, easy preparation, and chemical stability [6,14]. Magnetite is composed of both Fe(II) and Fe(III), having an inverse spinel structure and Fe(II) ions occupying octahedral (Oh) sites, and tetrahedral (Td) and remaining Oh sites are split by Fe(III) ions. It has the general formula

AB_2O_4, where A and B indicate tetrahedral and octahedral sites, respectively and O shows the oxygen anion site [23]. Fe_3O_4 contains a face-centered cubic (FCC) unit cell [24], having an edge length of a = 0.8394 nm [25]. Figure 1.1 depicts the crystal structure of magnetite (Fe_3O_4).

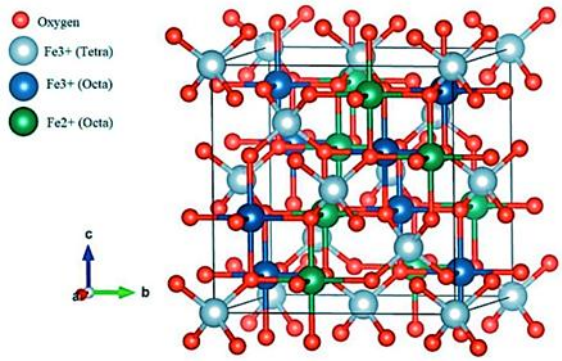

Figure 1.1. A spinel structure of magnetite (Fe_3O_4) that is face-centered cubic (FCC), and adapted from Fouad D et al. [26].

1.2. Nanomagnetism

Magnetic materials are categorized based on their response to an external magnetic field and characterized by their magnetic susceptibility (χ), which is determined by the ratio of magnetization (M) to the applied magnetic field (H). The three main types of magnetism are diamagnetism, paramagnetism, and ferromagnetism. Antiferromagnetism and ferrimagnetism are subdivision of ferromagnetism [27,28] . More specifically, in diamagnetic materials when the external field is applied, there are no magnetic dipoles, and they show a small negative magnetic susceptibility. The susceptibility of paramagnetic materials is small and positive, and their magnetic dipoles are randomly oriented in the absence of an applied magnetic field. The spins within the ferromagnetic materials align with the field in one specific direction and exhibit much larger susceptibility than other magnetic materials [29].

The susceptibility of the classified materials depends on the temperature and strength of the magnetic field (H). In other words, by increasing the values of H, the materials reach their saturation magnetization (*Ms*), Figure 1.2. When an external magnetic field is removed, magnetization remains in a ferromagnetic material known as remanent magnetization (*Mr*). An

additional H in the opposite direction, known as coercivity force (H_c), is required to achieve zero remanences [27,28]. The magnetization also lags the applied field, a phenomenon known as hysteresis. A typical hysteresis loop is illustrated in Figure 1.2 (a).

MNPs reveal physical behavior distinct from the bulk counterpart after applying an external magnetic field. Bulk materials have multi-domain structures, but when the core size of the particle is reduced, their structure change from multidomain to single domain and result in new magnetic properties. To put it another way, as the size of magnetic material diminishes, it gets harder to build domain walls, and below a specific size, which vary depending on the material, the energy required to create a domain wall becomes insufficient. Thus, the particles are turned into single-domain structures [30,31].

The relationship between particle size and coercivity is depicted in Figure 1.2 (b). As is shown in Figure 1.2 (b), when MNPs are either in single or multi-domain domains, H_c reaches its maximum level, and by reducing the size of the particles, the H_c begins to decrease. After particles reach a superparamagnetic size (SPR), the H_c completely disappears. Superparamagnetic NPs, after being exposed to an external field, their spins are aligned in the same direction as the applied field. In the absence of the magnetic field, these particles do not show any remanent magnetization and coercivity, which is of great interest in biomedical applications. However, hysteresis is commonly observed in ferromagnetic materials [31,32].

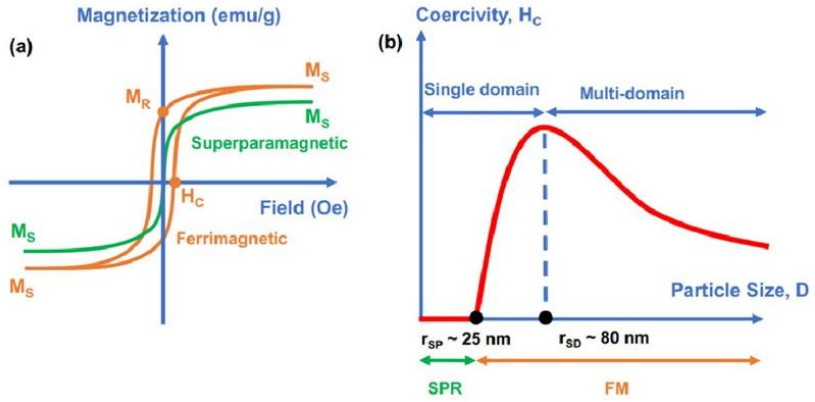

Figure 1.2. (a) Magnetization curves versus applied field for ferromagnetic (FM (red color)) and superparamagnetic (SPR (green color)), and (b) the change in coercivity of MNPs as a function of size, which is modified by Jun YW et al. [32].

Magnetic single-domain nanoparticles, after being subjected to an external magnetic field, all their magnetic dipoles are aligned parallel; these orientations minimize the anisotropy energy. For spherical particles, the magnetic anisotropy energy is defined below [33]:

$$E = KVsin^2\theta \qquad (1.1)$$

Where K is the effective anisotropy coefficient, V is the magnetic core volume and θ is the angle between the magnetization and the easy magnetization axis of the particle. Several factors, including the shape of the crystal, bulk magnetocrystalline anisotropy, dipolar interaction between neighboring and anisotropy constant nanoparticles, impact the anisotropy energy. When the size of particles decreases (below certain size), the anisotropy energy becomes lower than the thermal energy (k_BT: where k_B is the Boltzmann constant and T the absolute temperature) $KV < K_BT$. Thus, the particle conserves fixed alignments of the magnetic moment and becomes superparamagnetic. In comparison, the magnetic anisotropy energy of bulk materials is much higher than the thermal energy [29,33,34] . Figure 1.3 illustrates the energy diagram of MNPs having different magnetic spin alignments, ferromagnetism as a large particle and superparamagnetic as a small NP.

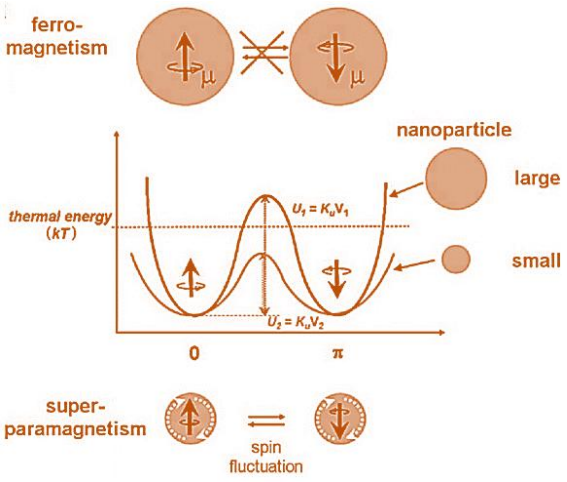

Figure 1.3. The variation of the anisotropy and thermal energies for particles with large and small sizes. Modified from Naween Dahal et al. [35].

1.3. Gold nanorods

Plasmonic nanostructures such as silver, gold, copper, and platinum are another type of NP that differ from their bulk counterparts due to their unique nanoscale properties. The optical properties of these NPs are directed by localized surface plasmons resonance (LSPR) [18,36,37]. Specifically, LSPR is created by irradiating metallic NPs with an appropriate wavelength of light, resulting in electron oscillations at a specific frequency along the metallic surface. Among different shapes of gold nanoparticles (e.g., cubic, rod, star), GNRs have been recognized as the most attractive plasmonic candidate for biomedical applications owing to their well-defined size, biocompatibility, and tunable optical properties [38,39]. To illustrate, for a given size, GNRs have two SPR bands; a transverse (short axis) shows a weak band like gold nanospheres at around 530 nm, while the intense longitudinal band exhibits a strong absorption peak of nearly from visible to near infrared (NIR (650−1200 nm, depending on the aspect ratio)). In the NIR region light absorption is minimal, resulting in maximum penetration in tissue, providing great opportunities for in vivo medical application [19–21,40–42]. These remarkable properties have expanded its use in different fields, such as biosensing, photothermal therapy, photoacoustic molecular imaging, and drug delivery. It should be noted that shape and size play a major role in LSPR and the optical characteristics of GNRs [38,43,44].

1.4. Synthesize of magnetic nanoparticles

MNPs have become an essential tool in biomedicine due to their nanoscale dimensions and promising properties, and these physiochemical characteristics are controlled through the synthesis routes [9,30]. Thus, several approaches have been explored to achieve biocompatible, monodisperse, highly stable, and well-shaped MNPs, which make them applicable in biomedical fields [14,17,45,46]. Some examples of chemical synthesis are coprecipitation (the most common route), thermal decomposition, hydrothermal and sol-gel [7,15,47,48]. A diagram illustration of different synthesis methods is shown in Figure 1.4. Here, we provide a brief description of a few popular synthesis techniques.

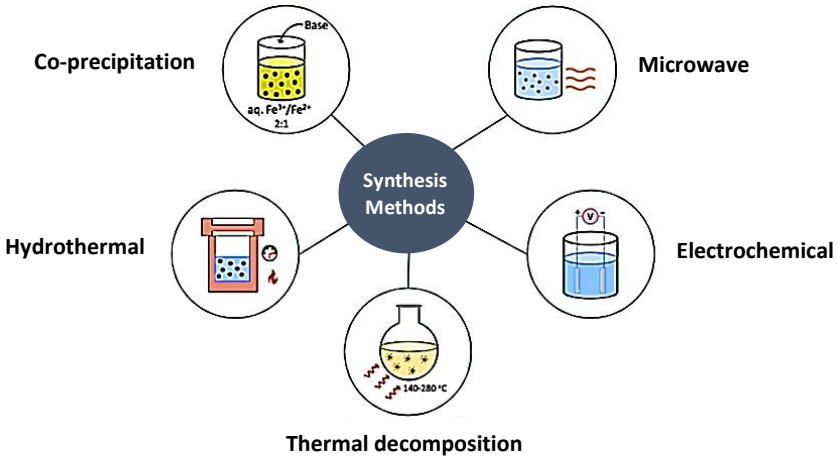

Figure 1.4. A schematic illustration of different methods to synthesize IONPs, taken from Mittal A et al. [49].

1.5. Coprecipitation method

Coprecipitation is known so far as one of the most convenient and high yield routes of synthesis, which can be performed at room temperature and under atmospheric conditions [13,46]. In this approach, the aqueous metal salts such as chlorides and sulfates are co-precipitated upon the addition of an appropriate base (NH_4OH or NaOH) at room temperature or high temperatures. Many parameters, such as PH, reaction temperature, salts ratio, basic solution dropping speed, and stirring rate, influence the size and shape of the final product [50–53].

It is essential to employ an appropriate ligand (organic or inorganic) during or after synthesis to enhance their stability and biocompatibility [9] . Polyethylene glycol (PEG), for example, is extensively deployed as a biocompatible stabilizing agent and FDA-approved polymer that allows further functionalization by targeting ligands, promoting a multifunctional application in both diagnoses and therapy [54,55]. Another advantage of using this polymer is the generation of strong steric repulsion, which can act as a barrier to particle interaction and increase the distance between particles after adsorbing this polymer onto the surface of MNPs. Furthermore, the presence of PEG on the surface of the IONPs reduces the rate of opsonization and subsequent mononuclear phagocyte system (MPS) clearance, resulting in a longer circulation time of MNPs, which is highly desirable in biomedical applications [56,57].

Although some studies have reported some disadvantages of coprecipitation, such as the presence of aggregation, difficulty in tuning the size, shape of the particles, and the broad size distribution of the products [58,59], optimizing some parameters during synthesis could enhance the quality of final MNPs to a great extent. On the other hand, this method has received much attention in several investigations owing to being the simplest, having a short reaction time, and a high reaction yield [50,51,60].

1.6. Thermal decomposition

Thermal decomposition (TD) is another standard method for producing monodisperse particles smaller than 20 nm with morphology control and narrow size distribution at high temperatures [61,62]. This procedure involves the decomposition of an organometallic precursor in a non-polar boiling solvent in the presence of stabilizing agents, such as 1-octadecene, and oleic acid (OA), at high temperatures. The primary organometallic precursors used in TD synthesis are metal carbonyls, such as iron oleate, $Fe((CO)_5)$, $Fe(Cup)_3$, and metal acetylacetonates [63,64] . This procedure begins with the decomposition of the iron oleate complex to form seeds at temperatures ranging from 200 to 240 °C, which then grow into NPs in the presence of an appropriate stabilizing agent at higher temperatures between 260 and 290 °C. Tuning reaction time, temperature, heating rate, and the molar ratios between the solvents and reducing agents significantly impact the particles' size and morphology [62,65].

Even though the NPs created by the TD method has excellent dispersibility in non-polar solvents, their hydrophobic property limits their application. As a result, further functionalization is required to switch their phases from hydrophobic to hydrophilic and make them useful in biomedical fields. Other disadvantages of this method are complicated procedure, high cost, extremely high temperature, and difficulty for producing a large particle yield [64,66].

1.7. Hydrothermal

The hydrothermal route is the third method for making NPs. Typically, the reaction mixture of metal salts, ethylene glycol, and PEG is stirred to form a clear solution, then sealed in a Teflon autoclave under a high vapor pressure of (0.3 to 4 MPa) and heated and kept at

temperatures between 130 to 250 °C over a long time (~ 8 h). The use of an appropriate solvent mixture and varying parameters such as temperature and reaction time all play an important role in formation of NP and size control [67]. However, the scale-up in this method is difficult and limited to producing NPs with a small size of less than 10 nm [48,66].

1.8. Synthesize of gold nanorods

There are different methods to synthesize GNRs, including the template, electrochemical, photochemical, and seeded growth methods [36,39,68]. The latter is regarded as one of the most typical approaches to preparing GNRs, due to is simplicity, flexible manufacturing of GNRs with different aspect ratios, low synthesis times, and fairly monodisperse [69,70]. This manufacture was first proposed in the 1920s [71] since then, several studies were performed using the same technique with only some modification to obtain the desired GNRs. The principal basis of this process is the formation of seed solution through the reduction of $HAuCl_4$ in the presence of a ligand like cetyltrimethylammonium bromide (CTAB) with cold sodium borohydride. The next step is a growth solution made up of tetrachloroauric acid ($HAuCl_4$) reduced by ascorbic acid, CTAB, and silver nitrate. Following that, a defined amount of gold seeds added to the growth solution serves as nucleation sites for the formation of NRs [69,70]. It should be noted that CTAB as a cationic surfactant micelle is proposed to govern growth of NPs and enhance the stability of the GNRs. In this synthesis, the number of parameters such as the concentration of CTAB, the reaction time, temperature, amounts of silver nitrate, and gold seed should be chosen properly. For example, the function of silver nitrate is to adjust the aspect ratio (size) which influences the longitudinal band of GNRs, while the transverse band remains unchanged. To elaborate, changing the aspect ratio by silver nitrate causes a red shift in the longitudinal band from visible to NIR regions, which is very beneficial for in vivo applications [18,37,40,44].

1.9. Biomedical applications of IONPs

MNPs due to their remarkable physicochemical properties have attracted significant interest in various biomedical applications. For example, superparamagnetic NPs have been widely used as promising contrast agents in diagnostic applications such as MRI, magnetic particle imaging (MPI), and MMUS [16,72–75]. In addition, their potential in therapeutic

platforms like MH and drug delivery has also been promoted in recent decades [76,77]. A schematic illustration of various biomedical applications of MNPs is depicted in Figure 1.5. This thesis will provide a brief explanation of MMUS and MH.

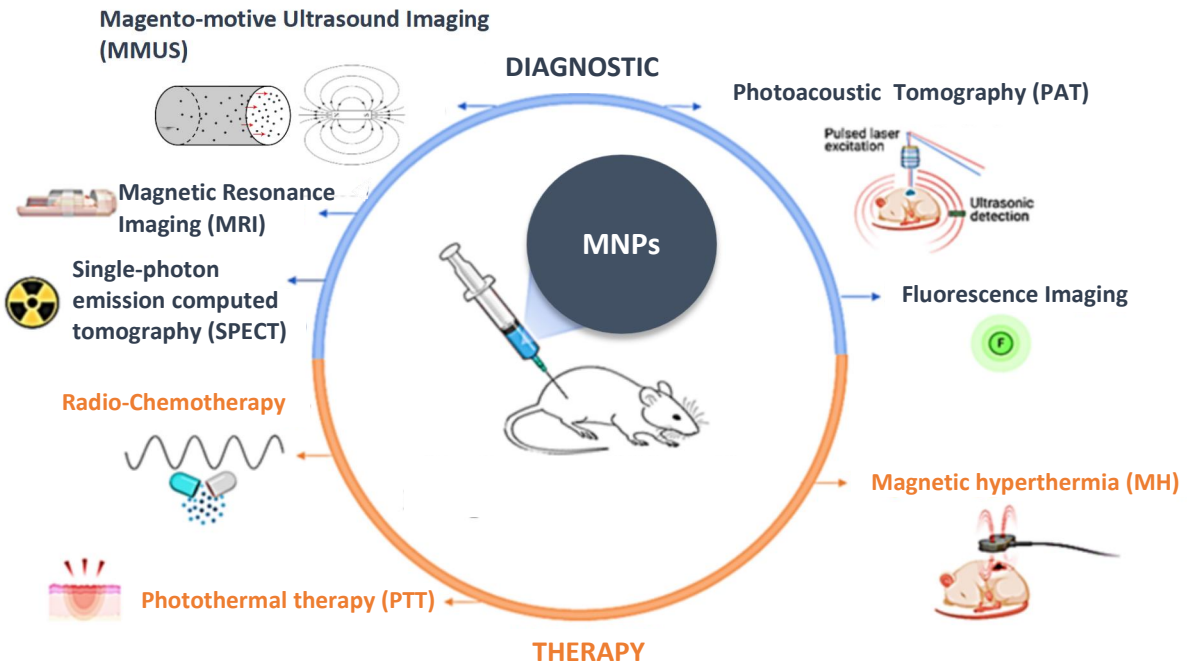

Figure 1.5. A schematic representation of MNPs-based diagnostic imaging techniques and therapeutic applications, taken from Lage T et al. [78].

1.9.1. Magneto-motive ultrasound imaging

MMUS imaging, a combination of magnetism and ultrasound, is proposed to overcome the poor contrast of stand-alone ultrasound imaging for the localization of MNPs [10]. This technique is one of the recent imaging modalities that benefits from superparamagnetic NPs as contrast agents to visualize molecular and cellular levels through ultrasound imaging while providing viscoelastic properties within the tissue filled with MNPs [79,80]. This approach applies an external time-varying magnetic field to move a magnetically labeled tissue. In other words, the interaction between an external magnetic field gradient with the MNPs leads to a magneto-motive force. The magneto-motive force acting on the movement of MNP in the direction of the magnetic field gradient is described by the Equation (1.2):

$$F_z = \frac{\lambda_{nps} V_{nps}}{\mu} B_0(z,t) \frac{\partial B_0(z,t)}{\partial z} \quad (1.2)$$

Where χ_{nps} is the MNP magnetic susceptibility, V_{nps} is the volume of MNPs, B_0 is the magnetic flux, and μ is the relative permeability of the medium. Therefore, the force acting on the MNPs is linearly proportional to the magnetic susceptibility, the volume of MNPs, and the magnetic field magnitude on the z-axis [10,75]. Optimizing any of these factors will enhance the induced displacements and, subsequently, the contrast of MMUS, which is the aim of this thesis. However, it should be noted that the displacement will only be linear if the magnetization remains in the linear region of the magnetization curve. Because after MNPs reach saturation magnetization, any increment of the magnetic field will not lead to a significant enhancement in the magnetization of the material.

1.9.2. Magnetic hyperthermia

Magnetic hyperthermia has gained much attention as one of the most efficient localized forms of therapy. When MNPs are excited by an altering current (AC) magnetic field, electromagnetic energy is converted into heat, and this heating ability can kill cancer cells. Because tumor cells have a higher metabolic rate than healthy cells, they are more susceptible to heating. Thus, when tumor cells are exposed to an alternating magnetic field, their temperature rise to 42-46 °C, significantly reducing cancer cell viability [12,76]. In MH, thermal energy upon excitation results from either relaxation mechanisms such as Neel/Brownian or hysteresis losses, which is associated with the shift of domain walls. Neel relaxation refers to the rotation of the magnetic moment of MNPs and is visualized in Figure 1.6. The Neel relaxation is expressed as [81]:

$$\tau_N = \tau_0 \exp\left(\frac{KV_m}{\kappa_b \mathrm{T}}\right) \quad (1.3)$$

Where τ_0 is the attempt time, equating to 10^{-9} s, K is the anisotropy constant; and its given values in the literature range from 7 to 20 KJ/m^3, V_m is the particle volume, κ_b is the Boltzmann constant, and T is the absolute temperature. Brownian relaxation, another mechanism responsible

for heat generation, is related to the physical rotation of particles (when the entire particle rotates) and can be described by [82]:

$$\tau_B = \frac{3\mu V_h}{\kappa_b \mathrm{T}} \qquad (1.4)$$

Where η and V_h are the viscosity of the medium and the hydrodynamic particle volume, respectively. Each of these mechanisms is highly dependent on the size and composition of MNPs. More specifically, for single-domain superparamagnetic NPs, Neel and Brownian relaxations are the leading causes of heating (until the size of MNPs is smaller than 20 nm), whereas the ferromagnetic materials are attributed to hysteresis losses. Thus, Brownian relaxation governs larger particle volumes and lower viscosities, whereas viscous solutions and small NPs are directed by Neel relaxation [83,84].

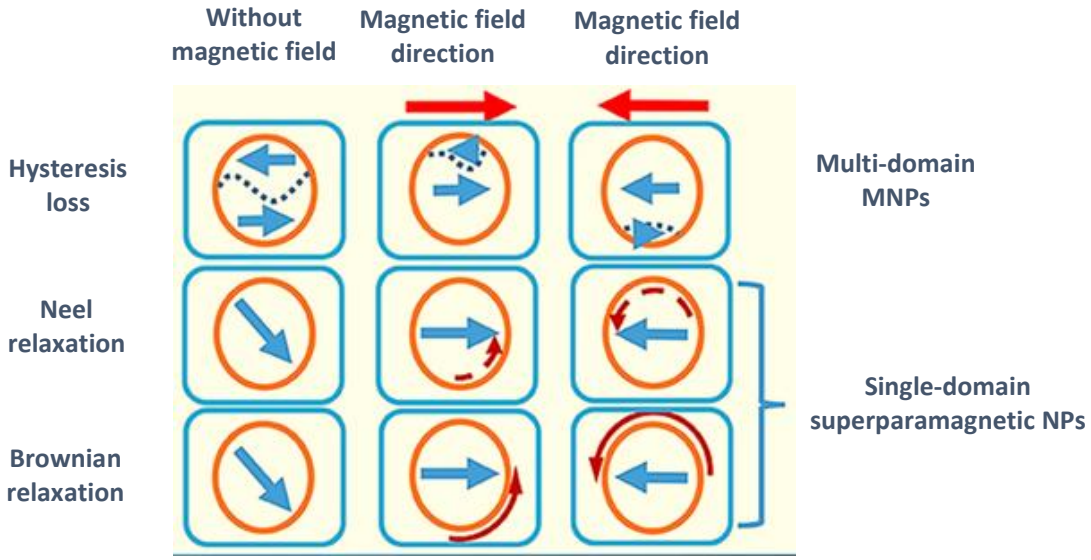

Figure 1.6: Brownian (the rotation of the entire particle) and Neel relaxation (the rotation of the magnetic moment within the particle) phenomena in superparamagnetic NPs, taken from Chang D et al. [85].

Depending on the particle core and hydrodynamic sizes, the Brownian and Neel relaxation performances occur at different time scales. Effective relaxation time can be given by [81]:

$$\tau_{eff} = \frac{\tau_B \tau_N}{\tau_B + \tau_N} \quad (1.5)$$

1.10. Biomedical application of gold nanorods

1.10.1. Photoacoustic imaging

Photoacoustic imaging (PAI) is a non-invasive hybrid imaging modality that contains an excellent temporal resolution of ultrasound imaging and contrast of optical imaging [86]. In this technique, a target is typically irradiated with a laser pulse (with a duration of ns) during PAI, which causes local temperature increases due to light absorption, the creation of a temperature gradient, and resulting in a subsequent thermoelastic expansion in the medium, generating acoustic waves, that are detected using a US acquisition. GNRs are highly desirable for use as PAI contrast agents due to their tunable resonance in the NIR spectrum and a very high absorption cross-section [87–89]. In addition, in PAI, GNRs generate higher optical absorption when compared to background tissue. Thus, highly localized, and targeted regions of interest can produce a higher PA emission signal. Optical imaging alone does not provide sufficient resolution in deep tissue due to optical scattering. However, PAI can reach much deeper into tissue and provide greater contrast, making it a potential system for diagnostic and therapeutic platforms such as cancer imaging (e.g., breast tumor detection), and its integration with other imaging modalities such as MMUS or photothermal therapy [90,91].

1.11. Motivation and scope of thesis

In this PhD thesis, we sought to develop multifunctional NPs, carry out all the required characterization, and examine their potential to be employed in biomedical applications. More specifically, our first purpose was to manufacture bare iron oxide NPs and coated by PEG with excellent physiochemical properties. In this regard, we used an optimized coprecipitation method to create bare MNPs with high stability, relatively high saturation magnetization, uniform size, and almost no aggregation for biomedical applications. Following that, PEG as a ligand was used to improve colloidal stability and biocompatibility, both of which are critical factors to consider before applying *in vivo.*

Our second aim was to prepare hybrid NPs with magnetic and optical properties. We suggested a mixture of Ci-$MnFe_2O_4$ and CTAB-GNRs with opposite surface charges because plasmonic and superparamagnetic NPs have received a lot of attention due to their attractive features in nanomedicine. Thus, the potential of this hybrid NPs in magneto-optical imaging and thermal therapy was verified. Next, we synthesized small and highly stable IONPs coated with sodium citrate and OA using coprecipitation and thermal decomposition methods, respectively, and estimated their properties. Furthermore, to improve the biocompatibility of CTAB-coated GNRs, further functionalization with silica shell was performed, as well as some characterizations.

1.12. Thesis outline

In this work, multifunctional NPs were synthesized and characterized, and they were found to be a promising candidate for biomedical applications. This thesis is divided into three major chapters, the second and third of which contain papers that have been published (paper 1, paper 2). Chapter 4 presents preliminary findings from PhD project that will be investigated further by members of our groups. The thesis is structured as follows:

Chapter 2 describes Uniform size PEGylated iron oxide nanoparticles as a potential theranostic agent synthesized by a simple optimized coprecipitation route. This work was published in the Journal of Magnetism and Magnetic Materials (JMMM).

Chapter 3 reports Hybrid Nanoparticles of Citrate Coated Manganese Ferrite and Gold Nanorods in Magneto-optical Imaging and Thermal Therapy. This work was published in the Journal of Nanomaterials.

Chapter 4 presents the initial investigation of OA and citrate coated IONPs via thermal decomposition and coprecipitation methods, respectively. Also, CTAB-GNRs was synthesized and overcoated by silica shell to enhance their biocompatibility and thermal stability for future investigation. Lastly, the cell viability of PEG-MNPs was assessed on the mammalian B16-F10 cell line.

References

1. Nagai H, Kim YH. Cancer prevention from the perspective of global cancer burden patterns. J Thorac Dis 2017 ; 9:448.

2. Sumer B, Gao J. Theranostic nanomedicine for cancer. Nanomedicine 2008;3:137–40.

3. Ahmed N, Fessi H, Elaissari A. Theranostic applications of nanoparticles in cancer. Drug Discov 2012;17:928–34.

4. Lima-Tenório MK, Gómez Pineda EA, Ahmad NM, Fessi H, Elaissari A. Magnetic nanoparticles: In vivo cancer diagnosis and therapy. Int J Pharm 2015;493:313–27.

5. Magnetic nanoparticles for precision oncology: theranostic magnetic iron oxide nanoparticles for image-guided and targeted cancer therapy. Nanomedicine 2017 Jan; 12(1): 73–87.

6. Banerjee R, Katsenovich Y, Lagos L, McIintosh M, Zhang X, Li CZ. Nanomedicine: Magnetic Nanoparticles and their Biomedical Applications. Curr Med Chem 2010; 17:3120–41.

7. Jinhao GAO, Hongwei GU, Bing XU. Multifunctional magnetic nanoparticles: design, synthesis, and biomedical applications. Acc Chem Res 2009;42:1097–107.

8. Dadfar SM, Roemhild K, Drude NI, von Stillfried S, Knüchel R, Kiessling F, et al. Iron oxide nanoparticles: Diagnostic, therapeutic and theranostic applications. Adv Drug Deliv Rev 2019;138:302–25.

9. Bohara RA, Thorat ND, Pawar SH. Role of functionalization: strategies to explore potential nano-bio applications of magnetic nanoparticles. RSC Adv 2016; 6:43989–4012.

10. Oh J, Feldman MD, Kim J, Condit C, Emelianov S, Milner TE. Detection of magnetic nanoparticles in tissue using magneto-motive ultrasound. Nanotechnology 2006; 17:4183.

11. Hadadian Y, Uliana JH, Carneiro AAO, Pavan TZ. A Novel Theranostic Platform: Integration of Magnetomotive and Thermal Ultrasound Imaging with Magnetic Hyperthermia. IEEE Trans Biomed Eng 2021; 68:68–77.

12. Perecin CJ, Tirich BM, Nagamine LCCM, Porto G, Rocha F v., Cerize NNP, et al. Aqueous synthesis of magnetite nanoparticles for magnetic hyperthermia: Formation mechanism approach, high water-dispersity and stability. Colloids Surf A Physicochem Eng Asp 2021;627:127169.

13. Arsalani S, Guidelli EJ, Araujo JFDF, Bruno AC, Baffa O. Green Synthesis and Surface Modification of Iron Oxide Nanoparticles with Enhanced Magnetization Using Natural Rubber Latex. ACS Sustain Chem Eng 2018; 6:13756–65.

14. Arruebo M, Fernández-Pacheco R, Ibarra MR, Santamaría J. Magnetic nanoparticles for drug delivery. NanoToday 2007; 2:22–32.

15. Tran N, Webster TJ. Magnetic nanoparticles: biomedical applications and challenges. J Mater Chem 2010 ; 20:8760–7.

16. Shen Z, Wu A, Chen X. Iron Oxide Nanoparticle Based Contrast Agents for Magnetic Resonance Imaging. Mol Pharm 2017 ; 14:1352–64.

17. Berry CC. Progress in functionalization of magnetic nanoparticles for applications in biomedicine. J Phys D Appl Phys 2009; 42:224003.

18. Chang SS, Shih CW, Chen CD, Lai WC, Wang CRC. The Shape Transition of Gold Nanorods. Langmuir 1998 ; 15:701–9.

19. Chen YS, Zhao Y, Yoon SJ, Gambhir SS, Emelianov S. Miniature gold nanorods for photoacoustic molecular imaging in the second near-infrared optical window. Nature Nanotechnology 2019; 14:465–72.

20. Kuo WS, Chang CN, Chang YT, Yang MH, Chien YH, Chen SJ, et al. Gold Nanorods in Photodynamic Therapy, as Hyperthermia Agents, and in Near-Infrared Optical Imaging. Angewandte Chemie 2010 ;122:2771–5.

21. Wang L, Li YF, Zhou L, Liu Y, Meng L, Zhang K, et al. Characterization of gold nanorods in vivo by integrated analytical techniques: Their uptake, retention, and chemical forms. Anal Bioanal Chem 2010 ;396:1105–14.

22. Ajinkya N, Yu X, Kaithal P, Luo H, Somani P, Ramakrishna S. Magnetic Iron Oxide Nanoparticle (IONP) Synthesis to Applications: Present and Future. Materials 2020, 13, 4644.

23. Brundle CR, Chuang TJ, Wandelt K. Core and valence level photoemission studies of iron oxide surfaces and the oxidation of iron. Surf Sci 1977; 68:459–68.

24. Yamamuro S, Farrell DF, Majetich SA. Direct imaging of self-assembled magnetic nanoparticle arrays: Phase stability and magnetic effects on morphology. Phys Rev B 2002; 65:224431.

25. Meldrum FC, Mann S, Heywood BR, Frankel RB, Bazylinski DA. Electron microscopy study of magnetosomes in a cultured coccoid magnetotactic bacterium. Proc R Soc Lond B Biol Sci 1993; 251:231–6.

26. Fouad D, Bachra Y, Ayoub G, Ouaket A, Bennamara A, Knouzi N, et al. A Novel Drug Delivery System Based on Nanoparticles of Magnetite Fe_3O_4 Embedded in an Auto Cross-Linked Chitosan. Chitin and Chitosan - Physicochemical Properties and Industrial Applications 2020.

27. Papaefthymiou GC. Nanoparticle magnetism. Nano Today 2009;4:438–47.

28. Morrish, H. A. The Physical Principles of Magnetism. ppm 2001; 696.

29. Stöhr J, Siegmann HC. Magnetism: From fundamentals to nanoscale dynamics. Magnetism: From Fundamentals to Nanoscale Dynamics 2006;152:1–822.

30. Chatterjee J, Haik Y, Chen CJ. Size dependent magnetic properties of iron oxide nanoparticles. J Magn Magn Mater 2003;257:113–8.

31. Majetich SA, Wen T, Mefford OT. Magnetic nanoparticles. MRS Bull 2013; 38:899–903.

32. Jun YW, Seo JW, Cheon J. Nanoscaling laws of magnetic nanoparticles and their applicabilities in biomedical sciences. Acc Chem Res 2008; 41:179–89.

33. Goya GF, Berquó TS, Fonseca FC, Morales MP. Static and dynamic magnetic properties of spherical magnetite nanoparticles. J Appl Phys 2003; 94:3520.

34. Luis F, Torres JM, García LM, Bartolomé J, Stankiewicz J, Petroff F, et al. Enhancement of the magnetic anisotropy of nanometer-sized Co clusters: Influence of the surface and of interparticle interactions. Phys Rev B 2002; 65:094409.

35. Naween Dahal. Synthesis and characterizations of novel magnetic and plasonic nanoparticles. Chemistry, Materials Science 2010.

36. Pérez-Juste J, Pastoriza-Santos I, Liz-Marzán LM, Mulvaney P. Gold nanorods: Synthesis, characterization and applications. Coord Chem Rev 2005; 249:1870–901.

37. Chen H, Shao L, Li Q, Wang J. Gold nanorods and their plasmonic properties. Chem Soc Rev 2013 ; 42:2679–724.

38. Meng L, Zhang J, Li H, Zhao W, Zhao T. Preparation and Progress in Application of Gold Nanorods. J Nanomater 2019.

39. Yang DP, Cui DX. Advances and Prospects of Gold Nanorods. Chem Asian J 2008; 3:2010–22.

40. Niidome T, Yamagata M, Okamoto Y, Akiyama Y, Takahashi H, Kawano T, et al. PEG-modified gold nanorods with a stealth character for in vivo applications. Journal of Controlled Release 2006;114:343–7.

41. Wang H, Huff TB, Zweifel DA, He W, Low PS, Wei A, et al. In vitro and in vivo two-photon luminescence imaging of single gold nanorods. Proc Natl Acad Sci U S A 2005; 102:15752–6.

42. Choi W il, Kim JY, Kang C, Byeon CC, Kim YH, Tae G. Tumor regression in vivo by photothermal therapy based on gold-nanorod-loaded, functional nanocarriers. ACS Nano 2011; 5:1995–2003.

43. Das M, Shim KH, An SSA, Yi DK. Review on gold nanoparticles and their applications. Toxicology and Environmental Health Sciences 2011 3:4; 3:193–205.

44. Morasso C, Picciolini S, Schiumarini D, Mehn D, Ojea-Jiménez I, Zanchetta G, et al. Control of size and aspect ratio in hydroquinone-based synthesis of gold nanorods. Journal of Nanoparticle Research 2015; 17:1–7.

45. Schladt TD, Schneider K, Schild H, Tremel W. Synthesis and bio-functionalization of magnetic nanoparticles for medical diagnosis and treatment. Dalton Transactions 2011; 40:6315–43.

46. Arsalani S, Hadadian Y, Mazon EE, Guidelli EJ, Kava E, Ramos AP, et al. Uniform size PEGylated iron oxide nanoparticles as a potential theranostic agent synthesized by a simple optimized coprecipitation route. J Magn Magn Mater 2022; 564:170091.

47. Noqta OA, Aziz AA, Usman IA, Bououdina M. Recent Advances in Iron Oxide Nanoparticles (IONPs): Synthesis and Surface Modification for Biomedical Applications. J Supercond Nov Magn 2019; 32:779–95.

48. Teja AS, Koh PY. Synthesis, properties, and applications of magnetic iron oxide nanoparticles. Progress in Crystal Growth and Characterization of Materials 2009; 55:22–45.

49. Mittal A, Roy I, Gandhi S. Magnetic Nanoparticles: An Overview for Biomedical Applications. Magnetochemistry 2022, 8, 107.

50. Mello LB, Varanda LC, Sigoli FA, Mazali IO. Co-precipitation synthesis of (Zn-Mn)-co-doped magnetite nanoparticles and their application in magnetic hyperthermia. J Alloys Compd 2019; 779:698–705.

51. Besenhard MO, LaGrow AP, Hodzic A, Kriechbaum M, Panariello L, Bais G, et al. Co-precipitation synthesis of stable iron oxide nanoparticles with NaOH: New insights and continuous production via flow chemistry. Chemical Engineering Journal 2020;399:125740.

52. Valenzuela R, Fuentes MC, Parra C, Baeza J, Duran N, Sharma SK, et al. Influence of stirring velocity on the synthesis of magnetite nanoparticles (Fe3O4) by the co-precipitation method. J Alloys Compd 2009;488:227–31.

53. Mascolo MC, Pei Y, Ring TA. Room Temperature Co-Precipitation Synthesis of Magnetite Nanoparticles in a Large pH Window with Different Bases. Materials 2013, 6, 5549-5567.

54. Alconcel SNS, Baas AS, Maynard HD. FDA-approved poly(ethylene glycol)– protein conjugate drugs. Polym Chem; 2:1442–8.

55. Horcajada P, Gref R, Baati T, Allan PK, Maurin G, Couvreur P, et al. Metal-organic frameworks in biomedicine. Chem Rev 2012; 112:1232–68.

56. Torchilin VP, Trubetskoy VS. Which polymers can make nanoparticulate drug carriers long-circulating? Adv Drug Deliv Rev 1995;16:141–55.

57. Fang C, Zhang M. Multifunctional magnetic nanoparticles for medical imaging applications. J Mater Chem 2009; 19:6258–66.

58. Ling W, Wang M, Xiong C, Xie D, Chen Q, Chu X, et al. Synthesis, surface modification, and applications of magnetic iron oxide nanoparticles. J Mater Res 2019; 34:1828–44.

59. Wang B, Wei Q, Qu S. Synthesis and Characterization of Uniform and Crystalline Magnetite Nanoparticles via Oxidation-precipitation and Modified co-precipitation Methods. Int. J. Electrochem. Sci 2013; 8:3786–93.

60. Mascolo MC, Pei Y, Ring TA. Room Temperature Co-Precipitation Synthesis of Magnetite Nanoparticles in a Large pH Window with Different Bases. Materials 2013, 6, 5549-5567.

61. Sun S, Zeng H, Robinson DB, Raoux S, Rice PM, Wang SX, et al. Monodisperse MFe2O4 (M = Fe, Co, Mn) Nanoparticles. J Am Chem Soc 2004; 126:273–9.

62. Chen Z. Size and Shape Controllable Synthesis of Monodisperse Iron Oxide Nanoparticles by Thermal Decomposition of Iron Oleate Complex. 2012; 42:1040–6.

63. Xu C, Sun S. Monodisperse magnetic nanoparticles for biomedical applications. Polym Int 2007 ; 56:821–6.

64. Lu AH, Salabas EL, Schüth F. Magnetic Nanoparticles: Synthesis, Protection, Functionalization, and Application. Angewandte Chemie International Edition 2007; 46:1222–44.

65. Park J, An K, Hwang Y, Park JEG, Noh HJ, Kim JY, et al. Ultra-large-scale syntheses of monodisperse nanocrystals. Nature Materials 2004 3; 3:891–5.

66. Wu W, He Q, Jiang C. Magnetic Iron Oxide Nanoparticles: Synthesis and Surface Functionalization Strategies. Nanoscale Research Letters 2008 3: 2008; 3:397–415.

67. Takami S, Sato T, Mousavand T, Ohara S, Umetsu M, Adschiri T. Hydrothermal synthesis of surface-modified iron oxide nanoparticles. Mater Lett 2007;61:4769–72.

68. Nikoobakht B, Wang ZL, El-Sayed MA. Self-Assembly of Gold Nanorods. Journal of Physical Chemistry B 2000; 104:8635–40.

69. Altansukh B, Yao JX, Wang D. Synthesis and characterization of gold nanorods by a seeding growth method. J Nanosci Nanotechnol 2009;9:1300–3.

70. Altansukh B, Yao JX, Wang D. Synthesis and Characterization of Gold Nanorods by a Seeding Growth Method. J Nanosci Nanotechnol 2009;9:1300–3.

71. Pérez-Juste J, Pastoriza-Santos I, Liz-Marzán LM, Mulvaney P. Gold nanorods: Synthesis, characterization and applications. Coord Chem Rev 2005;249:1870–901.

72. Shin TH, Choi Y, Kim S, Cheon J. Recent advances in magnetic nanoparticle-based multi-modal imaging. Chem Soc Rev 2015; 44:4501–16.

73. Yallapu MM, Othman SF, Curtis ET, Gupta BK, Jaggi M, Chauhan SC. Multi-functional magnetic nanoparticles for magnetic resonance imaging and cancer therapy. Biomaterials 2011;32:1890–905.

74. Mehrmohammadi M, Yoon KY, Qu M, Johnston KP, Emelianov SY. Enhanced pulsed magneto-motive ultrasound imaging using superparamagnetic nanoclusters. Nanotechnology 2010; 22:045502.

75. Mehrmohammadi M, Oh J, Ma L, Yantsen E, Larson T, Mallidi S, et al. Imaging of iron oxide nanoparticles using magneto-motive ultrasound. Proc IEEE Ultrason Symp 2007;652–5.

76. Kumar CSSR, Mohammad F. Magnetic nanomaterials for hyperthermia-based therapy and controlled drug delivery. Adv Drug Deliv Rev 2011;63:789–808.

77. Dobson J. Magnetic nanoparticles for drug delivery. Drug Dev Res 2006; 67:55–60.

78. Lage T, Rodrigues RO, Catarino S, Gallo J, Bañobre-López M, Minas G. Graphene-Based Magnetic Nanoparticles for Theranostics: An Overview for Their Potential in Clinical Application. Nanomaterials 2021,11, 1073.

79. Almeida TWJ, Sampaio DRT, Bruno AC, Pavan TZ, Carneiro AAO. Comparison between shear wave dispersion magneto motive ultrasound and transient elastography for measuring tissue-mimicking phantom viscoelasticity. IEEE Trans Ultrason Ferroelectr Freq Control 2015; 62: 2138–45.

80. Almeida TWJ, Sampaio DRT, Pavan TZ, Carneiro AAO. Shear wave Vibro Magneto Acoustography for measuring tissue mimicking phantom elasticity and viscosity. IEEE International Ultrasonics Symposium, IUS 2014;1097–100.

81. Liu X, Zhang Y, Wang Y, Zhu W, Li G, Ma X, et al. Comprehensive understanding of magnetic hyperthermia for improving antitumor therapeutic efficacy. Theranostics 2020 Jan 8; 10:3793.

82. Dieckhoff J, Eberbeck D, Schilling M, Ludwig F. Magnetic-field dependence of Brownian and Néel relaxation times. J Appl Phys 2016; 119:043903.

83. Hergt R, Dutz S, Röder M. Effects of size distribution on hysteresis losses of magnetic nanoparticles for hyperthermia. Journal of Physics: Condensed Matter 2008; 20:385214.

84. Deatsch AE, Evans BA. Heating efficiency in magnetic nanoparticle hyperthermia. J Magn Magn Mater 2014;354:163–72.

85. Chang D, Lim M, Goos JACM, Qiao R, Ng YY, Mansfeld FM, et al. Biologically targeted magnetic hyperthermia: Potential and limitations. Front Pharmacol 2018;9:831.

86. Liu Y, Nie L, Chen X. Photoacoustic Molecular Imaging: From Multiscale Biomedical Applications Towards Early-Stage Theranostics. Trends Biotechnol 2016;34:420–33.

87. Manohar S, Ungureanu C, van Leeuwen TG. Gold nanorods as molecular contrast agents in photoacoustic imaging: the promises and the caveats. Contrast Media Mol Imaging 2011; 6:389–400.

88. Knights OB, Ye S, Ingram N, Freear S, McLaughlan JR. Optimising gold nanorods for photoacoustic imaging in vitro. Nanoscale Adv 2019; 1:1472–81.

89. Chen YS, Frey W, Kim S, Kruizinga P, Homan K, Emelianov S. Silica-coated gold nanorods as photoacoustic signal nanoamplifiers. Nano Lett 2011;11:348–54.

90. Emelianov SY, Aglyamov SR, Karpiouk AB, Mallidi S, Park S, Sethuraman S, et al. Synergy and applications of combined ultrasound, elasticity, and photoacoustic imaging. Proc IEEE Ultrason Symp 2006; 1:405–15.

91. Mallidi S, Luke GP, Emelianov S. Photoacoustic imaging in cancer detection, diagnosis, and treatment guidance. Trends Biotechnol 2011; 29:213–21.

Chapter 2: Uniform size PEGylated iron oxide nanoparticles as a potential theranostic agent synthesized by a simple optimized coprecipitation route

Abstract

Iron oxide nanoparticles, due to their unique intrinsic magnetic properties, have attracted significant interest in biomedical applications. Therefore, the optimization of Magnetic Nanoparticles (MNPs) properties has always been the center of attention. For example, controlling the size of MNPs and enhancing their stability are the two most important parameters for biomedical applications that must be considered using an appropriate synthesis method. In this study, we synthesized bare magnetite NPs via an optimized coprecipitation route, followed by a post-synthesis procedure to coat them with polyethylene glycol (PEG). The synthesized MNPs presented optimized physiochemical properties, such as high stability, uniform size, relatively high saturation magnetization, and the absence of aggregation. The X-ray diffraction results revealed the high crystallinity of MNPs. Fourier transform infrared studies confirmed the surface modification of particles with PEG. Moreover, an in vitro biological assay on the bacterial strain of *Escherichia coli (E. coli)* Rosetta (DE3) demonstrated low cytotoxicity and no evident cytotoxicity for bare MNPs and PEG-MNPs, respectively at a high concentration (0.5 mg/mL). Lastly, the potential of these MNPs was investigated as theranostic agents in magnetomotive ultrasound imaging (MMUS) and magnetic hyperthermia (MH). Based on the obtained results, both MNPs demonstrated the same performance in MMUS; however, PEG-coated MNPs showed a higher heating efficiency. These results show the great potential of the particles to be used as theranostic agents or other biomedical applications owing to their high saturation magnetization.

2. Introduction

Over the last decades, nanotechnology has embraced multidisciplinary research such as industry, engineering, biotechnology, environmental science, and nanomedicine [1–3]. In nanomedicine, for instance, various nanomaterials have been proposed for theranostic application. As an example, iron oxide nanoparticles (IONPs) are considered one of the most promising nanostructures due to their unique physicochemical properties, such as superparamagnetic behavior, chemical stability, biocompatibility, etc. [4–6]. In biomedical applications, the surface modification of Magnetic Nanoparticles (MNPs) is an essential parameter since naked IONPs tend to aggregate rapidly, hence losing their colloidal stability. In addition, due to their high chemical activity, surface oxidation may occur, affecting their magnetic properties. Thus, appropriate, and biocompatible surfactants/ligands are required to obtain hydrophilic MNPs, which are stable against agglomeration under different conditions [7]. Various polymer molecules, surfactants, or inorganic materials such as polyvinylpyrrolidone (PVP), poly (vinyl alcohol) (PVA), polyethylene glycol (PEG), silica, citric acid, dextran, cetrimonium bromide (CTAB), etc. have been suggested to improve the colloidal and chemical stability of MNPs [8–10]. Among all, PEG is one of the most frequently used surface coating agents for IONPs owing to its very high biocompatibility, hydrophilicity, prolonging the circulation time of MNPs, and enhancing the colloidal stability [11–13]. Therefore, due to its excellent properties, MNPs coated by PEG have been used in diverse applications [14–16].

Several synthesis methods have been utilized to manufacture IONPs, including coprecipitation, thermal decomposition, hydrothermal, microemulsion, and sonochemical synthesis [17,18]. However, among all, coprecipitation is one of the most popular and highly efficient, being the simplest, the most cost-effective, nontoxic, and high-yield for largescale synthesis of IONPs [7,17,19]. However, compared to thermal decomposition as the gold standard method for producing monodisperse nanoparticles [18,20], coprecipitation has some disadvantages, such as the presence of aggregation, difficulty in tuning the size and shape of the particles, and the broad size distribution of the products. Nevertheless, due to its simplicity and efficiency, especially for the mass production of IONPs, a huge number of studies has been reported on optimizing the reaction parameters in this method to improve the quality of the resultant nanoparticles [7,21–25]. This includes the reaction temperature, the use of different iron

salts or bases, the molar ratios between the starting materials, the pH value, the dropping speed of base/salt solution, the ionic strength of the media, using different surfactants, and the stirring rate [21]. Although using a surfactant or size selection process has shown that coprecipitation can lead to obtaining narrow size distribution IONPs [26], most of the surfactant-free routes resulted in aggregated and/or broad size distribution nanoparticles. In addition, unless in a few cases where the entire reaction flow is controlled, reproducibility of the reaction is very difficult [27]. This can greatly affect both the size and magnetic properties of the resultant particles. Despite several promising progresses in exploring the effect of synthesis parameters, in most cases, addressing the issue of aggregation, non-uniformity, and/or very low saturation magnetization (typically between 30 and 50 emu/g [25]) in the resultant MNPs is still challenging. Sun et al. [28] by using the reaction temperature of 50 ◦C, adding the iron salts to ammonium hydroxide with a flow rate of 9 mL/ min, and stirring the reaction at 900 rpm, obtained MNPs with sizes ranging from 8 to 20 nm. The saturation magnetizations of their MNPs were between 41.60 and 49.24 emu/g. The IONPs synthesized by Mahdavi et al. [29] had sizes between 8 and 17 nm and saturation magnetizations ranging from 58 to 81 emu/g, where the optimal conditions were 45 ◦C as the reaction temperature, 800 rpm as the stirring rate, and a pH of 11. Kim et al. [30] added the iron source dropwise into an alkali source (NaOH) under vigorous mechanical stirring (2000 rpm) for 30 min at room temperature and passed nitrogen through the solution media to avoid undesirable oxidation of Fe^{2+}. According to their results, the synthesized MNPs demonstrated superparamagnetic behavior with a magnetization saturation of 42 emu/g and a diameter of 7.2 nm. Hans-Christian Roth et al. [31] synthesized IONPs of various mean sizes (3–17 nm) and saturation magnetizations from 16.7 to 89.19 Am^2kg. They investigated the influence of different parameters, such as alteration in reaction temperature, the concentration of iron salt, and the ratio of Fe^{3+}/Fe^{2+}, while maintaining a constant injection flow of 150 mL/min iron salt to NaOH solution. Results showed that the concentrations of iron salt and ratio of Fe^{3+}/Fe^{2+} had a linear relationship with particle size, however, the synthesis temperature had almost no effect on particle size. Li et al. [25] examined the addition of citric acid in different reaction stages, where the iron salts were added dropwise to NaOH at 80 °C with vigorous mechanical stirring for 15 min. They also studied the effect of temperature on the adsorption of citric acid on the surface of the MNPs in a two-step synthesis process. They found that the mean core sizes can vary from 6 to 13 nm depending on the stage of adding citric acid

and decrease in temperature resulted in increasing the hydrodynamic size from 52.9 to 132.9 nm on MNPs with the core size of 13 nm. The saturation magnetization of the IONPs in that study varied between 40 and 51 emu/g. In the present study, we aimed to obtain reproducible and biocompatible magnetite nanoparticles with a narrow size distribution, aggregate-free, and relatively high saturation magnetization, which can efficiently act as theranostic agents (i.e., in magnetomotive ultrasound imaging (MMUS) and magnetic hyperthermia (MH)). The molar ratios of starting materials for synthesizing bare IONPs were adapted from a previous study [7], but several other parameters were modified to obtain the optimized MNPs. To do so, several attempts were made to achieve the optimal synthesis condition for such particles. Mainly, four parameters, including the flow rate of adding the base solution to the iron salts (from 2 to 6 mL/min), the temperature of the reaction (from room temperature up to 90 °C), the stirring rate (from 200 to 1000 rpm), and the reaction time (2–10 min) were examined. Finally, we reached an optimal condition to synthesize bare MNPs: using 750 rpm, 6 mL/min, 80 °C, and 5 min as stirring rate, flow rate, reactions temperature, and time, respectively. Then, in a post-synthesis procedure, the obtained IONPs were successfully coated by PEG. Furthermore, both bare and coated IONPs were characterized using different techniques, including dynamic light scattering (DLS), zeta potential, transmission electron microscopy (TEM), magnetic separation (SEPMAG), vibrating sample magnetometer (VSM), and attenuated total reflection (ATR). In addition, biological studies were also conducted on these IONPs using the bacterial strain of *Escherichia coli (E. coli)* Rosetta (DE3).

2.1. Materials

The chemical reagents ferric chloride hexahydrate ($FeCl_3.6H_2O$) and ferrous chloride tetrahydrate ($FeCl_2.4H_2O$) were purchased from Sigma Aldrich. Ammonium hydroxide (NH_4OH; 27%), polyethylene Glycol (PEG-average mol. wt. 1500 Da), and hydrochloric acid (HCl; 37%) were purchased from Synth. All the materials were used as received without any purification.

2.2. Methods

2.2.1. Preparation of MNPs

Since the goal was to synthesize magnetite nanoparticles, the molar ratios were used based on stoichiometric magnetite structure (Fe_3O_4). The ratios of starting materials for

synthesizing bare IONPs were adapted from a previous study [7], where the resultant particles showed a relatively high saturation magnetization. However, to improve the particles' shape, size, and distribution while reducing the aggregation, several modifications were performed in the synthesis route compared to Arsalani et al. study [7]. In a typical reaction, first, 6.75 g of $FeCl_3.6H_2O$ was dissolved in 25 mL of pure water from a Milli-Q system, and 3.97 g of $FeCl_2.4H_2O$ was dissolved in 10 mL of an aqueous solution of hydrochloric acid (5.45 M). Then, a 1.28 M NH_4OH aqueous solution was prepared (2.5 mL NH_4OH in 47.5 mL pure water). The pH of the NH_4OH solution at room temperature was 11. Subsequently, this ammonia solution was heated up to 80 °C for 10 min on a hot plate, and its pH was decreased to 10.2. At the same time, using a heating mantle connected to a temperature controller (Novus, N1030) in a three-neck round-bottom flask, a mixture of 4 mL iron (III) chloride and 1 mL iron (II) chloride solution was also heated up to 80 °C. When both solutions reached 80 ˚C, the heat sources were turned off, and immediately the base solution was injected into the iron sources mixture dropwise using a syringe pump with the flow rate of 6 mL/min. The ammonia solution was added under mechanical stirring (750 rpm) using a mechanical homogenizer (Mod. 713, 713 D). After completing the injection of the base solution, the reaction media was stirred for additional 5 min. Upon starting the base injection to the iron sources, the color gradually changed from light brown to dark brown and finally to dark black after finishing the additional 5 min of stirring. The reaction medium was then transferred to a beaker and placed in an ultrasonic bath for 30 min. Finally, the IONPs were precipitated with a strong permanent magnet with a magnetic field strength of 300 mT. After discarding the supernatant, the IONPs were re-suspended in ultra-pure water. This washing process was carried out several times until the colloidal dispersion reached a pH of 6.5 (the pH of the water from Milli-Q system). After the last washing, the MNPs were dispersed in 40 mL, half of which were stored for characterization and the other half were used for functionalization with PEG. A schematic illustration of the synthesis setup is shown in Figure 2.1.

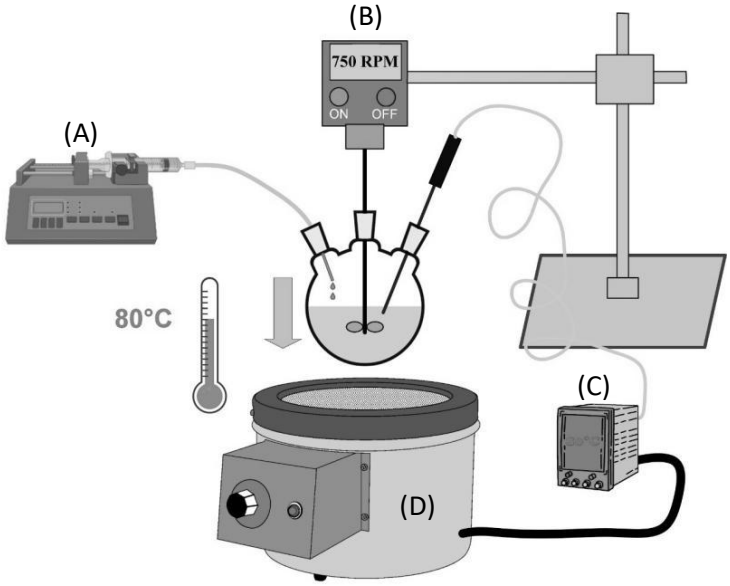

Figure 2.1. Schematic setup for preparing the MNPs. (A), (B), (C), and (D) are the syringe pump, the mechanical stirring system, the digital thermometer, and the heating mantle, respectively.

2.2.2. Functionalization with PEG

The bare IONPs were separated from the dispersion using a permanent magnet, and the water was decanted. Then, the surface modification of MNPs was conducted by adding a 6 wt% aqueous solution (10 mL and pH 6.8) of PEG to the particles. Following, the solution was mixed and sonicated for 8 min with an ultrasonic processor (Fisher Scientific, Pittsburgh, PA, USA). The ultrasonic processor was set with 20% amplitude and 5 s ON/15 s OFF cycle. To remove the unbounded PEG molecules from the dispersion, the final product was washed several times with ultra-pure water until it reached the pH of ultra-pure water. Finally, a portion of the sample was dried in an oven at 32 °C and under vacuum overnight for characterization. The rest of the sample was stored in refrigerator for further uses.

2.3. Characterization of MNPs and PEG-MNPs

Dynamic light scattering (DLS) was employed to measure the hydrodynamic diameters and zeta potential of MNPs by a fixed angle (173°) and an Nd: YAG laser (532 nm) using a Zetasizer Nano ZS (Malvern-UK). For this, the samples were dispersed in deionized water from a Milli-Q® system (resistivity 18.2 MΩ.cm. pH 6.5). The core size and morphology of bare and

coated MNPs were studied by transmission electron microscopy (TEM) using a JEOL-JEM-100 CXII unit with an accelerating voltage of 100 kV. For TEM samples, a droplet of the colloidal dispersion was placed onto a copper grid and dried at room temperature. The mean diameters were calculated from the TEM images using ImageJ software by measuring 900 particles per sample. The histograms of TEM images were then plotted using origin software. X-ray diffraction (XRD), D5005 Diffractometer, Bruker, analysis was conducted to study the crystal structure of the MNPs using X-ray beam nickel-filtered copper K radiation (λ = 1.5406 Å) in the range $10° < 2\theta° < 70°$. Furthermore, an attenuated total reflectance (ATR) accessory coupled to a Fourier-transform infrared spectrophotometer (FTIR) in a measurement range of 4000–400 cm−1 was used to verify the surface functionalization of MNPs. Moreover, a magnetic separation system (SEPMAG, Barcelona, Spain) having a magnetic field gradient of 15 T m^{-1} was used to examine the magnetophoretic behavior (motion of MNP in an inhomogeneous magnetic field) of samples. In addition, the magnetic properties of the particles were investigated by a vibrating sample magnetometer (VSM, EG&G Princeton Applied Research Magnetometer) at room temperature and on powder samples. Furthermore, thermal analyses (TGA) of the samples in powder form were conducted from room temperature to 600 ˚C under a N2 atmosphere and with a heating ramp of 10 °C/min using TGA Equipment (Model SDTQ600-TA Instruments). Lastly, the biocompatibility of the synthesized MNPs was examined using the bacterial strain of E. coli Rosetta as a preliminary test. More details about bacterial growth rate on used IONPs are described in the following section.

2.4. Cell culture and bacterial growth rate

E. coli bacterial strain Rosetta (DE3) was used to perform cytotoxicity assays. A single colony was inoculated in 10 mL of liquid Luria broth (LB) in the presence of 34 µg/mL of chloramphenicol, growing overnight at 37 ˚C and shaking at 200 rpm. The pre-inocula was diluted with the same LB medium containing the antibiotic to reach an optical density (OD) at 600 nm (OD600) of 0.01–0.02 using the NanoDrop 2000 spectrophotometer (Thermo Fisher Scientific, US). The bacterial solution was transferred to 250 mL Erlenmeyer flasks and mixed with the appropriate concentration of magnetic nanoparticles to reach the final concentrations of 0.05, 0.1, 0.25, and 0.5 mg/mL in a final volume of 25 mL, with the control solution containing only bacteria cells. The effect of MNPs concentrations on the bacterial growth rate was studied

by measuring the OD600 every 2 h of incubation time [32]. The absorbance measurements were corrected with the absorbance of the solution only containing the nanoparticles. The OD600 versus incubation time was normalized for each sample to calculate the exponential cell growth. The growth profile was fitted using the Origin 8.0 with the function $OD600 = C_1e^t /t_0 + C^2$, where C_1 is the constant amplitude, C_2 the offset, and t_0 the time constant. All the fits were with a 95% confidence interval [33].

2.5. Gelatin tissue-mimicking phantom preparation

Two cylindrical gelatin/agar tissue-mimicking phantoms were prepared to perform the MMUS experiment. Each phantom contained a hemispherical inclusion labeled with 0.35 wt% concentration of bare or PEG-coated MNPs. An aqueous solution of 6 wt% gelatin (GELITA, Sao Paulo, Brazil) and 3 wt% Agar (HiMedia, Mumbai, India) was prepared and heated to 90 ◦C for 2 h using a magnetic stirrer to obtain a homogeneous solution [34,35]. Then, the mixture was cooled down to 45 ˚C, and 0.4 mL formaldehyde (Synth, Sao Paulo, Brazil) was added. When the solution temperature reached 36 ˚C, the gelatin/agar mixture was poured over the inclusion, which was positioned in the bottom of the mold (20 × 75 mm). It should be mentioned that the inclusions were also prepared using the same gelatin/agar solution as used for the phantom. Finally, the phantom was kept in the refrigerator at 5 ˚C overnight.

2.6. MMUS setup

A pulsed MMUS device based on a discharge capacitor to generate an intense magnetic field pulse was used. This device is composed of three main stages [36]: Firstly, the charge circuit stage, which is consisted of a power supply line, converting the VAC to VDC; then, using this VDC, a capacitor charge circuit based on a half-bridge topology feeds an RC filter with a variable duty cycle, controlling the voltage value on a capacitor bank. Consequently, the second stage is to generate a magnetic field using the same capacitor bank, whose terminals are clamping to a coil (a solenoid with a ferromagnetic core) and a high-speed switching power device that activates the current pulse. The last stage is a control circuit based on a microcontroller, managing a USB bus for synchronizing the US acquisition system with the magnetic excitation [36]. The induced displacement of the phantom internal structure (in the

order of micrometer) was tracked by a multichannel ultrasound pulse/echo system (Sonix RP + Sonix DAQ, Ultrasonix) using a cross-correlation algorithm [37]. The maximum magnetic field applied 2 mm from the tip of the core was 740 mT with a frame rate of 4 kHz. A schematic of the MMUS setup is shown in Figure 2.2.

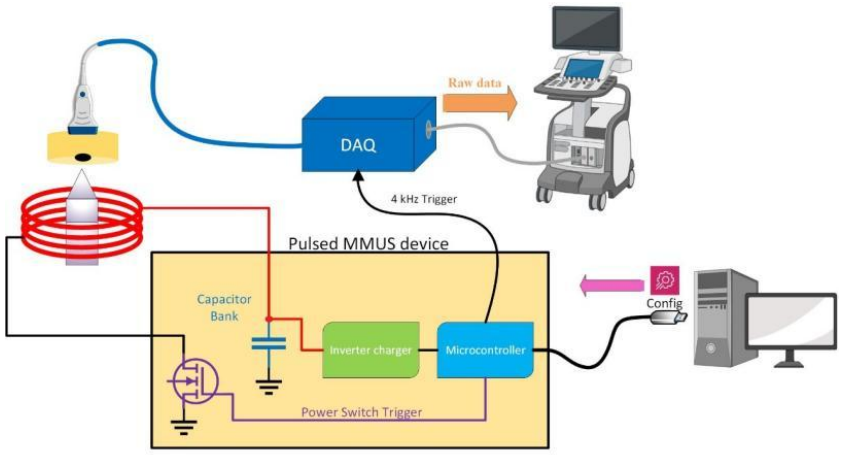

Figure 2.2. A schematic of the MMUS setup comprising an ultrasound imaging system, power device, and coil. The ultrasound transducer was symmetrically placed on the opposite side of the sample.

2.7. Hyperthermia experiments

For magnetic hyperthermia (MH) experiments, a device previously developed in our lab [38], was used. The sample was placed on a holder inside a solenoid with a diameter of 14 mm and a height of 87 mm, a configuration that ensures a homogenous magnetic field over the entire sample volume. The amplitude of the applied magnetic field was 10 mT at 132 kHz frequency. The concentration of both bare and coated MNPs dispersions was 0.35 wt%. The temperature of the samples was recorded by a fiber optic thermometer system (Qualitrol NOMAD-Touch Fiber Optic Monitor). Then, the heating efficiency of the samples was estimated using the specific loss power (SLP) equation for calorimetric method [39]. Moreover, the intrinsic loss power (ILP) was calculated to provide a better comparison with the SLP values reported in other studies [40].

2.8. Results and discussion

In this study, multiple syntheses were carried out to obtain reproducible narrow size IONPs with relatively high saturation magnetization to be used as theranostic agents. Among the

examined parameters, 6 mL/min, 80 °C, 750 rpm, and 5 min were chosen as the best conditions for a flow rate of adding a base, reaction temperature, stirring rate, and reaction time, respectively. These conditions resulted in well-defined size, high stability, and minimum aggregation in the final product. For example, stirring rates lower or higher than 750 rpm led to the production of polydisperse or significantly oxidized IONPs (brown color), respectively. At higher stirring velocities, a large number of bubbles due to the splashing of the reaction solution occurred. This, in turn, can increase the amount of oxygen in the reaction, as the reactions were conducted under an air atmosphere. For other parameters, using values other than the optimal ones, the reaction resulted in the presence of large aggregates, broad size distribution, or very low saturation magnetization samples. Since our goal in this study was to reach an optimized and reproducible route to synthesize narrow size IONPs with high saturation magnetization to be utilized as theranostic agents, rather than unrevealing the effects of synthesis parameters on the resultant particles, the data related to different synthesis conditions are not presented here. As a result, only the results related to the characterization and application of IONPs obtained under ideal conditions are reported. The hydrodynamic size of the samples was examined using DLS (Figure 2.3). Interestingly, the hydrodynamic size of PEG-coated MNPs and their polydispersity index (PDI) were reduced compared to bare MNPs. The size of particles and their PDI for bare and PEG-coated MNPs were 74 and 53 nm with PDI of 0.3 and 0.23, respectively.

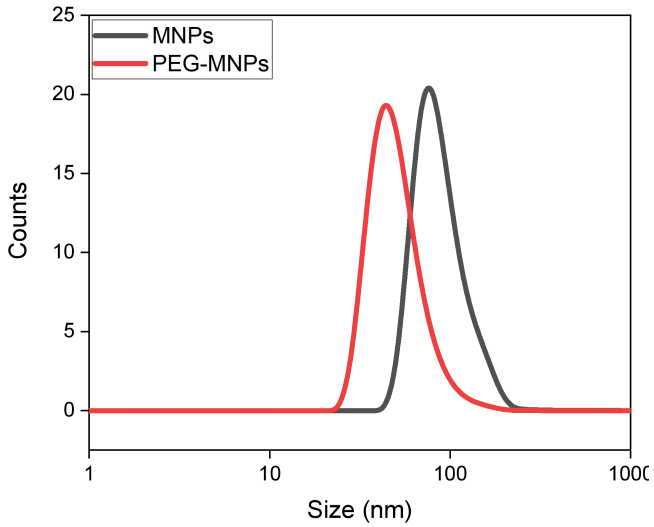

Figure 2.3. Hydrodynamic size for bare MNPs and PEG-coated MNPs.

The TEM images of bare and PEG-coated MNPs and their size distribution histograms are shown in Figure 2.4. The TEM results showed a homogeneous sphere-like shape in MNPs with a relatively narrow size distribution. More importantly, no clear aggregation, even for bare MNPs, was observed in the TEM images. Although the particles have appeared in TEM images in chain shapes or very close to each other, it is most probably due to the TEM sample preparation and physical contact and not aggregation. The TEM samples were prepared by a simple drop casting method, which results in clumps of NPs after drying [41]. Since the coating was performed in a post-synthesis step, it should not affect the core size but only the hydrodynamic size. As expected, both samples, considering the errors, have almost identical core sizes. The mean particle diameters are 23 ± 4.5 and 22 ± 4.7 nm for bare and coated MNPs, respectively. According to the obtained results, the diameter of NPs measured by DLS was larger than that of TEM. After coating the particles by PEG, one would expect to observe a larger hydrodynamic size in PEG-coated MNPs, however, here the opposite trend was observed. There could be two possible reasons for this observation. First, TEM images only provide information about the core size of NPs, whereas DLS measures the hydrodynamic size, which includes the core size and any molecules attached to the surface of the NPs. Larger hydrodynamic sizes are usually expected, compared to the core size [39,42,43]. Thus, one possible explanation is that the bare particles bear an electric double layer larger than the PEG-coated ones due to the counter ions and co-ions adsorption, resulting in a larger hydrodynamic size. The presence of PEG as a non-ionic surfactant [42–44] at the surfaces might hinder counter-ion adsorption and reduce the hydrodynamic size. Second, we speculate that in bare NPs, there was no or minimum aggregation, but probably to some extent agglomeration. The agglomerated particles can be easily separated using different approaches; they are held by weak van der Waals or magnetic forces rather than strong chemical bonds in the case of aggregated particles [45]. The presence of PEG as a non-ionic surfactant at the surfaces can hinder counter-ion adsorption and, as a result, preventing agglomeration and reducing the hydrodynamic size. Therefore, a slight agglomeration can cause DLS to identify the bare NPs as larger particles and report larger sizes.

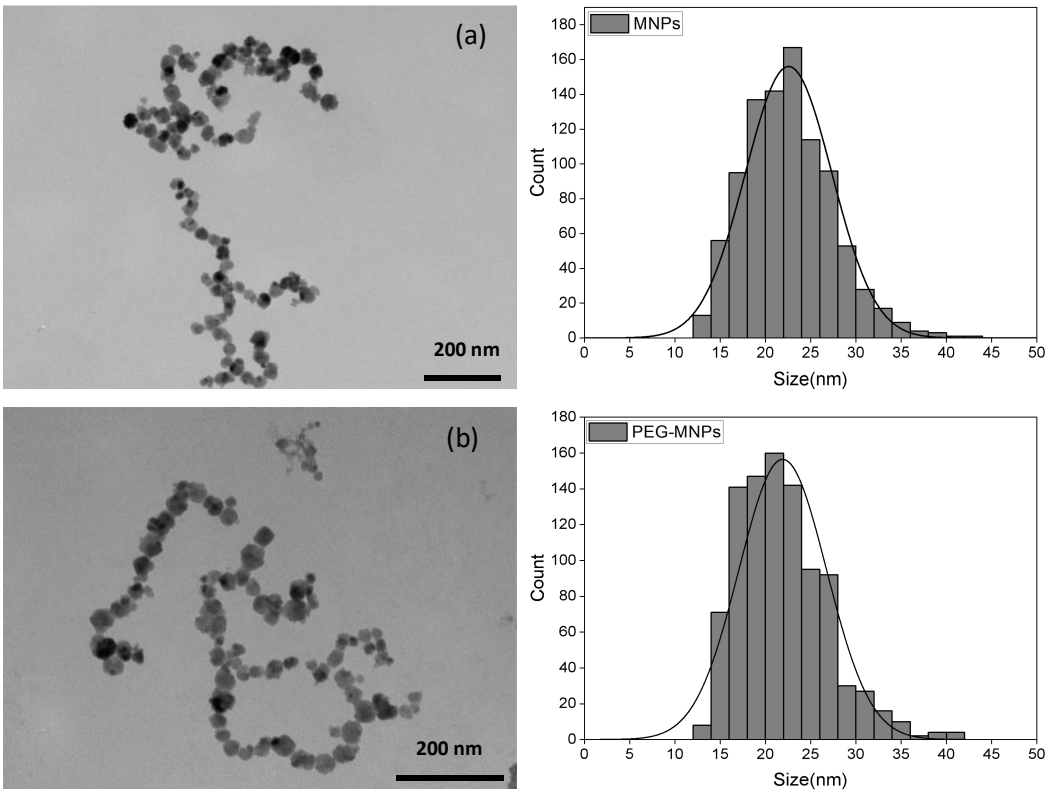

Figure 2.4. TEM images and histograms of the particle size distribution for bare MNPs (a) and PEG-MNPs (b). The scale bar corresponds to 200 nm.

XRD analyses were conducted to examine the crystal structure and size of the bare and PEG-coated MNPs (Figure 2.5). As it is expected, both samples revealed the same patterns. The diffraction peaks at 2θ (30.1, 35.5, 43.2, 53.6, 57.1, and 62.7◦) correspond to the (220) (311) (400) (422) (511) (440) Bragg angles very well-matched with the spinel structure of pure magnetite (Fe_3O_4), the JCPDS card no. 85-1436. Using the Scherrer equation [46], the average crystallite size of both samples was estimated considering the most intense peak (311) in the XRD patterns. The estimated crystallite sizes of bare and PEG-coated MNPs were 21.5 and 21 nm, respectively. The crystal sizes obtained here are in good agreement with the average size of TEM images, confirming that the particles are composed of single crystals [29]. In addition, coating the particles with PEG did not lead to any degradation of the magnetite cores.

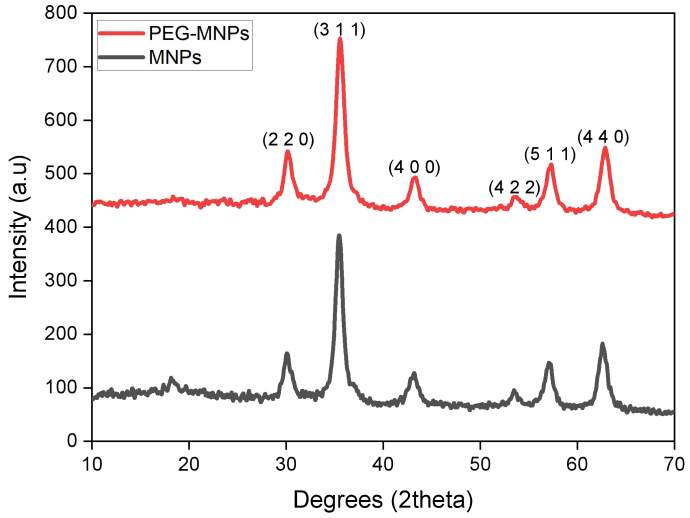

Figure 2.5. XRD patterns of bare MNPs and PEG-coated MNPs.

Evaluating the stability of MNPs is another important characterization before using them in any biomedical application. Therefore, Zeta potential analysis was employed to estimate the surface charge of both MNPs. Figure 2.6 shows the excellent Zeta potential values of 41 and 44 mV for bare and PEG-coated MNPs, respectively. According to the literatures [47,48], a Zeta potential value above ±30 mV indicates high stability in the MNPs dispersions. For bare MNPs prepared by coprecipitation and using NH_4OH, both negative [7] and positive [19,39] Zeta potentials have been reported. The positive surface charge can be due to the nitrogen binding of ammonium to metals on the surface of NPs. Due to this positive surface charge in bare MNPs and the fact that PEG is a neutral/ non-ionic polymer (~0 mV) [42–44], the absorption of PEG after coating has not affected the Zeta potential of the sample.

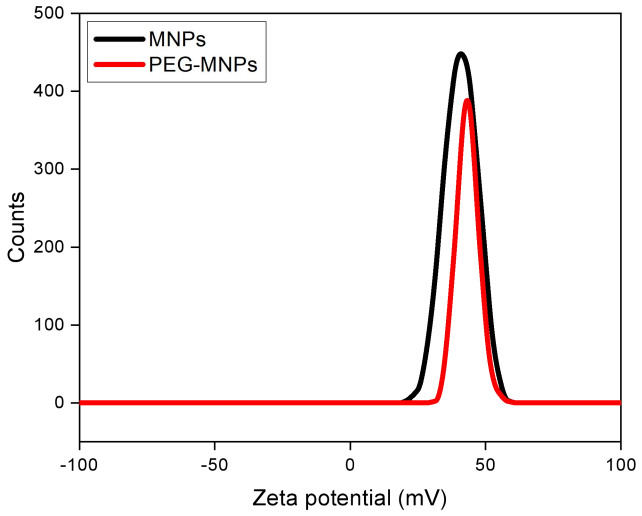

Figure 2.6. Zeta potential of bare MNPs and PEG-coated MNPs.

The FTIR spectra of bare and PEG-coated MNPs are presented in Figure 2.7. The dominant absorption band at 583 cm^{-1} is related to the stretching vibration mode of the Fe–O bond, indicating that the primary phase in both MNPs is Fe_3O_4 [49]. However, in nanosized magnetite nanoparticles, depending on the preparation method, there may be a degree of surface oxidation to maghemite. The appearance of small peaks around the 583 cm^{-1} band may be an indication of the presence of maghemite on the surface of the particles. Due to this reason, the possibility of surface oxidation, recalling the samples as iron oxide, seems to be more appropriate than magnetite. The spectra of bare and PEG coated MNPs have clear differences that can confirm the successful coating by PEG in MNPs. The wave numbers at 1390 and 1252 cm^{-1} in the FTIR spectrum of PEG-coated MNPs can be related to the stretching vibration of the C–O group and 2989 cm^{-1} corresponding to the C–H stretching band, confirming the presence of adsorbed PEG molecules on the surface of MNPs [50,51]. The band at the region of 3336 cm^{-1} is assigned to the stretching of the OH.

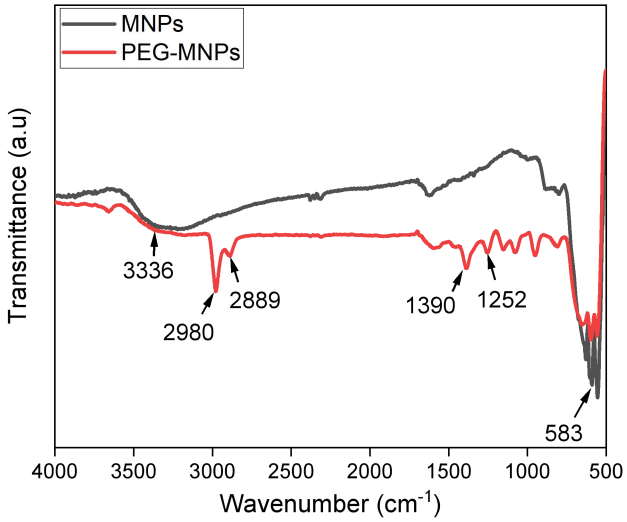

Figure 2.7. FTIR spectra of bare MNPs and PEG-coated MNPs.

Figure 2.8 provides information about the motion of MNP in a magnetic field gradient (magnetophoretic behavior). Since the system contains an optical sensor, it measures the changes in the opacity of the sample over time during the process. Generally speaking, at the beginning of the separation process (t = 0), the dispersion is a homogeneous distribution of MNPs (having the maximum opacity), but the opacity decreases as time passes. The time when the opacity is decreased by 50% (the half separation time) is referred as t_{50} and is usually used to study the magnetophoretical behavior of the sample. The magnetophoretic process of both MNPs at the concentration of 0.2 wt% in water was studied. According to the obtained results, MNPs coated by PEG showed a longer separation time of t_{50} = 95.25 s due to a smaller hydrodynamic size than the bare MNPs (Figure 2.8). In other words, since the hydrodynamic size of bare MNPs is larger, these MNPs experienced stronger attractive magnetic forces, and their movement along the magnetic field gradient is faster, resulting in a separation time of t_{50} = 66.7 s. Wittmann et al. [52] and Arsalani et al. [53] also reported similar results. In their studies, NPs with larger hydrodynamic size experienced stronger magnetic force and, consequently faster separation time compared to the smaller ones, which is in agreement with our results. In addition, the magnetic force is directly related to the magnetic moment of the particles. The bare MNPs, due to the absence of the surface coating molecules tend to agglomerate much faster in an applied field. The presence of these agglomeration in the system means the appearance of larger magnetic moments, which in turn increases the magnetic force.

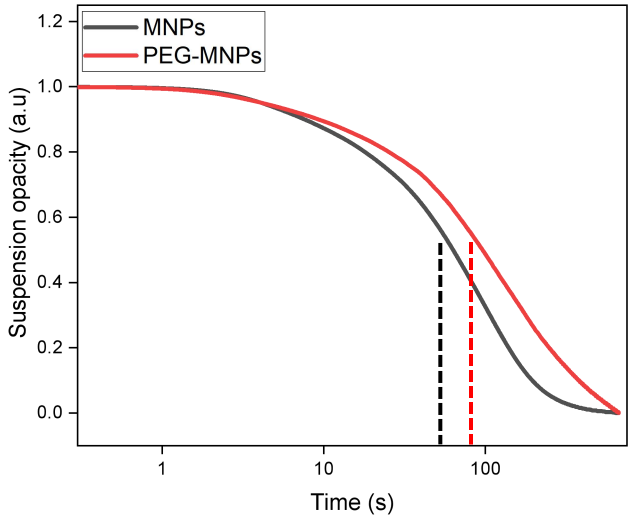

Figure 2.8. The magnetophoretic curve of bare MNPs and PEG-coated MNPs.

Figure 2.9a shows the room temperature M-H curves of the samples in the applied field of − 10 to +10 kOe, considering the mass of MNPs. The magnetization measurements showed superparamagnetic-like behavior in the samples with negligible coercivity. Due to the small remanence field in our VSM device (50–60 Oe), the observed coercivity field in the sample (around 100 Oe) cannot directly be assigned to the intrinsic properties of MNPs. The saturation magnetization of the as-synthesized bare MNPs was 66.7 emu/g, which was obtained by considering the mass of the powder sample used for VSM measurement. However, to calculate the saturation magnetization of the PEG-coated MNPs, the mass of inorganic matter (PEG) should be subtracted. Therefore, to determine the amount of PEG absorbed on the surface of the particles, TGA analyses were conducted on the powder sample (Figure 2.9b). The first derivative (DTGA) of the TGA data was plotted, and as can be seen, there are three sharp weight losses in the sample as the temperature has increased. The first weight loss, at temperatures up to 70 °C is due to the evaporation of the water observed on the surface of the particles from the environment. The second and third at around 280 and 450 are related to desorption and decomposition of PEG absorbed on the surface. of the MNPs [54]. In order to estimate the weight fraction of PEG and ensure not including any weight from the water, we considered the weight loss between 110 and 600 ˚C. At this range, the weight loss was 9%. Based on this result, the saturation magnetization of PEG-coated samples was calculated as 70.6 emu/g, which is slightly higher (~4 emu/g) than the as-synthesized bare MNPs. Interestingly, four months after synthesizing the samples, VSM

measurements were repeated, and the saturation magnetization of the bare MNPs was reduced to 60 emu/ g. The slight decrease (~6 emu/g) in the bare MNPs can be due to partial surface oxidation. These results show that PEGylating the MNPs not only prevents or at least defers the surface oxidation of the IONPs but also may enhance their saturation magnetization to some extent. It has been shown in several studies [7,18,55,56–59] that surface modification can significantly influence the magnetic properties of the materials at the nanoscale. The coordination of ligands to the surface of particles can reduce the surface spine disorder generated in nanomaterials because of the broken symmetry on the borders, thereby enhancing the saturation magnetization.

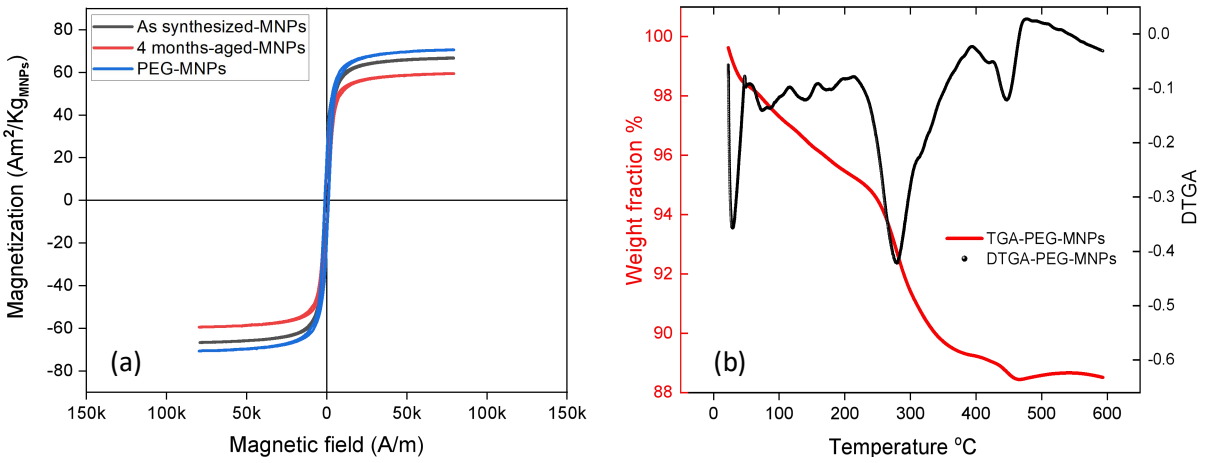

Figure 2.9. (a) Magnetization curves of as-synthesized MNPs repeated after four months of bare and PEG-coated MNPs measured considering the mass of MNPs, and (b) The TGA and DTGA of PEG-coated MNPs. Both VSM and TGA were conducted on powder samples.

The last characterization was performed to examine the biocompatibility of the synthesized MNPs using bacterial cells. This method can be used as a preliminary cytotoxicity evaluation, which has been widely used in other studies [32,60–64]. According to the results, the growth rate of the E. coli cells was not affected by low concentrations of MNPs (Figure 2.10). It is well-known that cell culture has different phases of growth: the lag phase, when the cells start to grow; the log phase, when the cell growth has an exponential behavior; the plateau, and the death phase [65]. Therefore, to avoid the influence of the MNPs' high absorption at 600 nm, the measurements started 2 h after the cell growth in the presence of MNPs and were performed until cells started the plateau phase. At this condition, the growth has a low rate and bacterial

populations do not increase. Interestingly, we observed a different growth profile for the cell culture with 0.5 mg/mL of bare MNPs and MNPs coated by PEG, indicating that the bare MNPs start to be toxic at this concentration (0.5 mg/ mL). Nevertheless, the PEG coating still has a role in keeping bacteria alive due to its biological compatibility, which is in agreement with the literature [66,67]. However, it should be taken into account that some parameters can affect the cytotoxicity of PEG-coated MNPs; for example, the method of synthesizing the MNPs and coating by PEG, the nature of the cell line, and using a high dosage of PEG [68,69]. Moreover, it should be mentioned that the cytotoxicity of a less complex cell, as a prokaryotic organism, may provide some preliminary information about the influence of the MNPs on the cell membrane since there is no compartmentalization of the cytosolic content inside these types of cells, and any interference on the membrane integrity would lead to a higher rate of cell death [70]. As the results suggest, the PEG-coated MNPs have no effect on cell growth, indicating that for the less complex organisms, we have promising and preliminary data that allows us to perform the cytotoxicity test using human cells, which is our next step. Meanwhile, some studies [71,72] have investigated reactive oxygen species (ROS) generation, which is one of the main causes of nanoparticle-induced cytotoxicity, to supplement the biocompatibility assay. According to these studies, as our bare and PEG-coated MNPs showed low cytotoxicity and no evident cytotoxicity behaviors, respectively, it is expected that the sample coated by PEG may either decrease the formation levels of the ROS or hinder the production of ROS. It is worth mentioning that the maximum concentration used for diagnostic (MMUS) or therapeutic (MH) applications in this work was around 0.35 wt%, and based on cytotoxicity results, the bare MNPs can still be considered safe at this concentration.

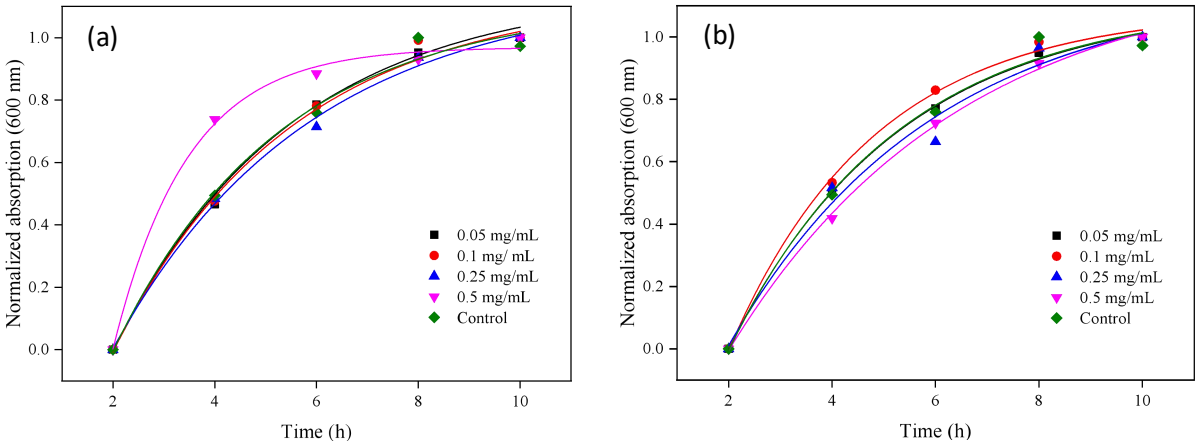

Figure 2.10. Effect of bare MNPs concentration on the *E. coli* cell growth rates (a) and PEG-coated MNPs (b). Optical density was normalized for each sample and fitted with an exponential growth function.

Figure 2.11 shows the displacement map of both samples obtained by MMUS imaging in phantoms embedded with bare, 11(a) and coated MNPs, 11(b). The red color regions present higher displacements indicating where the MNPs are located. The induced displacements for phantoms containing either of MNPs were the same (around 14 µm), using a magnetic pulse width of 6 ms. The magneto-motive force in MMUS imaging that causes the displacements is directly proportional to the susceptibility and magnetization of the particles at the applied magnetic field [19,34]. Therefore, based on the obtained results, the presence of PEG as a ligand preserved the intrinsic magnetic properties of the particles, such that they had the same response in the applied magnetic field of MMUS imaging. Therefore, both MNPs can be considered suitable candidates for MMUS.

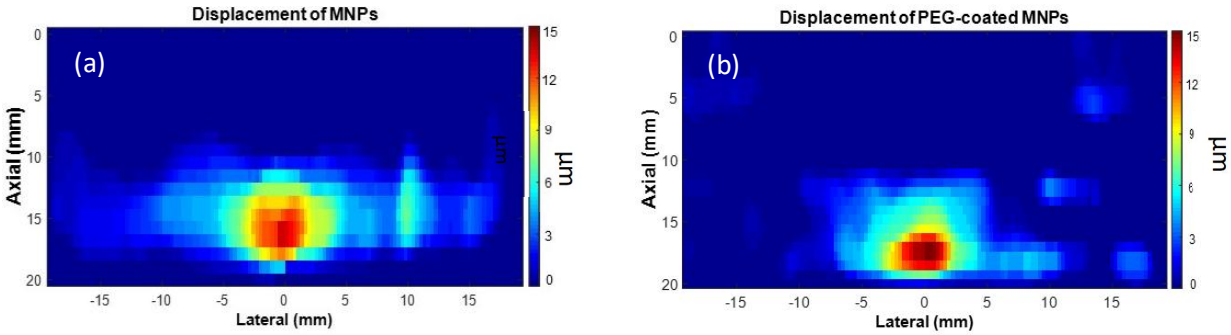

Figure 2.11. MMUS image of the phantom containing bare MNPs (a) and PEG-coated MNPs (b).

The temperature variation as a function of time for the bare, PEG coated MNPs (both with the concentration of 0.35 wt% dispersed in water), and water (as a control sample) are shown in Figure 2.12. SLP was calculated for both samples using the Box-Lucas method [39]. The SLP values were 17 W/g and 27.5 W/g for the bare and PEG-coated MNPs, respectively. These are corresponded to the ILP values of 2 and 3.2 $nHm^2\ kg^{-1}$ for bare and PEG-coated MNPs, respectively. Clearly, the PEG-coated MNPs showed a higher heating efficiency than bare MNPs. One possible explanation is that the presence of the PEG as a surfactant increases thermal conductivity in the system [41]. Another reason might be due to the changes that happened by the addition of PEG in the hydrodynamic diameter of the particles, which is directly affecting the Brownian relaxation time of MNPs [73]. Lastly, the stronger magnetic dipolar interaction in the bare MNPs compared to the coated ones can be detrimental for their heating efficiency [39]. Hence, PEG-coated MNPs can be considered a suitable candidate for MH too.

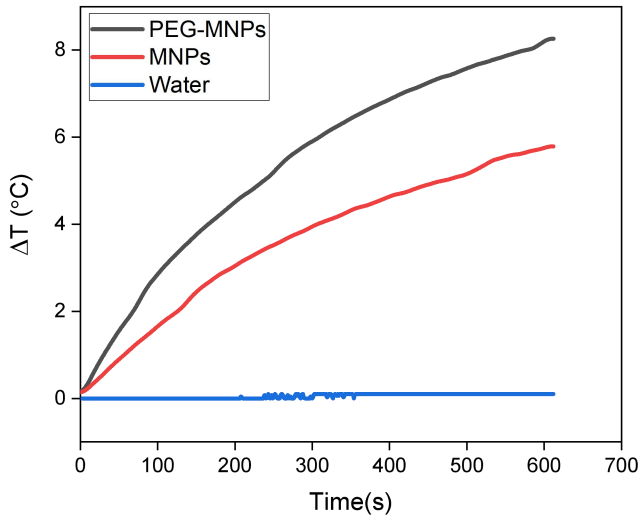

Figure 2.12. Temperature change as a time function for bare MNPs and PEG-coated MNPs.

2.9. Conclusion

To sum up, we optimized some parameters in the coprecipitation method to obtain a narrow size, relatively homogeneous shape with no or minimum aggregation (at least based on the TEM images), and relatively high saturation magnetization IONPs in a surfactant-free reaction. In addition, reproducibility in coprecipitation has long been a significant issue. Although very simple, the synthesis procedure in the present study led to a highly acceptable reproducibility in

the morphological and magnetic properties of the particles. The final remark is the high chemical stability of the particles achieved after coating by PEG, which resulted in preventing or at least deferring the surface oxidation of the IONPs during the time. In conclusion, both samples illustrated a high performance as contrast agents for MMUS, and PEG-coated MNPs showed a higher heating efficiency for MH. Hence, the synthesized MNPs have the potential to be considered as theranostic agents or used in other biomedical applications due to their optimized physiochemical properties.

Acknowledgments

The technical support given by Carlos Renato, Agnelo dos Santos Bastos Neto, Carlos A. Brunelo, Lourenco Rocha, and A. Maulin for the TEM images are greatly appreciated. Also, we are thankful to Prof Antonio Costa for sharing the biological samples and necessary equipment for Cytotoxicity measurements. Partial financial support was received from FAPESP Grants 2018/16939-8, 2016-0232-0, 2013/ 07699-0, CNPq-311224/2021-0, and CAPES - Finance Code 001.

References

[1] S.M. Dadfar, K. Roemhild, N.I. Drude, S. von Stillfried, R. Knüchel, F. Kiessling, T.J.A.d.d.r. Lammers, Iron oxide nanoparticles: Diagnostic, therapeutic and theranostic applications, Advanced drug delivery review, 138 (2019) 302-325.

[2] R. Banerjee, Y. Katsenovich, L. Lagos, M. McIintosh, X. Zhang, C.Z. Li, Nanomedicine: magnetic nanoparticles and their biomedical applications, Current medicinal chemistry, 17 (2010) 3120-3141.

[3] H. Arami, A. Khandhar, D. Liggitt, K.M.J.C.S.R. Krishnan, In vivo delivery, pharmacokinetics, biodistribution and toxicity of iron oxide nanoparticles, Chemical Society Reviews, 44 (2015) 8576-8607.

[4] V.I. Shubayev, T.R. Pisanic II, S.J.A.d.d.r. Jin, Magnetic nanoparticles for theragnostics, Advanced drug delivery reviews, 61 (2009) 467-477.

[5] T. Neuberger, B. Schöpf, H. Hofmann, M. Hofmann, B. Von Rechenberg, Superparamagnetic nanoparticles for biomedical applications: possibilities and limitations of a new drug delivery system, Journal of Magnetism and Magnetic Materials, 293 (2005) 483-496.

[6] M. Mozaffari, Y. Hadadian, A. Aftabi, M.O.J.J.o.M. Moakhar, M. Materials, The effect of cobalt substitution on magnetic hardening of magnetite, 354 (2014) 119-124.

[7] S. Arsalani, S. Arsalani, Y. Hadadian, D.R.T. Sampaio, O. Baffa, T.Z. Pavan, A.A.O. Carneiro, The effect of magnetization of natural rubber latex-coated magnetite nanoparticles on shear wave dispersion magneto-motive ultrasound, Physics in Medicine & Biology, 64 (2019) 215019.

[8] S. Arsalani, E.J. Guidelli, J.F.D.F. Araujo, A.C. Bruno, O. Baffa, Green Synthesis and Surface Modification of Iron Oxide Nanoparticles with Enhanced Magnetization Using Natural Rubber Latex, ACS Sustainable Chemistry & Engineering, 6 (2018) 13756-13765.

[9] J.V. Jokerst, T. Lobovkina, R.N. Zare, S.S. Gambhir, Nanoparticle PEGylation for imaging and therapy, Nanomedicine, 6 (2011) 715-728.

[10] K. Wu, D. Su, J. Liu, R. Saha, J.-P.J.N. Wang, Magnetic nanoparticles in nanomedicine: A review of recent advances, 30 (2019) 502003.

[11] A.J. Szalai, N. Manivannan, G.J.C. Kaptay, S.A. Physicochemical, E. Aspects, Super-paramagnetic magnetite nanoparticles obtained by different synthesis and separation methods stabilized by biocompatible coatings, Colloids and Surfaces A, 568 (2019) 113-122.

[12] C. Sun, K. Du, C. Fang, N. Bhattarai, O. Veiseh, F. Kievit, Z. Stephen, D. Lee, R.G. Ellenbogen, B.J.A.n. Ratner, PEG-mediated synthesis of highly dispersive multifunctional superparamagnetic nanoparticles: their physicochemical properties and function in vivo, ACS nano, 4 (2010) 2402-2410.

[13] B. Thapa, D. Diaz-Diestra, J. Beltran-Huarac, B.R. Weiner, G.J.N.r.l. Morell, Enhanced MRI T 2 relaxivity in contrast-probed anchor-free PEGylated iron oxide nanoparticles, 12 (2017) 1-13.

[14] J. Xie, C. Xu, N. Kohler, Y. Hou, S.J.A.M. Sun, Controlled PEGylation of monodisperse Fe3O4 nanoparticles for reduced non-specific uptake by macrophage cells, Advanced Materials, 19 (2007) 3163-3166.

[15] G. Antarnusa, E.J.M.R.E. Suharyadi, A synthesis of polyethylene glycol (PEG)-coated magnetite Fe3O4 nanoparticles and their characteristics for enhancement of biosensor, 7 (2020) 056103.

[16] C. Yue-Jian, T. Juan, X. Fei, Z. Jia-Bi, G. Ning, Z. Yi-Hua, D. Ye, G.J.D.d. Liang, i. pharmacy, Synthesis, self-assembly, and characterization of PEG-coated iron oxide nanoparticles as potential MRI contrast agent, 36 (2010) 1235-1244.

[17] R. Hao, R. Xing, Z. Xu, Y. Hou, S. Gao, S.J.A.m. Sun, Synthesis, functionalization, and biomedical applications of multifunctional magnetic nanoparticles, 22 (2010) 2729-2742.

[18] A. Ali, H. Zafar, M. Zia, I. ul Haq, A.R. Phull, J.S. Ali, A.J.N. Hussain, science, applications, Synthesis, characterization, applications, and challenges of iron oxide nanoparticles, Nanotechnology, 9 (2016) 49.

[19] Y. Hadadian, H. Masoomi, A. Dinari, C. Ryu, S. Hwang, S. Kim, B.k. Cho, J.Y. Lee, J.J.A.o. Yoon, From Low to High Saturation Magnetization in Magnetite Nanoparticles: The Crucial Role of the Molar Ratios Between the Chemicals, ACS omega, (2022).

[20] Y. Hadadian, A.P. Ramos, T.Z.J.S.R. Pavan, Role of zinc substitution in magnetic hyperthermia properties of magnetite nanoparticles: Interplay between intrinsic properties and dipolar interactions, Scientific Reports, 9 (2019) 1-14.

[21] S. Arsalani, J. Oliveira, E.J. Guidelli, J.F. Araujo, F. Wiekhorst, O.J.C. Baffa, S.A. Physicochemical, E. Aspects, Synthesis of radioluminescent iron oxide nanoparticles functionalized by anthracene for biomedical applications, Physicochemical and Engineering Aspects, 602 (2020) 125105.

[22] W. Wu, Q. He, C. Jiang, Magnetic iron oxide nanoparticles: synthesis and surface functionalization strategies, Nanoscale Res Lett, 3 (2008) 397-415.

[23] A. Joseph, S. Mathew, Ferrofluids: Synthetic Strategies, Stabilization, Physicochemical Features, Characterization, and Applications, ChemPlusChem, 79 (2014) 1382-1420.

[24] W. Wu, Z. Wu, T. Yu, C. Jiang, W.-S. Kim, Recent progress on magnetic iron oxide nanoparticles: synthesis, surface functional strategies and biomedical applications, Sci. Technol. Adv. Mater., 16 (2015) 023501.

[25] W. Wu, C.Z. Jiang, V.A.L. Roy, Designed synthesis and surface engineering strategies of magnetic iron oxide nanoparticles for biomedical applications, Nanoscale, 8 (2016) 19421-19474.

[26] L. Li, K.Y. Mak, C.W. Leung, K.Y. Chan, W.K. Chan, W. Zhong, P.W.T. Pong, Effect of synthesis conditions on the properties of citric-acid coated iron oxide nanoparticles, Microelectron. Eng., 110 (2013) 329-334.

[27] C.-Y. Hong, I.J. Jang, H.E. Horng, C.J. Hsu, Y.D. Yao, H.C. Yang, Ordered structures in Fe3O4 kerosene-based ferrofluids, J. Appl. Phys., 81 (1997) 4275-4277.

[28] A.P. LaGrow, M.O. Besenhard, A. Hodzic, A. Sergides, L.K. Bogart, A. Gavriilidis, N.T.K. Thanh, Unravelling the growth mechanism of the co-precipitation of iron oxide nanoparticles with the aid of synchrotron X-Ray diffraction in solution, Nanoscale, 11 (2019) 6620-6628.

[29] J. Sun, S. Zhou, P. Hou, Y. Yang, J. Weng, X. Li, M. Li, Synthesis and characterization of biocompatible Fe3O4 nanoparticles, Journal of Biomedical Materials Research Part A, 80A (2007) 333-341.

[30] M. Mahdavi, M. Ahmad, M. Haron, F. Namvar, B. Nadi, M. Rahman, J. Amin, Synthesis, Surface Modification and Characterisation of Biocompatible Magnetic Iron Oxide Nanoparticles for Biomedical Applications, Molecules, 18 (2013) 7533-7548.

[31] D. Kim, Y. Zhang, W. Voit, K. Rao, M.J.J.o.m. Muhammed, M. Materials, Synthesis and characterization of surfactant-coated superparamagnetic monodispersed iron oxide nanoparticles, magnetism and Magnetic Materials, 225 (2001) 30-36.

[32] H.-C. Roth, S.P. Schwaminger, M. Schindler, F.E. Wagner, S.J.J.o.M. Berensmeier, M. Materials, influencing factors in the CO-precipitation process of superparamagnetic iron oxide nano particles: a model based study, Magnetism and Magnetic Materials, 377 (2015) 81-89.

[33] M.S. Darwish, N.H. Nguyen, A. Ševců, I.J.J.o.N. Stibor, Functionalized magnetic nanoparticles and their effect on Escherichia coli and Staphylococcus aureus, Journal of Nanomaterials, 2015 (2015).

[34] M. Zwietering, I. Jongenburger, F. Rombouts, K.J.A. Van't Riet, e. microbiology, Modeling of the bacterial growth curve, 56 (1990) 1875-1881.

[35] T.W. Almeida, D.R. Sampaio, A.C. Bruno, T.Z. Pavan, A.A. Carneiro, Comparison between shear wave dispersion magneto motive ultrasound and transient elastography for measuring tissue-mimicking phantom viscoelasticity, IEEE transactions on ultrasonics, ferroelectrics, and frequency control, 62 (2015) 2138-2145.

[36] E. Mazon, S. Arsalani, J.H. Uliana, A.A. Carneiro, A.J. Gualdi, T.Z. Pavan, A pulsed magnetomotive ultrasound imaging system for magnetic nanoparticle detection, in: 2021 IEEE UFFC Latin America Ultrasonics Symposium (LAUS), IEEE, 2021, pp. 1-4.

[37] D.R.T. Sampaio, F.W. Grillo, A.C. Bruno, T.Z. Pavan, A.A.O.J.R.o.B.E. Carneiro, A magneto-motive ultrasound platform designed for pre-clinical and clinical applications, Research on Biomedical Engineering, 32 (2017) 337-346.

[38] Y. Hadadian, M. Azimbagirad, E.A. Navas, T.Z.J.R.o.S.I. Pavan, A versatile induction heating system for magnetic hyperthermia studies under different experimental conditions, 90 (2019) 074701.

[39] M. Kallumadil, M. Tada, T. Nakagawa, M. Abe, P. Southern, Q.A.J.J.o.M. Pankhurst, M. Materials, Suitability of commercial colloids for magnetic hyperthermia, 321 (2009) 1509-1513.

[40] G. Antarnusa, Y.R. Denny, A. Suherman, I.S. Utami, A.J.R.I.i.C.E. Saefullah, The Effect of Additional Polyethylene Glycol (PEG) as Coating Fe3O4 for Magnetic Nanofluid Applications, Recent Innovations in Chemical Engineering, 14 (2021) 335-346.

[41] V. Baldim, N. Yadav, N. Bia, A. Graillot, C. Loubat, S. Singh, A.S. Karakoti, J.-F. Berret, Polymer-Coated Cerium Oxide Nanoparticles as Oxidoreductase-like Catalysts, ACS Applied Materials & Interfaces, 12 (2020) 42056-42066.

[42] A. Alemdar, N. Güngör, O.I. Ece, O. Atici, The rheological properties and characterization of bentonite dispersions in the presence of non-ionic polymer PEG, J. Mater. Sci., 40 (2005) 171-177.

[43] Z. Cao, S. Jiang, Super-hydrophilic zwitterionic poly(carboxybetaine) and amphiphilic non-ionic poly (ethylene glycol) for stealth nanoparticles, Nano Today, 7 (2012) 404-413.

[44] J. Jiang, G. Oberdörster, P. Biswas, Characterization of size, surface charge, and agglomeration state of nanoparticle dispersions for toxicological studies, J. Nanopart. Res., 11 (2009) 77-89.

[45] F.T.L. Muniz, M.R. Miranda, C. Morilla dos Santos, J.M.J.A.C.S.A.F. Sasaki, Advances, The Scherrer equation and the dynamical theory of X-ray diffraction, 72 (2016) 385-390.

[46] M. Mahdavi, M.B. Ahmad, M.J. Haron, F. Namvar, B. Nadi, M.Z.A. Rahman, J.J.M. Amin, Synthesis, surface modification and characterisation of biocompatible magnetic iron oxide nanoparticles for biomedical applications, 18 (2013) 7533-7548.

[47] M. Szekeres, I.Y. Tóth, E. Illés, A. Hajdú, I. Zupkó, K. Farkas, G. Oszlánczi, L. Tiszlavicz, E.J.I.j.o.m.s. Tombácz, Chemical and colloidal stability of carboxylated core-shell magnetite nanoparticles designed for biomedical applications, 14 (2013) 14550-14574.

[48] S. Honary, F.J.T.J.o.P.R. Zahir, Effect of zeta potential on the properties of nano-drug delivery systems-a review (Part 1), Tropical Journal of Pharmaceutical Research, 12 (2013) 255-264.

[49] Y. Hadadian, D.R.T. Sampaio, A.P. Ramos, A.A.O. Carneiro, M. Mozaffari, L.C. Cabrelli, T.Z. Pavan, Synthesis and characterization of zinc substituted magnetite nanoparticles and their application to magneto-motive ultrasound imaging, Journal of Magnetism and Magnetic Materials, 465 (2018) 33-43.

[50] I. Karimzadeh, H.R. Dizaji, M.J.M.R.E. Aghazadeh, Preparation, characterization and PEGylation of superparamagnetic Fe3O4 nanoparticles from ethanol medium via cathodic electrochemical deposition (CED) method, Materials Research Express, 3 (2016) 095022.

[51] E.K. Larsen, T. Nielsen, T. Wittenborn, H. Birkedal, T. Vorup-Jensen, M.H. Jakobsen, L. Østergaard, M.R. Horsman, F. Besenbacher, K.A.J.A.n. Howard, Size-dependent accumulation of PEGylated silane-coated magnetic iron oxide nanoparticles in murine tumors, ACS nano, 3 (2009) 1947-1951.

[52] Y. Junejo, A. Baykal, H.J.O.C. Sözeri, Simple hydrothermal synthesis of Fe3O4-PEG nanocomposite, Open Chemistry, 11 (2013) 1527-1532.

[53] L. Wittmann, C. Turrina, S.P.J.M. Schwaminger, The Effect of pH and Viscosity on Magnetophoretic Separation of Iron Oxide Nanoparticles, Magnetochemistry, 7 (2021) 80.

[54] S. Arsalani, N. Löwa, O. Kosch, P. Radon, O. Baffa, F.J.P.i.M. Wiekhorst, Biology, Magnetic separation of iron oxide nanoparticles to improve their application for magnetic particle imaging, Physics in Medicine & Biology, 66 (2021) 015002.

[55] G. Antarnusa, P.D. Jayanti, Y.R. Denny, A. Suherman, Utilization of co-precipitation method on synthesis of Fe3O4/PEG with different concentrations of PEG for biosensor applications, Materialia, 25 (2022) 101525.

[56] G. Kandasamy, D. Maity, Recent advances in superparamagnetic iron oxide nanoparticles (SPIONs) for in vitro and in vivo cancer nanotheranostics, International Journal of Pharmaceutics, 496 (2015) 191-218.

[57] J. Mohapatra, A. Mitra, D. Bahadur, M. Aslam, Surface controlled synthesis of MFe2O4 (M = Mn, Fe, Co, Ni and Zn) nanoparticles and their magnetic characteristics, CrystEngComm, 15 (2013) 524-532.

[58] C.R. Vestal, Z.J. Zhang, Effects of Surface Coordination Chemistry on the Magnetic Properties of MnFe2O4 Spinel Ferrite Nanoparticles, J. Am. Chem. Soc., 125 (2003) 9828-9833.
[59] N. Cordente, M. Respaud, F. Senocq, M.-J. Casanove, C. Amiens, B. Chaudret, Synthesis and Magnetic Properties of Nickel Nanorods, Nano Lett., 1 (2001) 565-568.
[60] P. de la Presa, M. Multigner, J. de la Venta, M.A. García, M.L. Ruiz-González, Structural and magnetic characterization of oleic acid and oleylamine-capped gold nanoparticles, J. Appl. Phys., 100 (2006) 123915.
[61] S.S. Behera, J.K. Patra, K. Pramanik, N. Panda, H. Thatoi, Characterization and evaluation of antibacterial activities of chemically synthesized iron oxide nanoparticles, World Journal of Nano Science and Engineering, (2012).
[62] L. Zhang, Y. Jiang, Y. Ding, M. Povey, D. York, Investigation into the antibacterial behaviour of suspensions of ZnO nanoparticles (ZnO nanofluids), J. Nanopart. Res., 9 (2007) 479-489.
[63] J.S. Kim, E. Kuk, K.N. Yu, J.-H. Kim, S.J. Park, H.J. Lee, S.H. Kim, Y.K. Park, Y.H. Park, C.-Y. Hwang, Y.-K. Kim, Y.-S. Lee, D.H. Jeong, M.-H. Cho, Antimicrobial effects of silver nanoparticles, Nanomedicine: Nanotechnology, Biology and Medicine, 3 (2007) 95-101.
[64] B. Stephen Inbaraj, T.-Y. Tsai, B.-H. Chen, Synthesis, characterization and antibacterial activity of superparamagnetic nanoparticles modified with glycol chitosan, Sci. Technol. Adv. Mater., 13 (2012) 015002.
[65] A. Rajabi, M.J. Ghazali, E. Mahmoudi, A.H. Baghdadi, A.W. Mohammad, N.M. Mustafah, H. Ohnmar, A.S. Naicker, Synthesis, Characterization, and Antibacterial Activity of Ag2O-Loaded Polyethylene Terephthalate Fabric via Ultrasonic Method, Nanomaterials, 9 (2019) 450.
[66] R. Buchanan, R. Whiting, W.J.F.m. Damert, When is simple good enough: a comparison of the Gompertz, Baranyi, and three-phase linear models for fitting bacterial growth curves, 14 (1997) 313-326.
[67] M. Naseroleslami, K. Parivar, S. Khoei, N.J.C.J. Aboutaleb, Magnetic resonance imaging of human-derived amniotic membrane stem cells using PEGylated superparamagnetic iron oxide nanoparticles, Cell Journal (Yakhteh), 18 (2016) 332.
[68] M. Ayubi, M. Karimi, S. Abdpour, K. Rostamizadeh, M. Parsa, M. Zamani, A.J.M.S. Saedi, E. C, Magnetic nanoparticles decorated with PEGylated curcumin as dual targeted drug delivery:

Synthesis, toxicity and biocompatibility study, Materials Science and Engineering, 104 (2019) 109810.

[69] G. Liu, Y. Li, L. Yang, Y. Wei, X. Wang, Z. Wang, L.J.R.a. Tao, Cytotoxicity study of polyethylene glycol derivatives, RSC advances, 7 (2017) 18252-18259.

[70] J.A. Roacho-Pérez, F.G. Ruiz-Hernandez, C. Chapa-Gonzalez, H.G. Martínez-Rodríguez, I.A. Flores-Urquizo, F.E. Pedroza-Montoya, E.N. Garza-Treviño, M. Bautista-Villareal, P.E. García-Casillas, C.N.J.P. Sánchez-Domínguez, Magnetite nanoparticles coated with PEG 3350-Tween 80: In vitro characterization using primary cell cultures, Polymers, 12 (2020) 300.

[71] B. Alberts, A. Johnson, J. Lewis, M. Raff, K. Roberts, P. Walter, The compartmentalization of cells, in: Molecular Biology of the Cell. 4th edition, Garland Science, 2002.

[72] M. Yu, S. Huang, K.J. Yu, A.M.J.I.j.o.m.s. Clyne, Dextran and polymer polyethylene glycol (PEG) coating reduce both 5 and 30 nm iron oxide nanoparticle cytotoxicity in 2D and 3D cell culture, international journal of molecular sciences, 13 (2012) 5554-5570.

[73] Q. Feng, Y. Liu, J. Huang, K. Chen, J. Huang, K. Xiao, Uptake, distribution, clearance, and toxicity of iron oxide nanoparticles with different sizes and coatings, Sci. Rep., 8 (2018) 2082.

[74] R.E.J.J.o.m. Rosensweig, m. materials, Heating magnetic fluid with alternating magnetic field, 252 (2002) 370-374.

Chapter 3. Hybrid Nanoparticles of Citrate Coated Manganese Ferrite and Gold Nanorods in Magneto-optical Imaging and Thermal Therapy

Abstract

The development of nanomaterials has drawn considerable attention in nanomedicine to advance cancer diagnosis and treatment over the last decades. Gold nanorods (GNRs) and magnetic nanoparticles (MNPs) have been known as the most common nanostructures in biomedical applications due to their attractive optical properties and superparamagnetic (SP) behaviors, respectively. In this study, we proposed a simultaneous and simple combination of plasmonic and SP properties to produce hybrid NPs of citrate coated manganese ferrite (Ci-$MnFe_2O_4$) and cetyltrimethylammonium bromide coated GNRs (CTAB-GNRs). In this regard, two different samples were prepared: the first one was only made of Ci-$MnFe_2O_4$ (0.4 wt%), and the second one contained hybrid NPs of Ci-$MnFe_2O_4$ (0.4 wt%) and CTAB-GNRs (0.04 wt%). Characterization measurements such as UV-Visible spectroscopy and transmission electron microscopy (TEM) revealed electrostatic interactions caused by the opposing surface charges of hybrid NPs, which resulted in the formation of small nanoclusters. The performance of two samples was investigated using magneto-motive ultrasound imaging (MMUS). The sample containing Ci-$MnFe_2O_4$_CTAB-GNRs demonstrated a displacement nearly two-fold greater than just using Ci-$MnFe_2O_4$. Furthermore, the preliminary potential of these hybrid NPs was also examined in magnetic hyperthermia (MH) and photoacoustic imaging (PAI) modalities. Lastly, this hybrid NPs reported high stability and an absence of aggregation in water and PBS medium. Thus, Ci-$MnFe_2O_4$_CTAB-GNRs hybrid NPs can be considered as a potential contrast agent in MMUS, PAI, and heat generator in MH.

3. Introduction

Nanomaterials have been widely exploited in biomedical applications over the past few decades [1-3]. As an example, gold nanorods (GNRs) are known as promising candidates due to their biocompatibility [4], being well-defined in terms of size, and having tunable localized surface plasmon resonance [5]. As a result of these striking properties, GNRs have attracted significant interest in light-based imaging modalities and therapeutic techniques such as photoacoustic imaging (PAI) and photothermal therapy [4, 6-8]. In addition, magnetic nanoparticles (MNPs) have been extensively used in a variety of applications such as biology and biomedicine, owing to their unique features [9-17]. Manganese ferrites ($MnFe_2O_4$) are one interesting spinel ferrite NPs among the various mixed ferrites (AFe_2O_4) with other transition metal ions (e.g., A = Mn, Ni, Cu, and Zn) due to their biocompatibility, saturation magnetization, and chemical stability [18-23]. Considering these advantages of $MnFe_2O_4$, they are promising candidates to develop theranostic platforms, particularly in the field of personalized nanomedicine like magnetic resonance imaging (MRI) [24, 25] and magnetic hyperthermia (MH) [26-28].

Some researchers have combined the benefits of iron oxide nanoparticles (IONPs) and GNRs in magnetic and optical/thermal imaging modalities [29-31]. For example, in photoacoustic imaging (PAI), endogenous chromophores in tissue such as melanin and hemoglobin can generate a noticeable signal. This reduces the sensitivity of photoacoustic imaging to identify the desired contrast agent, in other words the region marked with the plasmonic nanoparticles. As a result, PAI and MMUS can be integrated to overcome this barrier by combining magneto-plasmonic NPs [29-33]. Qu *et al*. created liposomes encapsulating IONPs (Fe_3O_4) and GNRs as a dual contrast agent for magneto-photoacoustic imaging to improve contrast in both *ex vivo* and *in vivo* studies [29, 32, 34]. Furthermore, the same group suggested using nanoclusters containing gold nanospheres and IONPs in MMUS imaging to improve the accuracy of effective photothermal therapy (PTT). More specifically, MMUS imaging can assess tissue elasticity, which has been identified as a critical parameter in PTT efficiency evaluation [33]. Although several studies have been conducted using magneto-plasmonic NPs in biomedical applications, contrast enhancement using citrate coated manganese ferrite (Ci-$MnFe_2O_4$) and

cetyltrimethylammonium bromide coated GNRs (CTAB-GNRs) hybrid NPs in MMUS has not previously been reported.

In the current study, we suggested a hybrid NP made of Ci-$MnFe_2O_4$ and CTAB-GNRs through a simple combination in which CTAB-GNRs were synthesized using a gold seed-mediated method [35]. Zufelato *et al.* [27] manufactured $MnFe_2O_4$ coated with sodium citrate via the coprecipitation route. The interaction of these NPs was investigated using several characterizations, including a magnetic separation system (SEPMAG), UV-Visible spectroscopy, transmission electron microscopy (TEM), and attenuated total reflection (ATR). To highlight their stability in physiological media, the colloidal stability of hybrid NPs in phosphate buffer solution (PBS) at pH 7.4 (physiological pH) was also studied. Moreover, the performance of using only Ci-$MnFe_2O_4$ and its combination with CTAB-GNRs was investigated in MMUS, as well as their preliminary potential in the PAI and MH.

3.1. Materials

The chemical reagents used were: cetyltrimethylammonium bromide (CTAB), sodium borohydride ($NaBH_4$), tetrachloroauric acid ($HAuCl_4.4H_2O$), silver nitrate ($AgNO_3$), and L-ascorbic acid (AA), which were purchased from Sigma, Aldrich, Vetec, and Panreac, respectively. Milli-Q water was also used for the preparation and washing solutions.

3.2. Methods

3.2.1. Preparation of Ci-$MnFe_2O_4$ NPs

Ci-$MnFe_2O_4$ NPs were synthesized via the coprecipitation route by Zufelato *et al*. [27]. The core, crystal, hydrodynamic sizes, and polydispersity index (PDI) of these MNPs were 16.7, 14, 38, nm, and 0.32, respectively. In addition, Ci-$MnFe_2O_4$ had a saturation magnetization of 52.54 emu/g (in powder). For further information about MNPs synthesis and characterization, the reader is referred to the Supplementary Material (Figures 3S1a–c and 3S2).

3.2.2. Preparation of CTAB-GNRs

GNRs coated by CTAB were manufactured in two steps according to the study of Morasso *et al*. [35]: Preparation of gold seed NPs and growth solution.

3.2.2.1. Gold seed NPs

Gold seeds were synthesized according to the study by Morasso *et al*. [35] with only one modification by replacing hydroquinone (acting as a reducing agent) with AA. First, a 5 ml tetrachloroauric acid ($HAuCl_4$) solution of 0.5 mM was added to the CTAB solution (200 mM) at 40 °C. Next, 0.6 ml of 10 mM freshly ice-cold sodium borohydride ($NaBH_4$) was added under vigorous stirring. The mixture's color changed rapidly to light brown, confirming the formation of small gold NPs [5, 35]. The stirring was continued for 20 more minutes. A schematic illustration of the gold seed preparation is shown in Figure 3S3a.

3.2.2.2. Preparation of growth solution

In the next step (the growth solution), we added 55 µL of AA, 200 µL of silver nitrate ($AgNO_3$) solution (4 mM), and 5 ml of tetrachloroauric acid ($HAuCl_4$) solution (1 mM), respectively, to 80 mM of CTAB under vigorous stirring. Thereafter, 12 µL seed suspension was added to the growth solution [35], Figure 3S3b. The mixture was then stirred for 60 minutes. The color of the solutions changed to light ruby after 20 minutes, indicating the formation of GNRs.

3.2.2.3. Purification of CTAB-GNRs

As mentioned earlier, the GNRs were stabilized by CTAB; therefore, the suspension containing CTAB-GNRs was centrifuged to remove any excess of CTAB due to its cytotoxicity. The GNRs were precipitated at the bottom of the solvent after 8 minutes of centrifugation at 7000 rpm (Eppendorf 5415D Microcentrifuge with Rotor F45-24-11). The GNRs were then resuspended in Milli-Q water, depending on the amount of residue. Finally, the GNR suspension was kept at room temperature.

3.2.3. Preparation of Ci-$MnFe_2O_4$_CTAB-GNRs hybrid NPs

The concentrations of the stock dispersion of CTAB-GNRs and Ci-$MnFe_2O_4$ were 0.35 wt% and 3 wt%, respectively. A hybrid NPs dispersion with lower concentration was papered for both MMUS and MH experiments, such that it consisted of 0.04 wt% CTAB-GNRs and 0.4% Ci-$MnFe_2O_4$ NPs. The MMUS experiments were conducted using samples of 900 µl volume;

that is, 103 µl of CTAB-GNRs and 120 µl of Ci-$MnFe_2O_4$ taken from their corresponding stock and dispersed in solution of 6 wt% gelatin to reach the final volume of 900 µl. For MH experiments the samples were prepared by dispersing 66 µl Ci-$MnFe_2O_4$ and 57 µl CTAB-GNRs of the stocks in water to reach the final volume of 500 µl (the same concentration as in MMUS samples). Prior to the experiments, these hybrid NPs were mixed using a 3D rotation for 24 hours to allow their interactions occur.

3.3. Characterization of NPs

Various techniques were used to characterize NPs. Spectrophotometric analysis in the visible-near infrared region was used to determine the optical properties that provide information about the size of the gold seeds and GNRs via the plasmonic band and to investigate the interaction of Ci-$MnFe_2O_4$ _CTAB-GNRs using a UV spectrometer (Ultrospec 2100 pro) with a resolution of 0.5 nm operating in the wavelength range of 200-900 nm. Furthermore, TEM measurements were performed on a JEOL-JEM-100 CXII to verify the structure and size of GNRs, Ci-$MnFe_2O_4$, as well as to confirm the electrostatic interaction of hybrid NPs made of manganese ferrite and GNRs. A droplet of the desired suspension was dried on the copper grid at room temperature for TEM samples. The ImageJ software program was used to calculate mean diameters from TEM images (above 200 particles per sample were counted). The Origin® software was then used to plot the histograms of TEM images.

XRD (D5005 Diffractometer, Bruker) analysis was used to determine the crystalline properties and phase identification, with X-ray beam nickel-filtered copper K radiation (=1.5406) in the range $10° < 2\theta° < 70°$. Next, the hydrodynamic diameter, PDI and zeta potential of NPs were determined by dynamic light scattering (DLS) and using a Zetasizer Nano ZS (Malvern-UK). The data was measured at a fixed angle (173°) and an Nd: YAG laser (532 nm). Following that, an attenuated total reflectance (ATR) accessory coupled to a Fourier-transform infrared spectrophotometer (FTIR) was used to investigate CTAB molecule binding on the surface of GNRs, the functionalization surface of $MnFe_2O_4$ coated with sodium citrate, and particle interaction. Next, the magnetic properties of Ci-$MnFe_2O_4$ and its combination with CTAB-GNRs were investigated by a vibrating sample magnetometer (VSM, EG&G Princeton Applied Research Magnetometer) at room temperature and on powder samples. Then, a magnetic

separation system (SEPMAG, Barcelona, Spain) was used to verify the interactions between Ci-$MnFe_2O_4$ and CTAB-GNRs. More details about magnetic separation measurement are described in the following section.

3.3.1. Magnetic Separation

A magnetic separation system was used to measure the separation time of the abovementioned NPs, which highly depends on particle size distribution [11, 36]. In this study, we applied a magnetic separation system (SEPMAG) to examine the interaction between Ci-$MnFe_2O_4$ and CTAB-GNRs by measuring the separation time of Ci-$MnFe_2O_4$ and Ci-$MnFe_2O_4$ _CTAB-GNRs samples, separately.

This system is based on the movement of MNPs under the influence of magnetic field gradients. This phenomenon is known as magnetophoresis, which is defined by the magnetophoretic velocities of the MNPs as a result of the separation time parameter [37, 38]. The equipment contains two small cylindrical cavities with a volume of 2 mL and a third with a larger volume (15 ml). In this device, a homogeneous magnetic gradient of 15 T/m was applied by permanent magnets to create uniform magnetophoretic conditions for the three cavities. The magnetic force acting on magnetic particles can be defined as follows [39, 40]:

$$F = m\mu_0 \frac{\partial H}{\partial r} \qquad (3.1)$$

in which: μ_0 is the vacuum magnetic permeability constant, $\frac{\partial H}{\partial r}$ is the radial component of the magnetic gradient, and m is the magnetic moment of the particle, which is expressed as follows:

$$m = \mathrm{M}_s . \rho_\rho . \frac{4}{3} . \pi . R^3 \qquad (3.2)$$

M_S, ρ_ρ, and R are the saturation magnetization per unit mass of the colloid, the particle density, and the particle hydrodynamic radius, respectively. There is also the drag force opposing the magnetic field motion, which is given by [39]:

$$F_d = 6\pi\eta Rv \tag{3.3}$$

In which: η is the viscosity of the fluid, and v is the velocity of the particles. Therefore, the particles move toward the walls with a magnetophoretic velocity determined by the balance of the forces in equations (3.1) and (3.2) [41, 42]:

$$v = \frac{2M_s . \rho_\rho . R^2}{9\eta} \tag{3.4}$$

It should be noted that this system includes an optical sensor for measuring the transmitted light, which is produced by a LED array. The opacity of the sample changes over time during the process [36]. To be more precise, the maximum opacity is observed at the beginning of the process (t_0) due to the solution's homogeneity. Half separation time (t_{50}), which is the time when the opacity decreases by 50%, is employed to examine the magnetophoretic behavior of the samples. A schematic illustration of the magnetic separation process is shown in Figure 3.1.

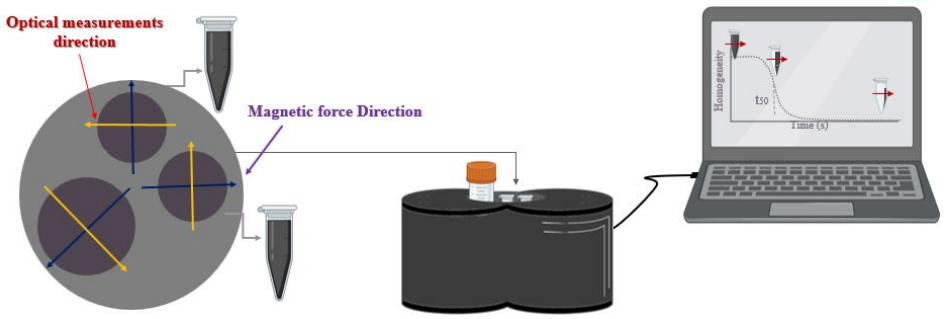

Figure 3.1. A schematic top view of the magnetic separation setup has three cavities with a volume of 2 ml for two tubes and 15 ml for the third tube. The red arrows indicate the movement of MNPs under the influence of magnetic field gradients.

3.4. Gelatin tissue-mimicking phantom

Gelatin/agar tissue-mimicking phantoms were prepared to perform the MMUS and PAI experiments. This preparation consists of two steps. First, the inclusion was prepared using a hemispherical mold (1 cm in diameter). To do so, 6 wt% gelatin (GELITA, São Paulo, Brazil)

was dissolved in deionized water at 25 °C and heated to 70 °C to obtain a homogeneous solution. When the temperature reached 70 °C, the solution was kept at room temperature and slowly mixed to cool down to 40 °C; formaldehyde was then added considering 5 wt% of the gelatin's mass [43]. Finally, the phantom was placed in the refrigerator for 24 hours [3]. Three different inclusions were manufactured as follows: the first inclusion was made of only 0.40 wt% Ci-$MnFe_2O_4$, the second was prepared using a hybrid NPs of 0.40 wt% Ci-$MnFe_2O_4$_0.04 wt% CTAB-GNRs, and the last sample was also made of hybrid NPs with the concentration of GNRs increased to 0.07 wt%. Since this study mainly focused on magnetic applications, low concentrations of CTAB-GNRs (0.04 and 0.07 wt%) were utilized to investigate their impact after mixing with 0.40 wt% Ci-$MnFe_2O_4$ on the MMUS contrast.

The next step was to assemble phantom backgrounds with a cylindrical mold (7 cm in diameter and 2.5 cm in height). This phantom was made using the same procedures as previously mentioned for inclusion preparation [11], but with a single modification of mixing 6 wt% gelatin with 3 wt% agar (HIMEDIA supplied Bacteriologic CAT. RM026). In this case, the solution was heated to 90 °C to achieve a uniform mixture. Three samples of each phantom type were created for a total of six phantoms.

3.5. MMUS experimental setup

The MMUS experimental setup consisted of a coil with 130 turns, an inner diameter of 22 mm, 114.2 μH of inductance, and 217.9 mΩ of DC resistance. A steel core of 20 mm diameter with a coercivity of 20 A/m was inserted in the center of the coil to enhance and focus the magnetic field. The tip of the steel core was positioned 2 mm away from the phantom's central region. The system also included a half-drive inverter to charge the capacitor bank once it reached the desired voltage. After charging the capacitor, an electronic switching device and the coil generated the magnetic field pulse. For further information about the MMUS setup, please refer to Mazon *et al*. [44]. A multichannel ultrasound pulse/echo system (Sonix RP + Sonix DAQ, Ultrasonix) was then used to track the induced displacement of the internal structure (in order of micrometer) by a cross-correlation method [45]. It should be mentioned that the US acquisition was synchronized with the magnetic excitation through a computer using a LabVIEW interface. This system operated with a frame rate of 4 kHz, and the magnetic pulse duration

varied from 4 to 8 ms [44]. The maximum magnetic field applied 2 mm from the tip of the core was 740 mT. A schematic of the pulsed MMUS setup is shown in Figure 3S-4.

3.6. PAI setup

The PAI measurements were carried out using an Nd: YAG laser (Brilliant B, Quantel) coupled to an optical parametric oscillator (MagicPRISM, Opotek). The optical beam was delivered to the phantom via a trifurcated optical fiber bundle (77536, Newport) attached to a linear L14-5/38 ultrasound transducer (Ultrasonix Medical Corp, Richmond, Canada). A parallel acquisition module (SonixDAQ, Ultrasonix) was used to collect PA data [46]. GNRs are commonly used as photo-absorbers in PA due to their excellent optical absorption property; the first phantom was made using only a low concentration of CTAB-GNRs (0.04 wt%). The second and third phantoms contained 0.4 wt% Ci-$MnFe_2O_4$, and hybrid NPs of 0.4 wt% Ci-$MnFe_2O_4$ _0.04 wt% CTAB-GNRs, respectively, similar to those used for MMUS. Thus, the potential of hybrid NPs for PAI was examined. For each phantom, 49 frames were acquired and averaged to obtain the PA images using the optical wavelength of 750 nm, corresponding to the longitudinal absorption peak of the CTAB-GNRs. The laser energy level was recorded to compensate for pulse-to-pulse variation, and the beam mean energy at the phantom surface was 10.30 ± 0.37 mJ, 10.23 ± 0.38 mJ, and 9.71 ± 0.39 mJ, for phantoms 1, 2, and 3, respectively.

3.7. MH experiments

This experiment was conducted using a homemade MH system [47]. The applied magnetic field had a sinusoidal and continuous profile with an amplitude of 10 mT at 132 kHz. Three samples containing Ci-MnFe2O4 (0.4 wt%) and the hybrid NPs of Ci-$MnFe_2O_4$ (0.4 wt%) _CTAB-GNRs (0.04 wt% and 0.07 wt%) were dispersed in Milli-Q water and positioned on a holder inside a solenoid. The diameter and height of this solenoid are 14 and 87 mm, respectively, and it can generate a homogeneous magnetic field across the entire sample volume. A fiber optic thermometer system (Qualitrol NOMAD-Touch Fiber Optic Monitor) was used to record the temperature of the samples [47-49]. Moreover, the power dissipated and converted into heat by both samples was calculated using the specific loss power (SLP) expression as shown below [48, 50]:

$$SLP = \frac{C_w m_w + C_{np} m_{np}}{m_{np}} \frac{\Delta T}{\Delta t} \qquad (3.5)$$

The Box–Lucas equation was used to fit the results of temperature versus time, according to the reference [50, 51] in which: C_{np} is the volume-specific heat capacity of the sample, m_{np} is the MNPs mass, m_w is the mass of the dispersion (which is water), and C_w is the specific heat capacity of water. In addition, the intrinsic loss power (ILP) was also calculated to provide a better comparison with the SLP values reported in other studies [49].

3.8. Results and Discussion

UV-Vis/near-infrared measurements of gold seeds were conducted to confirm the formation of gold seeds (3S-5a). Their size should be small (around 5 nm) to ensure that gold seed NPs could be used in the following procedure (growth solution). As a result, no plasmonic peak was expected to be observed in the range of 500 to 520 nm (3S-5a). In addition, the TEM image showed the generation of gold seeds with spherical morphology and a size of about 5 ± 1 nm (see 3S-5b), which agrees with the literature [35].

Furthermore, the UV-Visible spectra of CTAB-GNRs revealed transverse and longitudinal plasmon bands at 515 and 744 nm, respectively, providing information about the size and shape of GNRs (3S-6a). The TEM image of GNRs depicted that they are rod-shaped and uniform in size, Figure 2. The average length and width of CTAB-GNRs were 42.3 ± 4.1 nm and 15.31 ± 1.5 nm, respectively, with an aspect ratio of 2.76 (3S-6b, c).

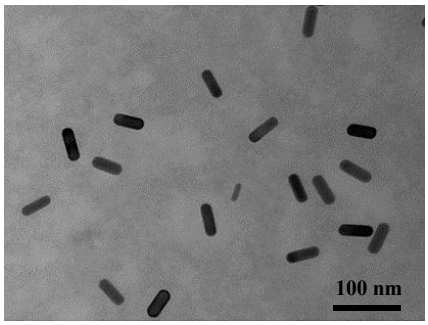

Figure 3.2. TEM images of CTAB-GNRs in the scale bare of 100 nm.

In this study, hybrid NPs containing 0.4 wt% Ci-$MnFe_2O_4$ and 0.04 wt% CTAB-GNRs were thoroughly investigated as follows. However, as another example, partial results of 0.4 wt% Ci-$MnFe_2O_4$ and 0.07 wt% CTAB-GNRs are presented here such as hydrodynamic size, Zeta potential, MMUS, and MH. The UV-Visible measurement was then carried out to confirm the interactions between CTAB-GNRs and Ci-$MnFe_2O_4$. The normalized spectrum of the suspension containing CTAB-GNRs, Ci-$MnFe_2O_4$, and hybrid NPs is shown in Figure 3.3.

The longitudinal peak of CTAB-GNRs can be seen at 744 nm, while the plasmonic band of GNRs showed a redshift to 764 nm after mixing with Ci-$MnFe_2O_4$. The band at 764 nm is related to the GNRs, revealing a redshift of the plasmonic band, which has a broader peak upon interaction with the Ci-$MnFe_2O_4$. Other studies have reported similar results [29, 32]. Furthermore, a small absorption peak at around 650 nm was observed for hybrid NPs (blue curve), that could be due to the formation of clusters, which decreases the extinction coefficient because of the presence of larger particles. As a result, the plasmonic intensity of the dipole mode decreases, making the plasmonic band of the GNRs with smaller aspect ratios more noticeable, which was previously embedded/hidden by the high intensity longer wavelength dipolar plasmon band [52-54].

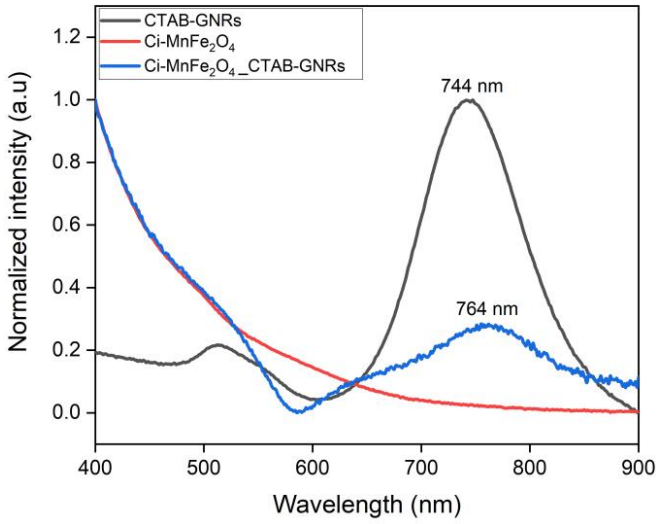

Figure 3.3. UV-Vis-NIR absorbance spectra of the solutions include GNRs (black), Ci-$MnFe_2O_4$ (red), and Ci-$MnFe_2O_4$ _CTAB-GNRs hybrid NPs (blue).

Figure 3.4a and b show TEM images of the interaction between Ci-$MnFe_2O_4$ _CTAB-GNRs hybrid NPs (red circles). Since the GNRs coated with CTAB had a positive surface charge, and the manganese ferrite stabilized by a capping agent of citrate had a negative surface charge, it was expected to generate an electrostatic attraction between these NPs (red circles). These results agree with the study by Truby [55], which showed excellent decoration of TREG SPIONs (positive charge) around the surface of the GNRs (negative charge) owing to charge affinity. In addition, small nanoclusters of Ci-$MnFe_2O_4$ were formed (yellow rectangular) after adding CTAB-GNRs to Ci-$MnFe_2O_4$ due to a charge imbalance in the medium. As expected, only a few CTAB-GNRs are observed compared to Ci-$MnFe_2O_4$ in the TEM images of hybrid NPs (Figures 4a and b). The reason could be the low amount of CTAB-GNRs used (0.04 wt%), while the concentration of Ci-$MnFe_2O_4$ used was much higher (nearly ten times greater (0.4 wt%) than CTAB-GNRs) in this study. Thus, more Ci-$MnFe_2O_4$ compared to CTAB-GNRs were expected to be observed in TEM images. The average particle size of nanoclusters was estimated to be around 48 ± 12 nm, Figure 3.4c.

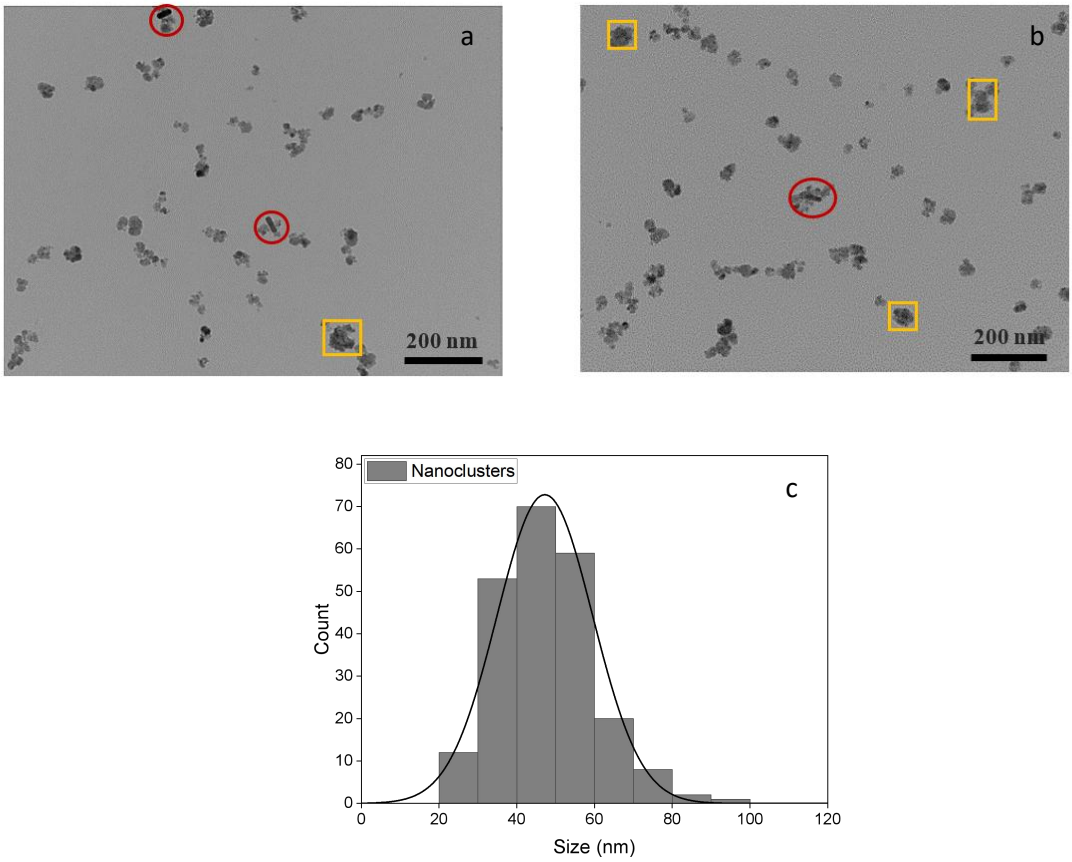

Figure 3.4. TEM images of nanoclusters of 0.4 wt% Ci-MnFe2O4 _0.04 wt% CTAB-GNRs hybrid NPs, in a scale bar of 200 nm.

Zeta potential was used to analyze the stability of the employed NPs (Table 1). GNRs coated with CTAB and $MnFe_2O_4$ capped with sodium citrate reported a Zeta potential of + 41 mV and – 43.5 mV, respectively, indicating that the nanoparticle surfaces were adequately coated and produced stable colloids, Table 1. After combining different concentrations of CTAB-GNRs with Ci-$MnFe_2O_4$, they maintained good stability at -30.4 mV and -31.1 mV. Following the classical colloidal theory, suspension stability can be interpreted as the balance between repulsive forces (with electrostatic origin) and attractive forces (generally associated with van der Waals interactions) [56]. The Zeta-potential values found for individual NPs (i.e., + 41 mV and – 43.5, respectively, CTAB-GNRs and Ci-$MnFe_2O_4$) correlate with a sufficient repulsive force to attain better physical colloidal stability. When these two particles interact, the net charge of the hybrid NPs decreases, and the electrostatic repulsion weakens [57]. This condition favors attractive forces to dominate the interaction between individual NPs of the

hybrid NPs, reducing the electrostatic stability (Zeta-potential = -30.4 mV and -31.1 mV for 0.4wt% $CiMnFe_2O_4$ _0.04 wt% CTAB-GNRs and 0.4 wt% $CiMnFe_2O_4$_0.07 wt% CTAB-GNRs, respectively). Also, the stability of hybrid NPs of 0.4 wt% Ci-$MnFe_2O_4$_0.04 wt% CTAB-GNRs was repeated after 6 months, and it maintained its stability (-31.6 mV) with no sedimentation. The colloidal stability of both hybrid NPs dispersed in PBS at pH 7.4 (physiological pH) was also investigated [58]. Surprisingly, in PBS buffer with pH 7.4, these hybrid NPs show high stability (Table 1), and after immersion in PBS medium, their average hydrodynamic sizes did not change. It should be noted that the minor difference in hydrodynamic size and PDI of hybrid NPs dispersed in water or buffer is most likely due to a difference in the concentration used, as DLS analysis is highly concentration dependent. Also, slightly higher PDI values after immersion in PBS could be attributed to the lack of ultrasonication for NPs prior to DLS measurements. As a result, these hybrid NPs could maintain their dispersion stability and absence of aggregation in physiological conditions.

Table 3.1. Zeta-potential, hydrodynamic size, and PDI of CTAB-GNRs, Ci-$MnFe_2O_4$, and hybrid NPs in water. Hybrid NPs were also examined in a PBS medium.

Samples	Solution	Zeta potential (mV)	Hydrodynamic size (nm)	PDI
CTAB-GNRs	Water	41	___	___
Ci-$MnFe_2O_4$	Water	-43.5	38	0.32
0.4 wt% Ci-$MnFe_2O_4$_0.04 wt% CTAB-GNRs	Water	-30.4	43	0.34
0.4 wt% Ci-$MnFe_2O_4$_0.07 wt% CTAB-GNRs	Water	-31.1	37.5	0.33
0.4 wt% Ci-$MnFe_2O_4$_0.04 wt% CTAB-GNRs	PBS	-37.3	38	0.4
0.4 wt% Ci-$MnFe_2O_4$_0.07 wt% CTAB-GNRs	PBS	-33.8	44	0.4

Some studies have suggested that the GNRs be overcoated with polyethylene glycol (PEG), polystyrene sulfonate (PSS), and polyallylamine hydrochloride (PAH) to improve the stability and overcome cytotoxicity of CTAB [8, 55, 59]. Meanwhile, other factors such as size and concentration influence the toxicity of GNRs and should be considered [8]. Our results reinforce the relevance of physical characterizations using physical phantoms for this kind of NPs prior to addressing safety and reliability issues before in vivo assays.

The ATR-FTIR spectra of CTAB-GNRs (blue line) confirmed the adsorption of the surfactant at the surface of NP (Figure 3.5) due to the presence of bands at 2848 and 2916 cm^{-1} assigned to the C–H symmetric and anti-symmetric stretching. The less intense band at 1480 cm^{-1} is related to the amine group of the quaternarium ammonium salt. Moreover, the region of 961.02 and 910.026 can be corresponded to the presence of $N(CH_3)_2$ group. The FTIR spectrum of Ci-$MnFe_2O_4$ (red line) exhibits the presence of bands at 1388 cm^{-1} and 1586 cm^{-1}, which are assigned to the symmetric and antisymmetric stretchings of C-O, respectively. The broad band related to the vibration of -OH at 3390 cm^{-1} also confirmed the existence of adsorbed citrate molecules on the $MnFe_2O_4$ surface. The displacement of the OH and C-O related bands in the FTIR spectrum of Ci-$MnFe_2O_4$_CTAB-GNRs (black line) to a lower/higher wavenumber suggests the interaction between the two NPs by hydrogen bonding [60] assisted by the presence of CTAB and citrate on the surfaces.

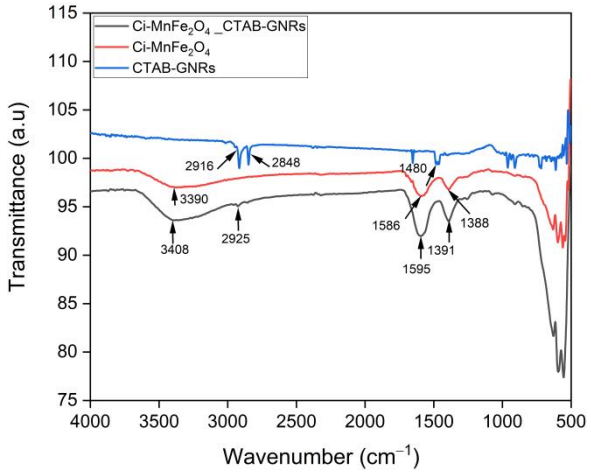

Figure 3.5. FTIR spectra of CTAB-GNRs, Ci-$MnFe_2O_4$, and their combination. The arrows indicate the main features of the spectra.

Furthermore, the magnetophoretic behavior of both samples was studied. Based on the obtained results, the separation time of Ci-$MnFe_2O_4$ (422.12 s) considering an intermediate stage (t_{50}) was significantly longer than that of Ci-$MnFe_2O_4$_CTAB-GNRs hybrid NPs (50.52 s), as shown in Figure 3.6, indicating the presence of larger NPs or clustering in the environment. According to Eq.1, the attractive magnetic force rises as the size of the hybrid NPs increases due to the presence of nanoclusters compared to Ci-$MnFe_2O_4$. Thus, hybrid NPs in the solution moved faster toward the tube wall (Eq. 4), resulting in a shorter separation time. These results can confirm the interactions between Ci-$MnFe_2O_4$ and CTAB-GNRs and the presence of larger hydrodynamic particle sizes. Our results agree with the study of Leonie Wittmann et al. [61], who investigated the effect of MNP movement along a magnetic field gradient on hydrodynamic particle size and found that larger NPs had a quicker separation time.

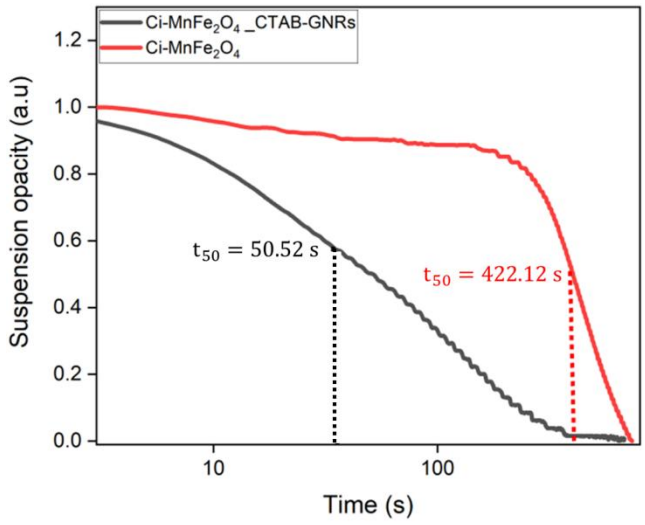

Figure 3.6. The magnetophoretic curve of Ci-$MnFe_2O_4$ and its combination with CTAB-GNRs.

Figure 3.7 shows the M-H curves of manganese ferrite capped citrate and its combination with CTAB-GNRs in the applied field of − 10 to + 10 kOe at room temperature, considering the total mass. The magnetization of both samples exhibits superparamagnetic behavior. The saturation magnetization for both samples (Ci-$MnFe_2O_4$ with and without GNRs) was almost the same at 52.54 emu/g and 52.8 emu/g, respectively. Since the CTAB-GNRs concentration was too low (0.04 wt.% for the hybrid NPs), there was no effect on the magnetization results, and both samples reported similar magnetization saturation in a high field (10 kOe).

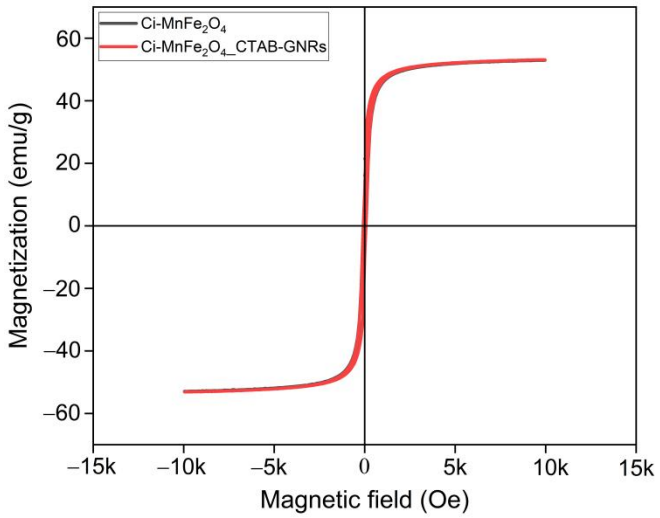

Figure 3.7. Magnetization curves of Ci-$MnFe_2O_4$ and its combination with CTAB-GNRs were recorded by a VSM, considering the total mass of each sample.

The next step was to perform the MMUS measurements using the gelatin-agar phantoms containing inclusions only labeled with Ci-$MnFe_2O_4$ (0.4 wt%) and a hybrid NPs of Ci-$MnFe_2O_4$ (0.4 wt%) _CTAB-GNRs (0.04 wt% and 0.07 wt%). For example, a B-mode and an MMUS image of a phantom containing hybrid NPs of 0.4 wt% Ci-$MnFe_2O_4$ _0.07 wt% CTAB-GNRs are illustrated in Figure 3.8a and b, respectively. Figure 3.8b depicts the induced displacement of approximately 30 μm, displaying the inclusion region (where the NPs are located). Figure 3.8c shows the induced displacements for three phantoms using three different magnetic pulse widths with the same magnetic field amplitude. The induced displacement of a phantom labeled with 0.4 wt% Ci-$MnFe_2O_4$_0.07 wt% CTAB-GNRs hybrid NPs was significantly greater at around 30.6 ± 4.16 μm than that of 0.4 wt% Ci-$MnFe_2O_4$_0.04 wt% CTAB-GNRs (19.42 ± 2.9 μm) and sample only labeled with 0.4 wt% Ci-$MnFe_2O_4$ (8 ± 1 μm). Mehrmohammadi and Yoon et al. [62, 63] also found that using small nanoclusters of MNP with a size of 55 nm resulted in higher displacements for pulsed MMUS than using individual MNPs. Hence, a similar outcome was observed in our work by generating nanoclusters, which agrees with Mehrmohammadi and Yoon et al. [62,63].

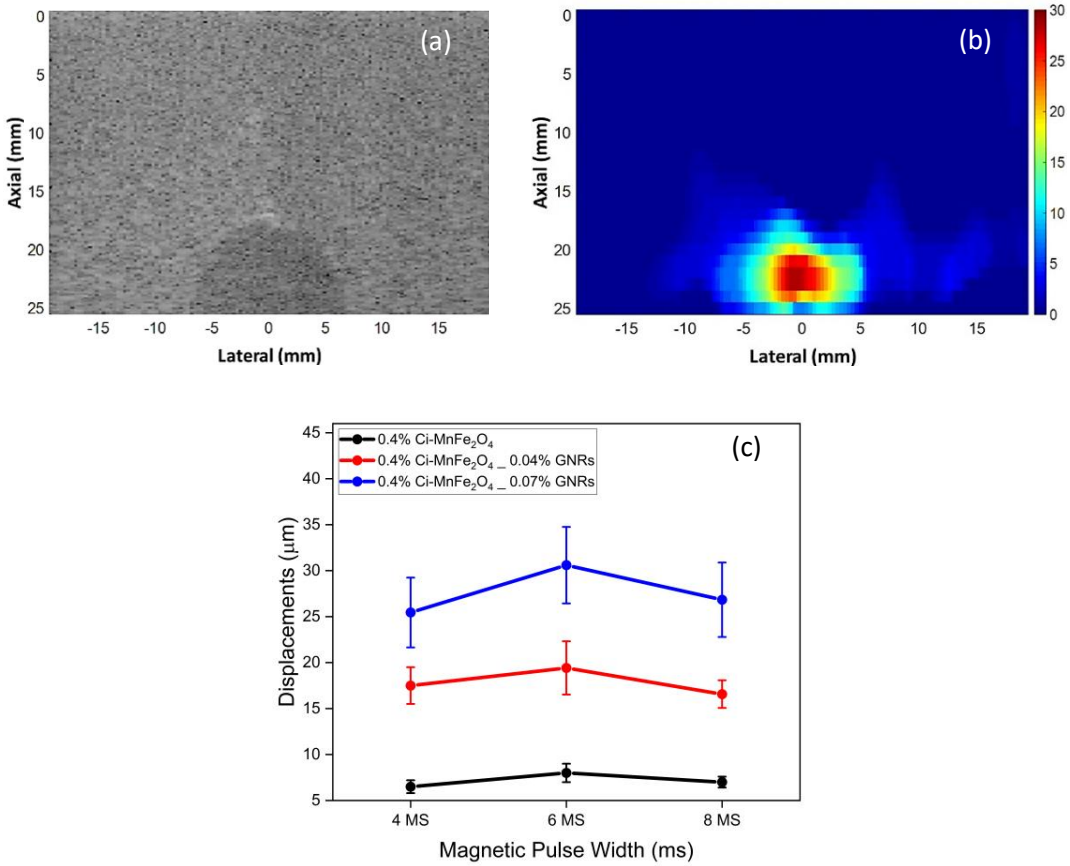

Figure 3.8. (a) The B-mode, (b) MMUS image of the phantom containing hybrid NPs of 0.4 wt% Ci-$MnFe_2O_4$ _0.07 wt% CTAB-GNRs, and (c) the induced displacements for phantoms containing Ci-$MnFe_2O_4$ and Ci-$MnFe_2O_4$ _CTAB-GNRs hybrid NPs.

Furthermore, since GNRs have remarkable optical properties, this hybrid NPs was also preliminarily examined as PAI contrast agents. Figure 3.9a represents the PA image for tissue-mimicking phantom only containing CTAB-GNRs (as an inclusion), and Figures 9b and c showed the images of the phantoms containing Ci-$MnFe_2O_4$ and hybrid NPs (Ci-$MnFe_2O_4$_CTAB-GNRs), respectively. Based on the results, although GNRs have been considered one of the most common metal NPs in PAI, the concentration used herein was very low (0.04 wt%), and therefore the obtained PA signal was not strong. The optical absorption for the next sample (only labeled with a high concentration of Ci-$MnFe_2O_4$) was boosted, which improved the image contrast, Figure 9b. The last sample (Figure 3.9c) containing the hybrid NPs also demonstrated a strong PA signal (like Figure 3.9b) since the number of particles increased by mixing Ci-$MnFe_2O_4$ and CTAB-GNRs. The signal-to-noise ratio (SNR) of the samples was

also depicted in Figure 3.9d, and based on the results, the sample containing hybrid NPs reported a larger SNR (152.7) than that of Ci-$MnFe_2O_4$ (142.6) and GNRs (90.03). Therefore, these hybrid NPs may be applied as a plausible contrast agent for PAI.

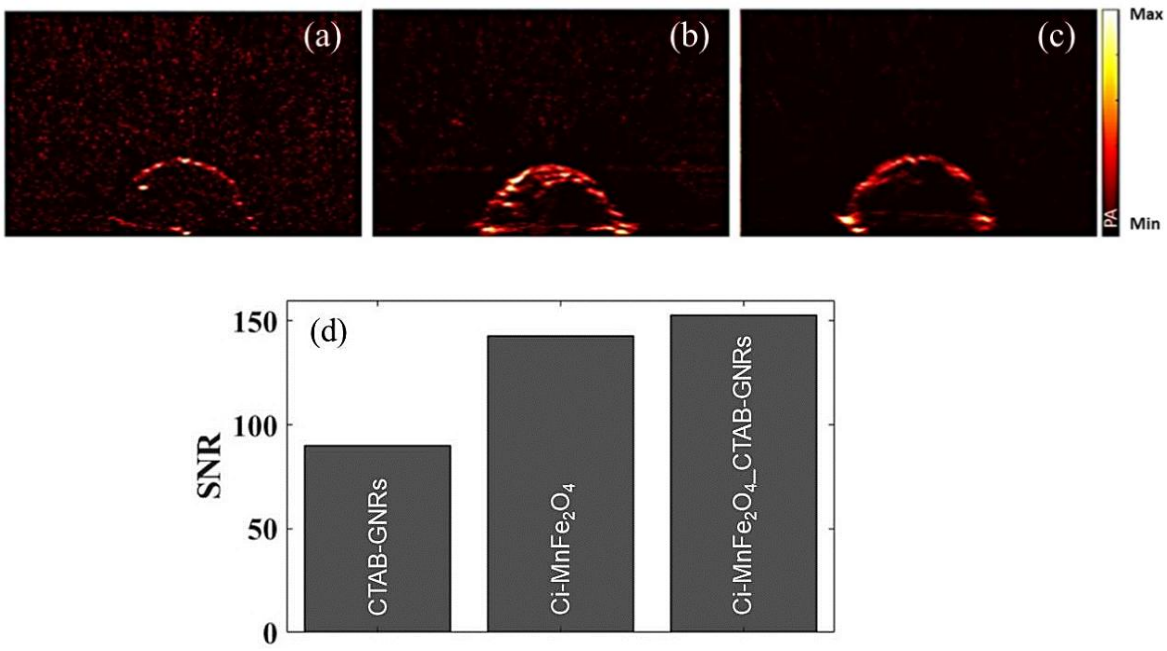

Figure 3.9. (a) PA images of the phantoms containing 0.04 wt% CTAB-GNRs, (b) 0.4 wt% Ci-$MnFe_2O_4$ and (c) 0.4 wt% Ci-$MnFe_2O_4$_ 0.04 wt% CTAB-GNRs. The images cover a 25 mm by 40 mm area. (d) The SNR of PAI using different phantoms.

Additionally, the potential of both hybrid NPs of Ci-$MnFe_2O_4$ _CTAB-GNRs was also initially verified in MH as another application using the magnetic field with characteristics described in section 2.7. Figure 3.10 shows the temperature variation as a function of time for all samples (0.4 wt% Ci-$MnFe_2O_4$ (sample 1), 0.4 wt% Ci-$MnFe_2O_4$_0.04 wt% CTAB-GNRs (sample 2), 0.4 wt% Ci-$MnFe_2O_4$_0.07 wt% CTAB-GNRs (sample 3)), and water (as a reference). SLP and ILP values of samples 1, 2, and 3 were 25.5 W/g, 3.02 nHm^2kg^{-1}, 24.6 W/g, 2.9 nHm^2kg^{-1}, and 23.8 W/g, 2.73 nHm^2kg^{-1}, respectively. Due to the low concentration of IONPs used, the samples' heating efficiency is less than 30 W/g. Although the SLP values, which are based on the initial slope of the heating curve, were almost similar for the three samples, the equilibrium temperature was higher for samples 2 and 3 (red and blue curves). One possible explanation is a better arrangement of magnetic anisotropy axes in the hybrid

nanoclusters, possibly during AC field excitation. Brownian rotation helps orienting the magnetic anisotropy axes of the MNPs, slightly enhancing the hyperthermia. Note that there is no contribution from the GNRs since the eddy's current loss in this size is negligible. Further studies may help to evaluate if the GNRs are influencing the Néel collective relaxation of the aggregates of Mn-ferrite NPs coupled to the GNRs [27]. Nevertheless, these hybrid NPs may be used similarly to Ci-$MnFe_2O_4$ as a feasible heat generator for MH.

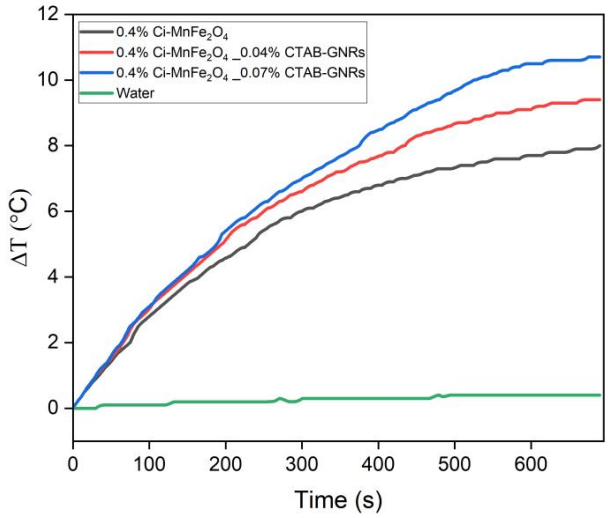

Figure 3.10. Temperature variation as a time function for Ci-$MnFe_2O_4$ and its combination with two different concentrations of CTAB-GNRs.

3.9. Conclusions

To conclude, hybrid NPs were prepared by a simple combination of positively charged GNRs coated with CTAB and negatively charged citrate-coated manganese ferrite. The electrostatic interaction of these NPs was studied using various characterizations, including UV visible, TEM, magnetic separation, and ATR. Interestingly, when the higher the concentration of GNRs was used, the greater the MMUS signal (induced displacement) from hybrid NPs based Ci-$MnFe_2O_4$_CTAB-GNRs was observed. The cause was the formation of nanoclusters, which improved contrast in MMUS. In this regard, more research will be conducted as a next step to determine the optimal concentration of GNRs to improve the contrast of MMUS in a subsequent study. Moreover, these potential candidates exhibited high stability and an absence of aggregation in the PBS medium. As a result, using the proposed multifunctional NPs for MMUS

reduces the required dosage of NPs while potentially minimizing side effects [33]. Nonetheless, more research is needed to confirm this contrast improvement in MMUS before using these particles *in vivo*. It should also be noted that the concentration of CTAB-GNRs in the hybrid NPs was significantly lower than Ci-$MnFe_2O_4$. Furthermore, another advantage of these hybrid NPs is their potential for use in MH therapy and PAI. Hence, these hybrid NPs could be used simultaneously in imaging and thermal therapy due to their dual magnetic susceptibility and optical properties.

Acknowledgments

The technical support given by Carlos Renato, Agnelo dos Santos Bastos Neto, Carlos A. Brunelo, Lourenco Rocha, and A. Maulin for the TEM images are greatly appreciated. We also thank Guilherme S. Pilotto Fernandes to help with PA measurements and profs. Adilson Jesus Aparecido de Oliveira and Alexandre José Gualdi for measuring the magnetization results.

References

1. Huang, X., S. Neretina, and M.A.J.A.m. El-Sayed, Gold nanorods: from synthesis and properties to biological and biomedical applications. Advanced materials, 2009. 21(48): p. 4880-4910.

2. Al-Eryani, Y., et al., Toxicity, therapeutic applicability, and safe handling of magnetic nanomaterials, in Magnetic Nanomaterials in Analytical Chemistry, 2021, Elsevier. p. 61-83.

3. Arsalani, S., et al., The effect of magnetization of natural rubber latex-coated magnetite nanoparticles on shear wave dispersion magneto-motive ultrasound. Physics in Medicine & Biology, 2019. **64**(21): p. 215019.

4. Durr, N.J., et al., Two-photon luminescence imaging of cancer cells using molecularly targeted gold nanorods. Nano letters, 2007. 7(4): p. 941-945.

5. Nikoobakht, B. and M.A. El-Sayed, Preparation and growth mechanism of gold nanorods (NRs) using seed-mediated growth method. American Chemical Society, 2003. **15**(10): p. 1957-1962.

6. Zhang, L., et al., Synthesis of gold nanorods and their functionalization with bovine serum albumin for optical hyperthermia.Journal of biomedical nanotechnology, 2014. **10**(8): p. 1440-1449.

7. Chen, Y.-S., et al., Miniature gold nanorods for photoacoustic molecular imaging in the second near-infrared optical window. Nature nanotechnology, 2019. **14**(5): p. 465-472.

8. Alkilany, A.M., et al., Cellular uptake and cytotoxicity of gold nanorods: molecular origin of cytotoxicity and surface effects. Advanced drug delivery reviews, 2009. 09. **5**(6): p. 701-708.

9. Arami, H., et al., In vivo delivery, pharmacokinetics, biodistribution and toxicity of iron oxide nanoparticles. Chemical Society Reviews, 2015. **44**(23): p. 8576-8607.

10. Dadfar, S.M., et al., Iron oxide nanoparticles: Diagnostic, therapeutic and theranostic applications. Advanced drug delivery review, 2019. **138**: p. 302-325.

11. Arsalani, S., et al., Uniform Size PEGylated Iron Oxide Nanoparticles as a Potential Theranostic Agent Synthesized by a Simple Optimized Coprecipitation Route. Journal of Magnetism and Magnetic Materials, 2022. **564**: p. 170091.

12. Arsalani, S., et al., Green Synthesis and Surface Modification of Iron Oxide Nanoparticles with Enhanced Magnetization Using Natural Rubber Latex. ACS Sustainable Chemistry & Engineering, 2018. **6**(11): p. 13756-13765.

13. Hadadian, Y., et al., Synthesis and characterization of zinc substituted magnetite nanoparticles and their application to magneto-motive ultrasound imaging. Journal of Magnetism and Magnetic Materials, 2018. **465**: p. 33-43.

14. Hadadian, Y., et al., From Low to High Saturation Magnetization in Magnetite Nanoparticles: The Crucial Role of the Molar Ratios Between the Chemicals, ACS Omega, 2022. **7**: p. 15996–16012.

15. Arsalani, S., et al., Magnetic Fe_3O_4 nanoparticles coated by natural rubber latex as MRI contrast agent. Journal of Magnetism and Magnetic Materials, 2019. **475**: p. 458-464.

16. Arsalani S, Radon P, Schier P, Jaufenthaler A, Liebl M, Baumgarten D, Wiekhorst F. Developing magnetorelaxometry imaging for human applications. Physics in Medicine & Biology. 2022. **67**(22): p. 225007.

17. Arsalani, S., et al. A Study on Magnetic Nanoparticles Concentration in Shear Wave Dispersion Magnetomotive Ultrasound. in XXVI Brazilian Congress on Biomedical Engineering. 2019. Springer.

18 Próspero, A.G., et al., Real-time in vivo monitoring of magnetic nanoparticles in the bloodstream by AC biosusceptometry. Journal of nanobiotechnology, 2017. **15**(1): p. 22.

19. Soares, G.A., et al., Multichannel AC Biosusceptometry system to map biodistribution and assess the pharmacokinetic profile of magnetic nanoparticles by imaging. IEEE transactions on nanobioscience, 2019. **18**(3): p. 456-462.

20. Prospero, A.G., et al., Corona protein impacts on alternating current biosusceptometry signal and circulation times of differently coated $MnFe_2O_4$ nanoparticles. Nanomedicine,2021. **16**(24): p. 2189-2206.

21. Quini, C.C., et al., Renal perfusion evaluation by alternating current biosusceptometry of magnetic nanoparticles. Journal of Magnetism and Magnetic Materials, 2015. **380**: p. 2-6.

22. Nunes, A.D., et al., Manganese ferrite-based nanoparticles induce ex vivo, but not in vivo, cardiovascular effects. International journal of nanomedicin, 2014. **9**: p. 3299.

23. Nunes, A.D., et al., Albumin Coating Prevents Cardiac Effect of the Magnetic Nanoparticles. IEEE transactions on nanobioscience, 2019. **18**(4): p. 640-650.

24. Yang, Y., et al., Graphene oxide/manganese ferrite nanohybrids for magnetic resonance imaging, photothermal therapy and drug delivery. Journal of biomaterials applications. 2016. **30**(6): p. 810-822.

25. Islam, K., et al., Manganese ferrite nanoparticles (MnFe2O4): Size dependence for hyperthermia and negative/positive contrast enhancement in MRI. Nanomaterials, 2020. **10**(11): p. 2297.

26. Branquinho, L.C., et al., Effect of magnetic dipolar interactions on nanoparticle heating efficiency: Implications for cancer hyperthermia. Scientific reports, 2013. **3**(1): p. 1-11.

27. Zufelato, N., et al., Heat Generation in Magnetic Hyperthermia by Manganese Ferrite-Based Nanoparticles Arises from Néel Collective Magnetic Relaxation. ACS Applied Nano Materials, 2022. **5**(5): p. 7521-7539.

28. Verde, E.L., et al., Field dependent transition to the non-linear regime in magnetic hyperthermia experiments: Comparison between maghemite, copper, zinc, nickel and cobalt ferrite nanoparticles of similar sizes. Aip Advances, 2012. **2**(3): p. 032120.

29. Qu, M., et al., Magneto-photo-acoustic imaging. Biomedical optics express, 2011. **2**(2): p. 385-396.

30. Urries, I., et al., Magneto-plasmonic nanoparticles as theranostic platforms for magnetic resonance imaging, drug delivery and NIR hyperthermia applications. Nanoscale,2014. **6**(15): p. 9230-9240.

31. Qu, M., et al., Combined photoacoustic and magneto-acoustic imaging. Conf Proc IEEE Eng Med Biol Soc, 2009. **2009**: p. 4763-6.

32. Qu, M., et al., Contrast-enhanced magneto-photo-acoustic imaging in vivo using dual-contrast nanoparticles. Photoacoustics, 2014. **2**(2): p. 55-62.

33. Mehrmohammadi, M., et al. Combined photothermal therapy and magneto-motive ultrasound imaging using multifunctional nanoparticles. In Nanoscale Imaging, Sensing, and Actuation for Biomedical Applications VII. 2010. International Society for Optics and Photonics. 7574: p. 20-27

34. Qu, M., M. Mehrmohammadi, and S.J.S. Emelianov, Detection of nanoparticle endocytosis using magneto-photoacoustic imaging. Small, 2011. **7**(20): p. 2858-2862.

35. Morasso, C., et al., Control of size and aspect ratio in hydroquinone-based synthesis of gold nanorods. Journal of Nanoparticle Research, 2015. 17(8): p. 1-7.

36. Arsalani, S., et al., Magnetic separation of iron oxide nanoparticles to improve their application for magnetic particle imaging. Physics in Medicine & Biology, 2021. **66**(1): p. 015002.

37. Leong, S.S., Z. Ahmad, and J.J.S.M. Lim, Magnetophoresis of superparamagnetic nanoparticles at low field gradient: hydrodynamic effect. 2015. **11**(35): p. 6968-6980.

38. Andreu, J., et al., Simple analytical model for the magnetophoretic separation of superparamagnetic dispersions in a uniform magnetic gradient. 2011. **84**(2): p. 021402.

39. Leong, S.S., et al.,Working principle and application of magnetic separation for biomedical diagnostic at high-and low-field gradients. Interface focus, 2016. **6**(6): p. 20160048.

40. De Las Cuevas., et al., Low-gradient magnetophoresis through field-induced reversible aggregation. The Journal of Physical Chemistry c,2008. **112**(4): p. 945-950.

41. Lim, J., et al., Magnetophoresis of nanoparticles. Acs Nano, 2011. **5**(1): p. 217-226.

42. Leong, S.S., et al., Unified view of magnetic nanoparticle separation under magnetophoresis. Langmuir, 2020. **36**(28): p. 8033-8055.

43. Pavan, T.Z., et al., Nonlinear elastic behavior of phantom materials for elastography. Phys Med Biol, 2010. 55(9): p. 2679-92.

44. Mazon, E., et al. A pulsed magnetomotive ultrasound imaging system for magnetic nanoparticle detection. in 2021 IEEE UFFC Latin America Ultrasonics Symposium (LAUS). IEEE, 2021: pp. 1–4.

45. Sampaio, D.R.T., et al., A magneto-motive ultrasound platform designed for pre-clinical and clinical applications. Research on Biomedical Engineering, 2017. 32: p. 337-346.

46. Uliana, J.H., et al., Multiangle long-axis lateral illumination photoacoustic imaging using linear array transducer. 2020. **20**(14): p. 4052.

47. Hadadian, Y., et al., A versatile induction heating system for magnetic hyperthermia studies under different experimental conditions. Review of Scientific Instruments, 2019. **90**(7): p. 074701.

48. Patil, R., et al., In vitro hyperthermia with improved colloidal stability and enhanced SAR of magnetic core/shell nanostructures. Materials Science and Engineering,2016. 59: p. 702-709.

49. Hadadian, Y., A.P. Ramos, and T.Z.J.S.R. Pavan, Role of zinc substitution in magnetic hyperthermia properties of magnetite nanoparticles: Interplay between intrinsic properties and dipolar interactions. Scientific Reports, 2019. **9**(1): p. 1-14.

50. Hadadian, Y., et al., A novel theranostic platform: Integration of magnetomotive and thermal ultrasound imaging with magnetic hyperthermia. IEEE Transactions on Biomedical Engineering, 2020. **68**(1): p. 68-77.

51. Mazon, E., et al., A high-resolution frequency variable experimental setup for studying ferrofluids used in magnetic hyperthermia. Review of Scientific Instruments, 2017. 88(8): p. 084705.

52. Kumbhar AS, Kinnan MK, Chumanov G. Multipole plasmon resonances of submicron silver particles. Journal of the American Chemical Society. 2005. 127(36): p. 12444-5.

53. Guidelli EJ, Araujo LF, Assuncao AC, Carvalho IC, Clarke DR, Baffa O. Microwave-Assisted Growth of Silver Nanoparticle Films with Tunable Plasmon Properties and Asymmetrical Particle Geometry for Applications as Radiation Sensors. Plasmonics. 2020. 15(6): p. 1551-64.

54. Amendola V, Bakr OM, Stellacci F. A study of the surface plasmon resonance of silver nanoparticles by the discrete dipole approximation method: effect of shape, size, structure, and assembly. Plasmonics. 2010. 5(1): p. 85-97.

55. Truby, R.L., S.Y. Emelianov, and K.A.J.L. Homan, Ligand-mediated self-assembly of hybrid plasmonic and superparamagnetic nanostructures. Langmuir,2013. **29**(8): p. 2465-2470.

56. Bakuzis, A.F., et al., Chain formation and aging process in biocompatible polydisperse ferro-fluids: Experimental investigation and Monte Carlo simulations. Advances in colloid and interface science, 2013. **191**: p. 1-21.

57. Shaw, D.J., Introduction to colloid and surface chemistry. 1980: Butterworths.

58. Chen ZP., et al., Stability of hydrophilic magnetic nanoparticles under biologically relevant conditions. Journal of nanoscience and nanotechnology. 2008. 8(12): p. 6260-5.

59. Wan, J., et al., Surface chemistry but not aspect ratio mediates the biological toxicity of gold nanorods in vitro and in vivo. Scientific reports,2015. **5**(1): p. 1-16.

60. Cao, Q., et al., Hydrogen-bonding-induced colorimetric detection of melamine by nonaggregation-based Au-NPs as a probe. Biosensors and Bioelectronics, 2010. **25**(12): p. 2680-2685.

61. Wittmann, L., C. Turrina, and S.P.J.M. Schwaminger, The Effect of pH and Viscosity on Magnetophoretic Separation of Iron Oxide Nanoparticles. Magnetochemistry, 2021. **7**(6): p. 80.

62. Mehrmohammadi, M., et al., Enhanced pulsed magneto-motive ultrasound imaging using superparamagnetic nanoclusters. Nanotechnology, 2010. **22**(4): p. 045502.

63. Yoon, K.Y., et al., Synthesis of Iron Oxide Nanoclusters with Enhanced Magnetization and Their Applications in Pulsed Magneto-Motive Ultraso*und Imagin*g. Nano, 2015. **10**(05): p. 1550073.

3.A. Supplementary Materials

The MnF_2O_4 was synthesized via co-precipitation method by mixing $MnCl_2.4H_2O$ and $FeCl_4.6H_2O$ in 1:2 molar ratios, and adding to basic solutions (CH_3NH_2), then heating to form $MnFe_2O_4$. Following that, sodium citrate was added to the synthesized MNPs at 80 °C and stirred for a while to allow the surfactant to act. A detailed description of the synthesis of these MNPs can be found in Zufelato et al. [1]. The morphology and size distribution of Ci-$MnFe_2O_4$ were determined by TEM. The TEM images of manganese ferrite capped with sodium citrate showed spherical morphology (Figure 3S1a, b) with mean particle diameters of 16.7 ± 4.8 nm (Figure 3S1c) and PDI of 0.32.

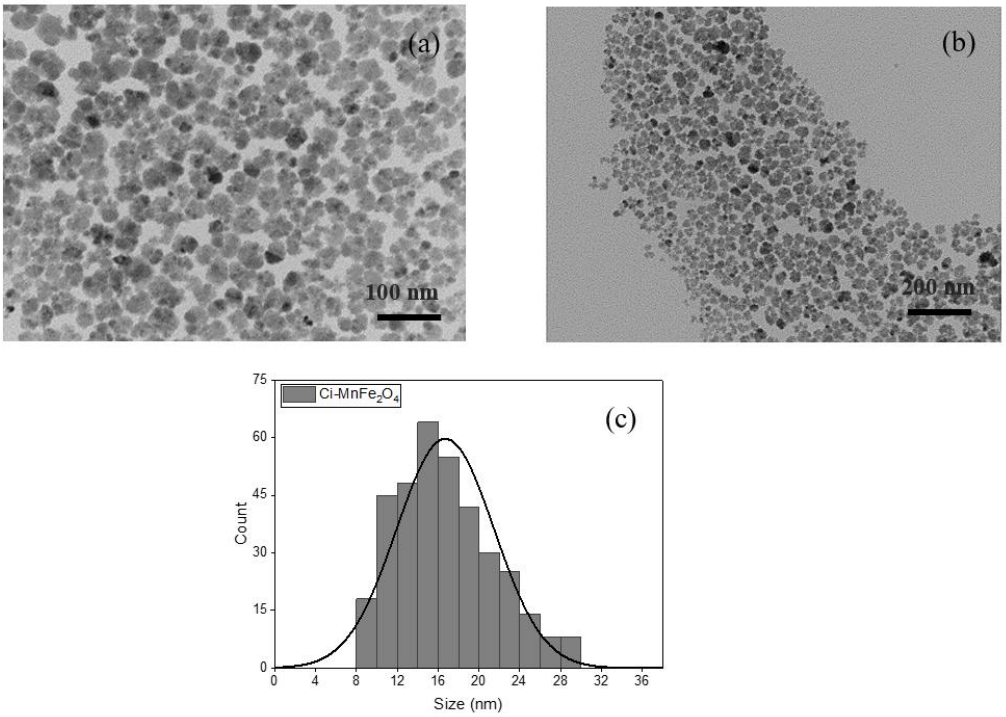

Figure 3S1. TEM images (the scale bars are 100 nm (a) and 200 nm (b) and histograms of the particle size distribution of Ci-$MnFe_2O_4$ (c).

Figure 3S2. provides information about the composition and size of Ci-$MnFe_2O_4$ by an XRD measurement. The data confirmed the spinal structure of ferrite and reported the average

crystallite size of 14 nm using the Scherrer equation. The estimated crystallite size is in good agreement with TEM results, indicating that each particle consists of a crystallite.

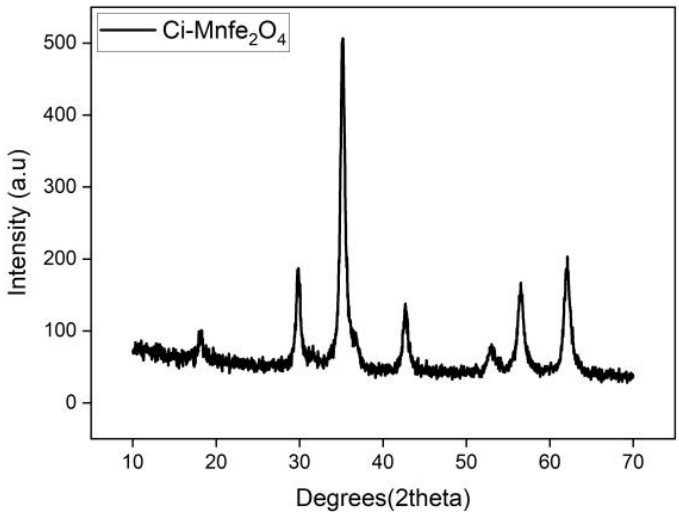

Figure 3S2. The XRD patterns of Ci-$MnFe_2O_4$.

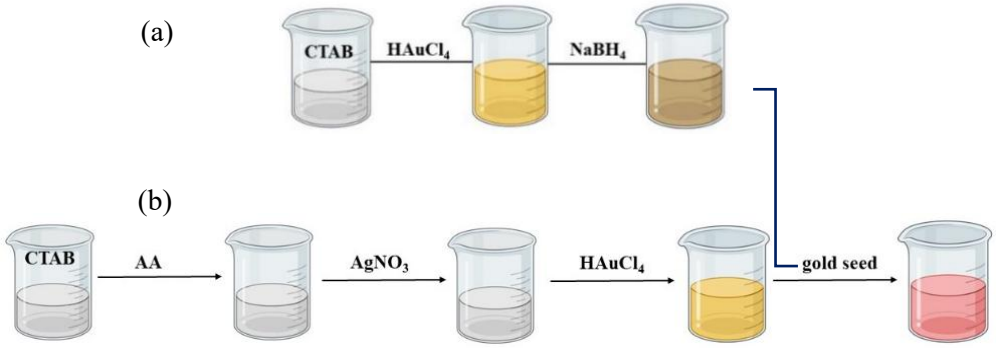

Figure 3S3. Schematic preparation of gold seed (a) and GNRs (b).

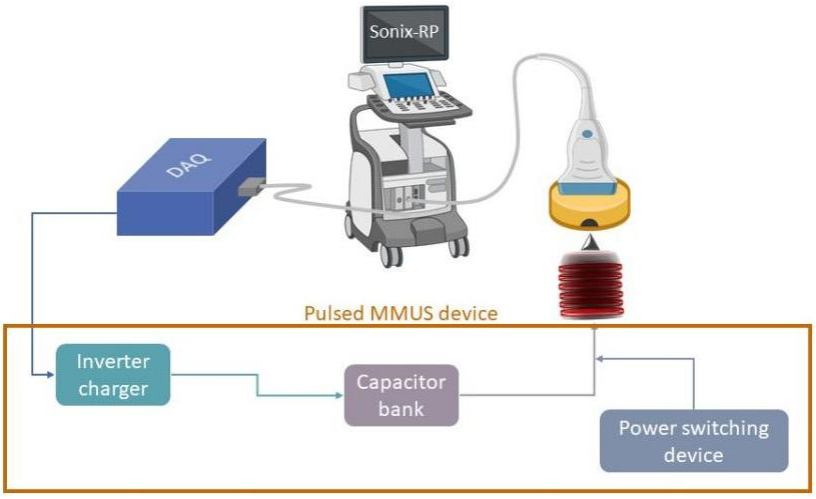

Figure 3S4. A Depiction of a pulsed magneto-motive ultrasound imaging system, which is mainly composed of an ultrasound acquisition setup integrated with a power pulse amplifier that drives the coil to generate the magnetic field excitation.

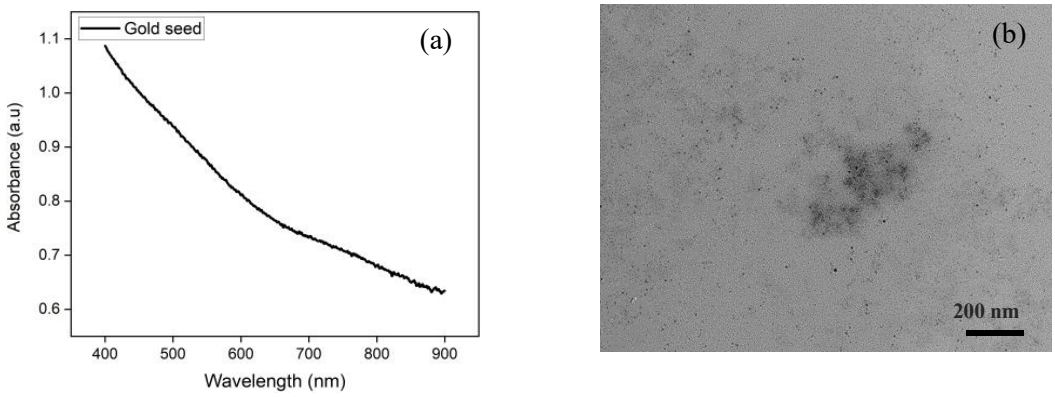

Figure 3S5. The UV-Visible spectrum of the gold seed after 20 minutes (a) and its TEM image (b) confirming the formation of small gold seeds.

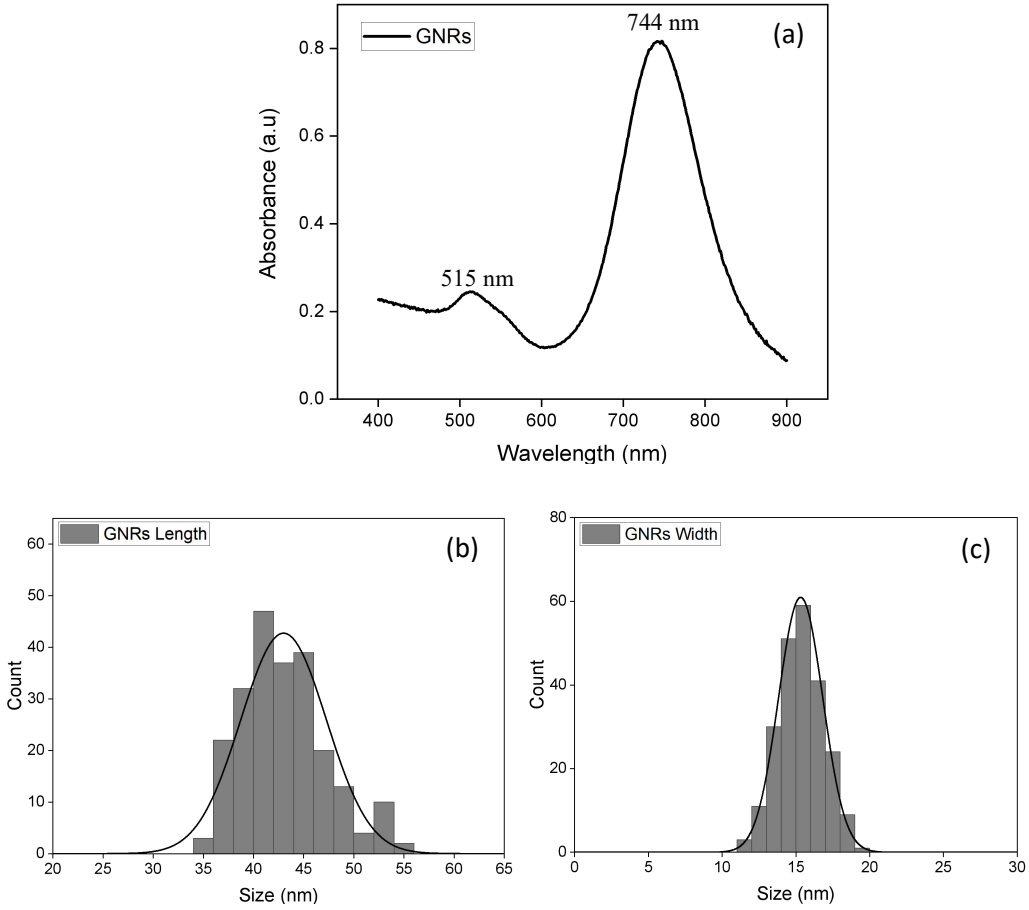

Figure 3S6. The UV-Visible absorption spectrum of GNRs (a). The histogram of long-axis (length) (b) and short-axis (width) (c) of GNRs with an aspect ratio of 2.76.

Reference

1. Zufelato, N., et al., Heat Generation in Magnetic Hyperthermia by Manganese Ferrite-Based Nanoparticles Arises from Néel Collective Magnetic Relaxation. ACS Applied Nano Materials, 2022. **5**(5): p. 7521-7539.

Chapter 4. Preliminary investigation and partial results

This chapter focused on the synthesis and characterization of IONPs using two different methods as well as GNRs coated by silica.

A. The first section describes the preparation of sodium citrate coated IONPs via an optimized coprecipitation route, as well as their characterization.

B. The second section outlines the fabrication and characterization of IONPs coated with Oleic acid using a thermal decomposition method.

C. The third section of this chapter consists of the synthesis of CTAB-capped GNRs that have been further functionalized with silica to improve biocompatibility and thermal stability for future research, as well as an investigation of their physiochemical properties.

D. In the fourth section, the cytotoxicity of PEG coated MNPs (which was thoroughly discussed in Chapter 2) and their MTT assay were assessed in B16-F10 mammalian skin cancer cells.

A. Section 1

4. Introduction

The coprecipitation route is a popular method for synthesizing MNPs [1]. Although several research have been conducted to investigate the synthesis of MNPs coated with citrate via coprecipitation, the absence of aggregation and relatively narrow size distribution was rarely observed in these studies [2-4]. Here, by optimizing of coprecipitation technique, which is fully described in chapter 2 (section 2.2.1) [5] highly stable, relatively uniform, and aggregation-free citrate coated MNPs were produced.

4.1. Materials

The chemical reagents ferric chloride hexahydrate ($FeCl_3 \cdot 6H_2O$) and ferrous chloride tetrahydrate ($FeCl_2 \cdot 4H_2O$) were purchased from Sigma Aldrich. Ammonium hydroxide (NH_4OH; 27%), hydrochloric acid (HCl; 37%) were purchased from Synth. Sodium citrate was purchased from dynamic.

4.2. Methods

4.2.1. Preparation of MNPs

Briefly, to make magnetite NPs, an aqueous solution containing ferric and ferrous salts in a molar ratio of 2:1 was mixed with a base (ammonium hydroxide) at an elevated temperature of 80 °C, under mechanical stirring rate of 750 rpm [5] . After 5 minutes of reaction, 0.07 g of sodium citrate (acting as a capping agent to improve stability and avoid oxidation) was added to the mixture and stirred for another 20 minutes and heated at elevated temperature to allow the coating process to act. Following that, the reaction medium was then transferred to a beaker and placed in an ultrasonic bath for 30 minutes to prevent aggregation. Next, these MNPs were precipitated with a strong permanent magnet and rinsed several times until the colloidal dispersion reached a neutral pH. Finally, to perform characterizations, a portion of the sample was dried in an oven at 32 °C under vacuum overnight.

4.3. Characterization of IONPs

The prepared IONPs coated by citrate or OA were characterized by different methods. The morphology and core size of the MNPs were investigated through TEM using a JEOL-JEM-100 CXII unit with an accelerating voltage of 100 kV, by drying a drop of the washed colloidal dispersion onto a copper grid covered with a conductive polymer. The TEM size of particles was measured using ImageJ software The hydrodynamic diameter and PDI of the NPs suspension was determined by dynamic light scattering (DLS) using a Zetasizer Nano ZS (Malvern-UK). The data was collected at a fixed angle of 173° and a wavelength of 633 nm (He–Ne laser). The crystalline properties and phase identification were acquired by a XRD (D5005 Diffractometer, Bruker) analysis using X-ray beam nickel-filtered Cu-K radiation (λ=1.5406 Å) in the range of $10°<2\theta°<70°$. In addition, thermal analyses (TGA/DSC) of the samples in powder form were measured from 25 to 800 °C under a N2 atmosphere ramp of 10 °C/min using TGA/DTA/DSC Equipment (Model SDTQ600-TA Instruments). Furthermore, the magnetic properties of the MNPs were measured by a vibrating sample magnetometer (VSM) and magnetic particle measurements system (MPMS). In addition, the magnetophoretic behavior of samples, movement of MNP in an inhomogeneous magnetic field, was examined using a magnetic separation system (SEPMAG, Barcelona, Spain) with a magnetic field gradient of 15 T/m. The measurements were taken at room temperature (25 °C) and under different applied magnetic fields from −10 kOe to +10kOe, on powder samples.

4.4. Results

4.4.1. TEM Analysis

Figure 4.1 presents the TEM images and size distribution of citrate coated MNPs. As shown, the mean diameter of MNPs was 22.12 ± 3.3 nm, with spherical morphology and a relatively narrow size distribution.

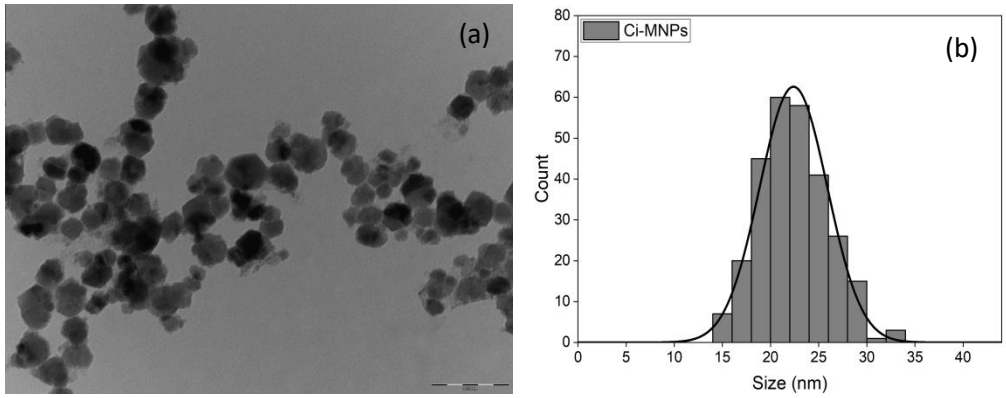

Figure 4.1. (a) TEM images in the scale bars of 100 nm, and (b) size distribution of citrate coated MNPs.

4.4.2. XRD Analysis

The crystal structure and size of Ci-MNPs were examined using XRD, Figure 4.2. The diffraction peaks at 2θ (30.1, 35.5, 43.1, 57.0, and 62.6°) corresponding to the (220), (311), (400), (511), and (440) of the magnetite crystal structure, respectively [95]. The average crystallite size of Ci-MNPs was obtained considering the broadening of XRD peak (3 1 1) using the Scherrer equation (equation 4.1):

$$D=k\lambda/\beta\cos\theta \qquad (4.1)$$

Where *K* is a numerical factor known as the crystallite shape factor and can be considered 0.94 for spherical nanoparticles with a cubic crystal structure, λ is the wavelength of the radiation (0.15406 nm), β is full width at half-maximum of the peak intensity (FWHM), and θ is peak position (Bragg angle) [96]. The XRD patterns of citrate coated MNPs revealed a highly crystalline cubic spinel structure. The reflection peak positions and relative intensities of Ci-MNPs are well matched with XRD patterns of magnetite in the reported literature. This result indicates the formation of a pure magnetite NPs phase [6,7], Figure 4.2. The estimated crystallite sizes of IONPs coated by citrate was 19 nm. The crystal size is almost like the particle sizes of TEM images, indicating that each particle is composed of a single crystal.

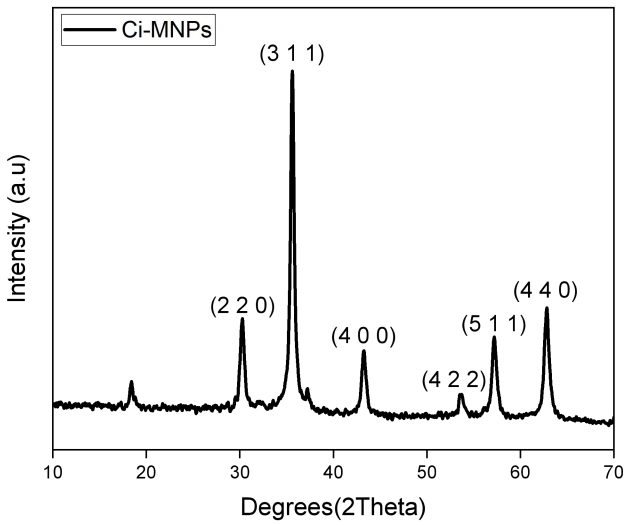

Figure 4.2. XRD patters of citrate coated MNPs.

4.4.3. DLS and Zeta potential Analysis

DLS measurements were carried out to obtain the hydrodynamic size of the magnetic NPs, which provide information about the core size of the NPs and their surrounding layer (core + shell). The particle size for citrate capped MNPs was 45 nm and PDI of 0.29, Figure 4.3.

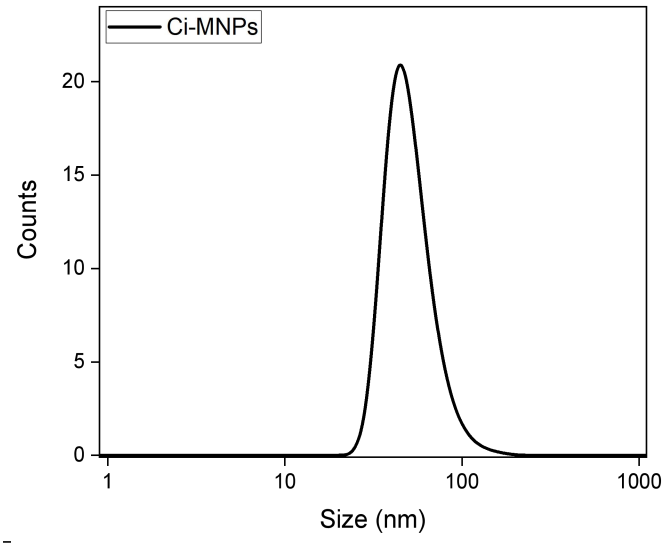

Figure 4.3. The hydrodynamic diameter of the citrate coated MNPs by DLS measurement.

Another important parameter to estimate is the zeta potential of NPs, which measures the colloidal stability of MNPs. The MNPs coated with sodium citrate demonstrated high stability, with a Zeta potential of -30 mV, Figure 4.4. This negative value of Zeta is due to the adsorbed carboxylate groups derived from citrate in distilled water [8,9].

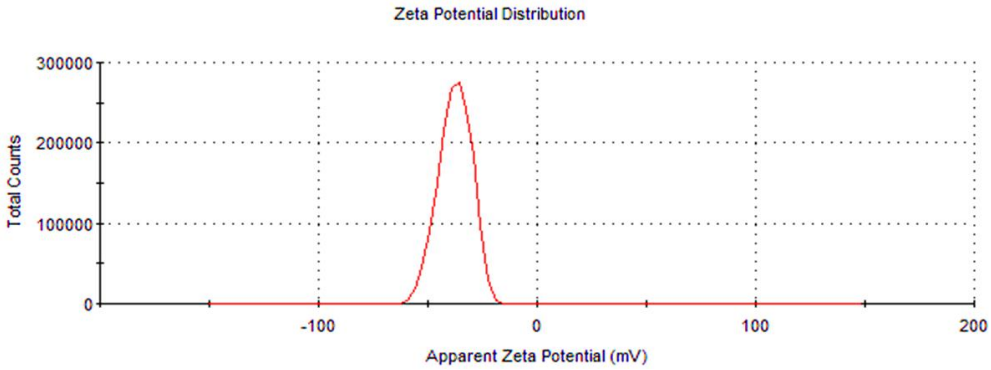

Figure 4.4. Zeta potential of citrate coated MNPs.

4.4.4. Magnetophoresis Anaylsis

The separation time of the MNPs was measured using a magnetic separation system, which is highly dependent on particle size distribution. The magnetophoretic behavior of the sample is illustrated in Figure 4.5. To perform the magnetophoretic process, 0.2 wt% of this sample dispersed in water and the changes in suspension opacity were observed over time. Due to high stability of the MNPs and the absence of large particle size, a relatively long separation time of t_{50}= 88.6 s was observed [5].

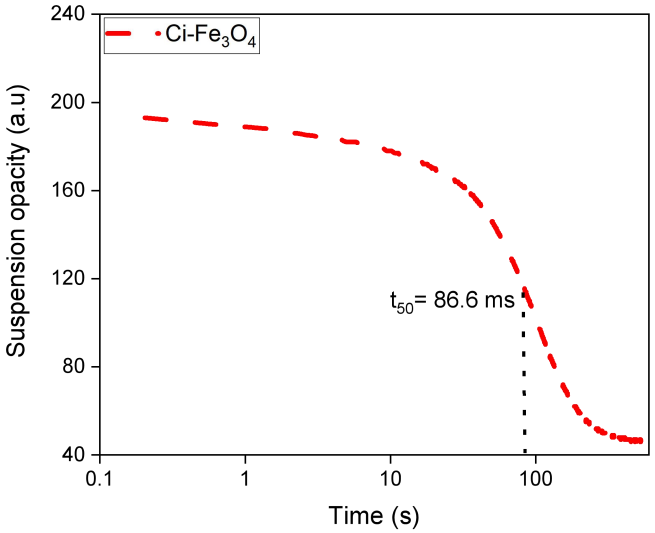

Figure 4.5. Magnetophoresis experiments for one citrate coated MNPs with 0.2 wt.%.

4.4.5. Magnetic property Analysis

Magnetization measurements of Ci-MNPs in the applied field of − 10 to +10 kOe at room temperature, is reported in Figure 4.6. This sample presents superparamagnetic behavior at room temperature without any remanence or coercivity. The magnetization for this sample was 57 emu/g at 10 kOe. The reported magnetization values for MNPs coated with citrate are relatively higher than in previous studies [4,9].

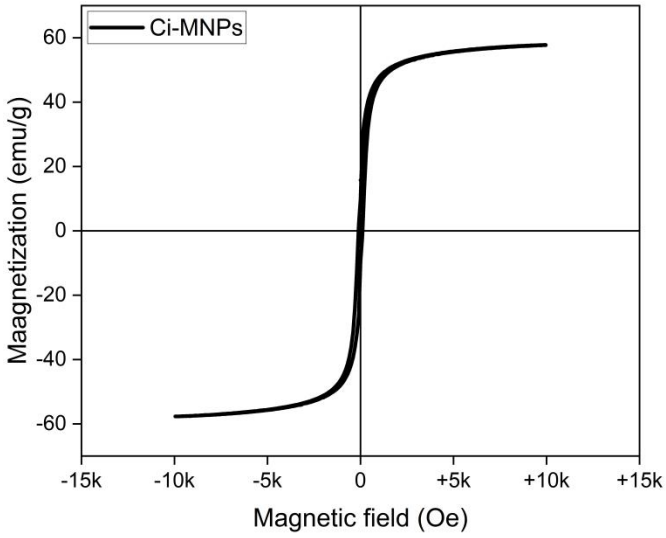

Figure 4.6. Magnetization curve for Ci-MNPs in the applied field of −10 to +10 kOe, MNPs in the applied field of − 10 to +10 kOe at room temperature considering the total mass of MNPs.

4.4.6. MMUS experiment

MNPs have been used in a variety of biomedical applications due to their excellent magnetic properties. MMUS, a novel molecular imaging technique, benefits from the use of MNPs as a contrast agent. This modality is discussed in detail in the first and second chapters [10,11]. To perform this experiment gelatin tissue mimicking phantoms were labeled with 0.3 wt% Ci-MNPs. The displacement map of the sample obtained by MMUS imaging in phantoms embedded with Ci-MNPs using three different magnetic pulse widths with the same magnetic field amplitude is demonstrated in Figure 4.7. The maximum induced displacement was 7 μm ± 0.6, using a magnetic pulse width of 6 ms.

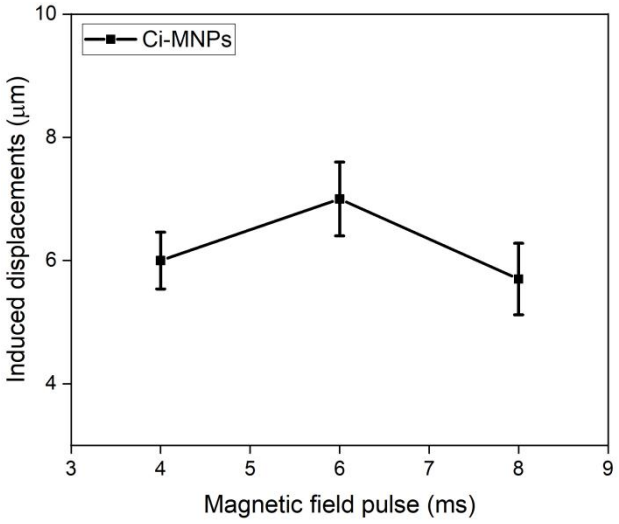

Figure 4.7. The induced vibration of a phantom labeled with Ci-MNPs, with pulse duration ranging from 4 to 8 ms.

B. Section 2

5. Introduction

Thermal decomposition (TD), as a standard method, was used to synthesize IONPs with excellent small size, well-defined shape, and high monodispersity. In TD, the separation between the nucleation and growth steps is an essential factor for producing monodisperse nanoparticles with narrow size distributions. This separation can be effectively accomplished when these two stages take place at two different temperatures [12,13,14].

5.1. Materials

The chemical reagents used in this research were ferric chloride hexahydrate ($FeCl_3$. $6(H_2O)$), and ferrous chloride tetrahydrate ($FeCl_2.4(H_2O)$), which were purchased from Sigma Aldrich. Ammonium hydroxide (NH_4OH; 27%), and hydrochloric acid (HCl; 37%) were purchased from Synth. Oleic acid ($C_{18}H_{34}O_2$; 89%), 1-Octadecene (technical grade; 90%) and sodium oleate (90%) were prepared from Synth, Aldrich and Dynamic, respectively. All the materials were used as received without any purification.

5.2. Methods

5.2.1. Preparation of IONP capped by OA

Preparation of the monodispersed IONPs covered by OA is conducted in accordance with a prior study by Park et al. [14]. This route consists of two steps as follows:

5.2.1.1. Synthesis of Iron oleate complex

The iron oleate complex was prepared by reacting non-toxic metal salts and sodium oleate. In a typical synthesis of iron–oleate complex, 3.06 g of iron (III) chloride and 10.34 g of sodium oleate was dissolved in a mixture solvent composed of 22 ml ethanol, 17 ml distilled water and 40 ml hexane. The resulting solution was heated to 70 ˚C and kept at that temperature for four hours [99]. When the reaction was completed, the upper organic layer containing the

iron–oleate complex was washed five times with 50 ml distilled water in a separatory funnel. After washing and removing water, again the solution was heated to 70 ˚C and kept at that temperature for four hours to evaporate hexane and water. Then we have iron–oleate complex in a waxy solid form [15,16].

5.2.1.2. Synthesis of Iron oxide nanoparticles

To synthesize small and monodispersed IONPs (around 10 nm), 5 g of the iron oleate complex synthesized was dissolved in 88.5 μL of oleic acid and 35.64 mL 1-octadecene at room temperature. The reaction mixture was gradually heated to 320 ˚C with a constant heating rate of 3.3 ˚C/min, and then maintained at that temperature for 30 min. When the reaction temperature reached 320 ˚C, a severe reaction occurred, and the initial transparent solution became turbid and brownish black [13,14,16]. The resulting solution containing the nanocrystals was then cooled under ambient condition, and 30 ml of ethanol was added to the solution to precipitate the nanocrystals. The nanocrystals were separated by a strong magnet and washed several times with hexane and ethanol.

5.3. Results

5.3.1. Size and morphology of IONPs coated by OA

TEM images and histograms of the size distributions of monodisperse IONPs coated by OA are depicted in Figure 4.8 (a-c). This monodispersed MNPs exhibited excellent uniform spherical particles, and narrow size distribution with a mean size of 9.50 nm ± 1.13 [14,17-18].

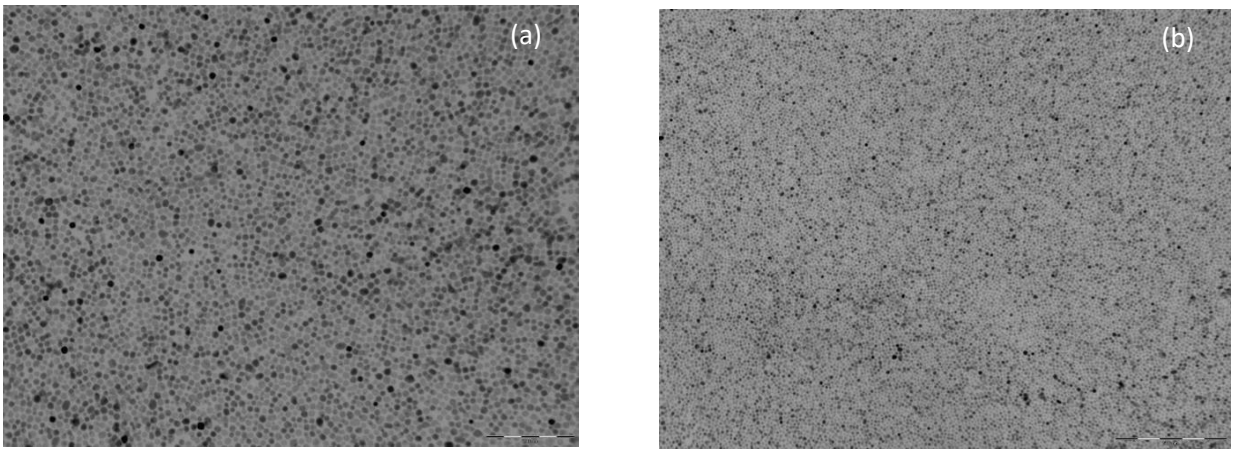

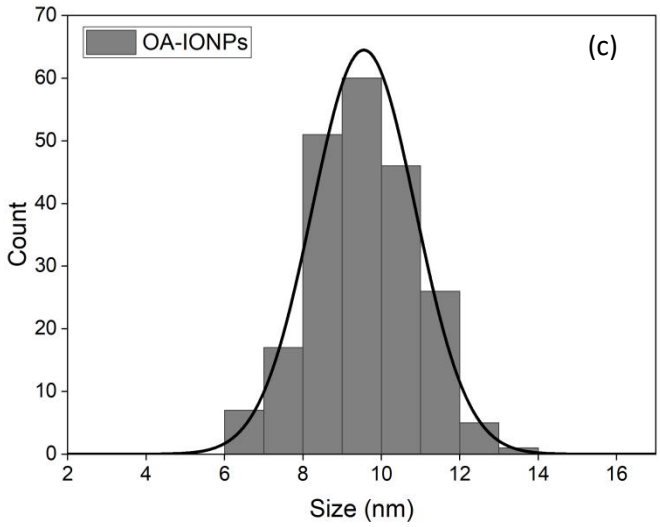

Figure 4.8. (a, b) TEM images in the scale bars of 200 and 500 nm and (c) histograms of the size distribution of OA-IONPs.

Figure 4.9 depicts the hydrodynamic size and PDI of the OA-IONPs using DLS analysis. The sample had a hydrodynamic size and PDI of 16 nm and 0.12, respectively. As it was expected, because of the presence of OA (acting as a capping agent) a slightly larger hydrodynamic size was observed compared to size by TEM results. The reason for this is that DLS measures core size plus shell (organic layer (e.g., OA)), resulting in larger particle size, whereas TEM only measures core size of NPs [5,19].

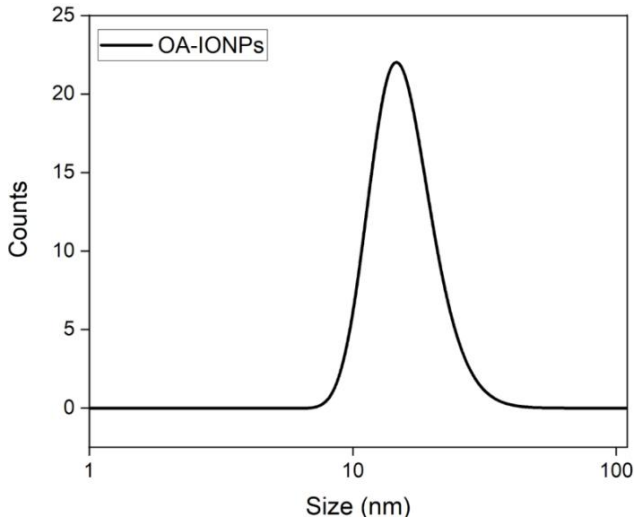

Figure 4.9. The hydrodynamic diameter of the OA-IONPs by DLS measurement.

5.3.2. Thermogravimetric Analysis

The weight loss observed during TGA provides confirmation of the presence of OA and its amount absorbed on the surface of the MNPs. TGA analyses were recorded on the powder sample. TGA of the obtained OA-IONPs revealed a typical IONP-coated OA curve, which was similar to the previous studies [18, 20]. The first derivative (DTGA) of the TGA data was also plotted, Figure 4.10. Based on the DTGA there are two weight losses (in 263 ℃ and 428 ℃) in this sample, which are corresponding to the desorption and decomposition of the OA bonded on the surface of the MNPs. At these ranges, the weight loss was 20 %.

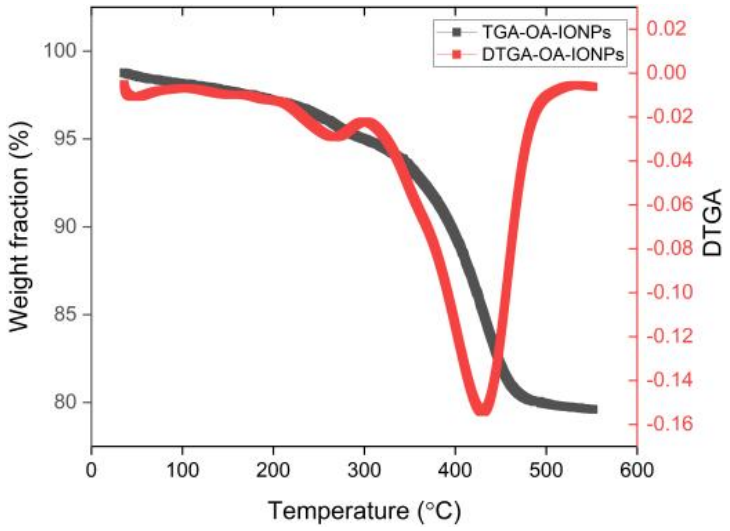

Figure 4.10. The TGA and DTGA of OA-coated IONPs.

5.3.3. Magnetization of OA-IONPs

Magnetization measurements of OA-IONPs in the applied field of − 50 to +50 kOe at room temperature, is reported in Figure 4.11. This sample demonstrated no remanence or coercivity within our experimental setup, confirming their superparamagnetic state. The saturation magnetization of OA-IONPs was reported to be 80 emu/g after subtracting the mass of organic compound (OA) analyzed with TGA. The reported value is nearly identical to the bulk material and represents a large saturation magnetization for a single magnetite NPs [18].

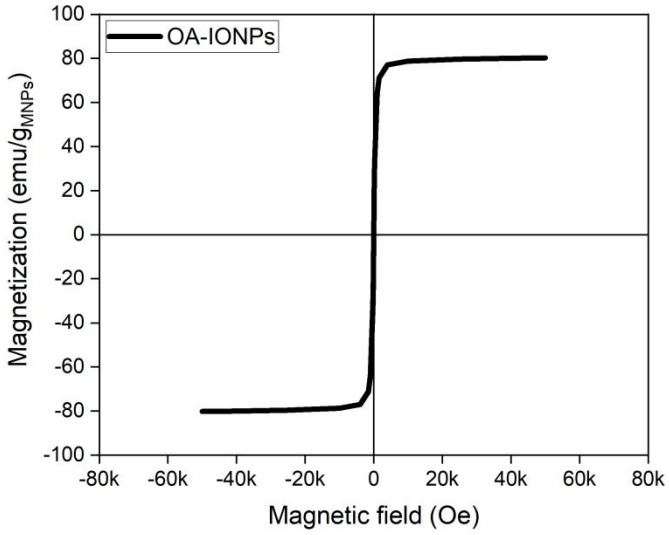

Figure 4.11. Magnetization curve of OA-coated IONPs at room temperature.

C. Section 3

6. Introduction

Gold nanorods are widely regarded as the most intriguing plasmonic NPs owing to their interesting properties. Several studies have been synthesized CTAB coated GNRs in which CTAB acts as a surfactant to increase stability and shape-inducing agent [21,22] ; however, CTAB disrupts membrane integrity and causes cytotoxicity [22] , limiting its use in biomedical applications such as PA, photothermal therapy (PTT), and drug delivery. Another disadvantage of CTAB-GNRs during PA or PTT is that the NPs lose their stability and reshape into spherical nanoparticles when exposed to radiation. Thus, silica coating has been widely recommended as a promising overcoating for GNRs due to its numerous merits, including biocompatibility, enhanced thermal stability, and silica shell that can be mesopores and employed for drug loading [23-25].

6.1. Materials

The chemical reagents used were: cetyltrimethylammonium bromide (CTAB), sodium borohydride ($NaBH_4$), tetrachloroauric acid ($HAuCl_4.4H_2O$), silver nitrate ($AgNO_3$), and L-ascorbic acid (AA), which were purchased from Sigma, Aldrich, Vetec, and Panreac, respectively. Tetraethylorthosilicate (≥99.0%; TEOS), Sodium oleate (≥97.0%; NaOL) and methanol (99.8%; CH_3OH) were purchased from Aldrich, dynamic and Panreac, respectively. Milli-Q® system ultrapure water (18.2 MΩ cm) was used throughout the experiments.

6.2. Methods

6.2.1. Preparation of GNRs

GNRs were prepared according to the research of Ye et al. and Pellas et al [26,27] . To elaborate, a seed-mediated growth method was employed to produce GNRs with a monodisperse and uniform shape. Briefly, the seed solution was made by mixing 5 mL of 0.2 M CTAB

aqueous solutions and 5 mL of 0.50 mM $HAuCl_4 \cdot 3H_2O$. Then, freshly prepared ice-cold $NaBH_4$ solution (0.01 M, 0.6 mL) was added into a mixture of CTAB and $HAuCl_4 \cdot 3H_2O$ under vigorous stirring (1000 rpm) for 2 min to form a brown gold seeds solution and it kept for 30 min at 30 °C before use. The next step which is the growth solution was carried out by dissolving 9 g of CTAB and 1.234 g of NaOL in 250 mL of water at 50 °C. This solution was allowed to cool down to 30 °C, and then, $AgNO_3$ solution (4 mM, 18 mL) was added, and the resulting solution was kept without stirring for 15 minutes. Then, $HAuCl_4 \cdot 3H_2O$ (1mM, 250 mL) aqueous solution was injected into the above solution and allowed to react for 90 min at 700 rpm. Next, 1.5 mL of HCl (37 wt %) was added to adjust the pH to 1.5. After another 15 minutes of slow stirring, AA aqueous solution (64 mM, 1.25 mL) was added, and it was slowly stirred for 30 s. Finally, 50 µL of the seed suspension was injected into the growth solution for 30 s to begin the growth. The resulting suspension was left undisturbed at 30 °C for 12 hours to allow GNRs to grow [27]. The following day, the final product was centrifuged (5600 rcf, 20 minutes) to remove the excess reactants. Lastly, GNRs were diluted in pure water to 20 mL and stored at 30 °C.

6.2.1.1. Silica Shell Growth on GNRs

The prepared GNRs are coated with a silica shell. To do so, several milliliters of synthesized GNRs were centrifuged (5600 rcf; 15 min) and then diluted to a final volume of 5 mL of water and 1mM CTAB concentration. The pH was then adjusted to 4 by adding small amounts of 0.1 M NaOH. Thereafter, 124 µL of TEOS in 20% MeOH was added to 5 mL of an aqueous suspension of GNRs while vigorously stirring. Then, the pH was raised to 8 by adding 0.1 M NaOH, and the solution was stirred for 20 minutes at 600 rpm and then kept for 20 h at room temperature.

6.2.1.2. Purification

The next day, the solution containing GNRs coated by silica centrifuged (7060 rcf, 15 min). The supernatant was removed, and the pellet was redispersed several times with methanol and water. After the last washing, the core-shell nanostructures were dispersed in 5 mL of water.

6.3. Characterization of GNRs after and before silica coating

Different characterizations of GNRs with and without silica shell were carried out. UV spectrometer (Ultrospec 2100 pro) with a resolution of 0.5 nm operating in the wavelength range of 200-900 nm was used to determine the optical properties that provide information about the size of the GNR through the plasmonic bands. In addition, as mentioned in section 4.3, other characterizations such as TEM, XRD, and Zeta potential were conducted for this NPs.

6.4. Results

6.4.1. UV Visible Analysis

A typical UV-Vis spectrum of GNRs after and before silica coating is shown in Figure 4.12. For GNRs without a silica shell, the UV-Vis spectrum depicts transverse and longitudinal plasmon bands at 525 and 784 nm, respectively. While the longitudinal resonance shifts by 18 nm after overcoating by silica, as expected, this red shift can be due to the effect of silica shell, which agrees with other studies [24, 27-28].

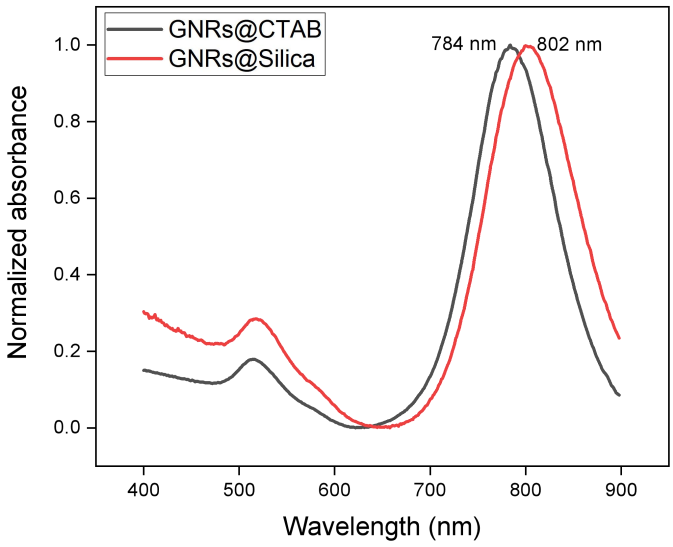

Figure 4.12. Absorption spectra of CTAB-GNRs and GNRs coated by silica.

6.4.2. TEM analysis

Figure 4.13 a-c exhibited the TEM image of GNRs before coating by silica and their size distribution, respectively. Figure 4.13a illustrates excellent shape and uniform size of GNRs. The average width and length of GNRs were 29 ± 2.3, 101 ± 7 nm, respectively (Figure 4.13 a,b) [27].

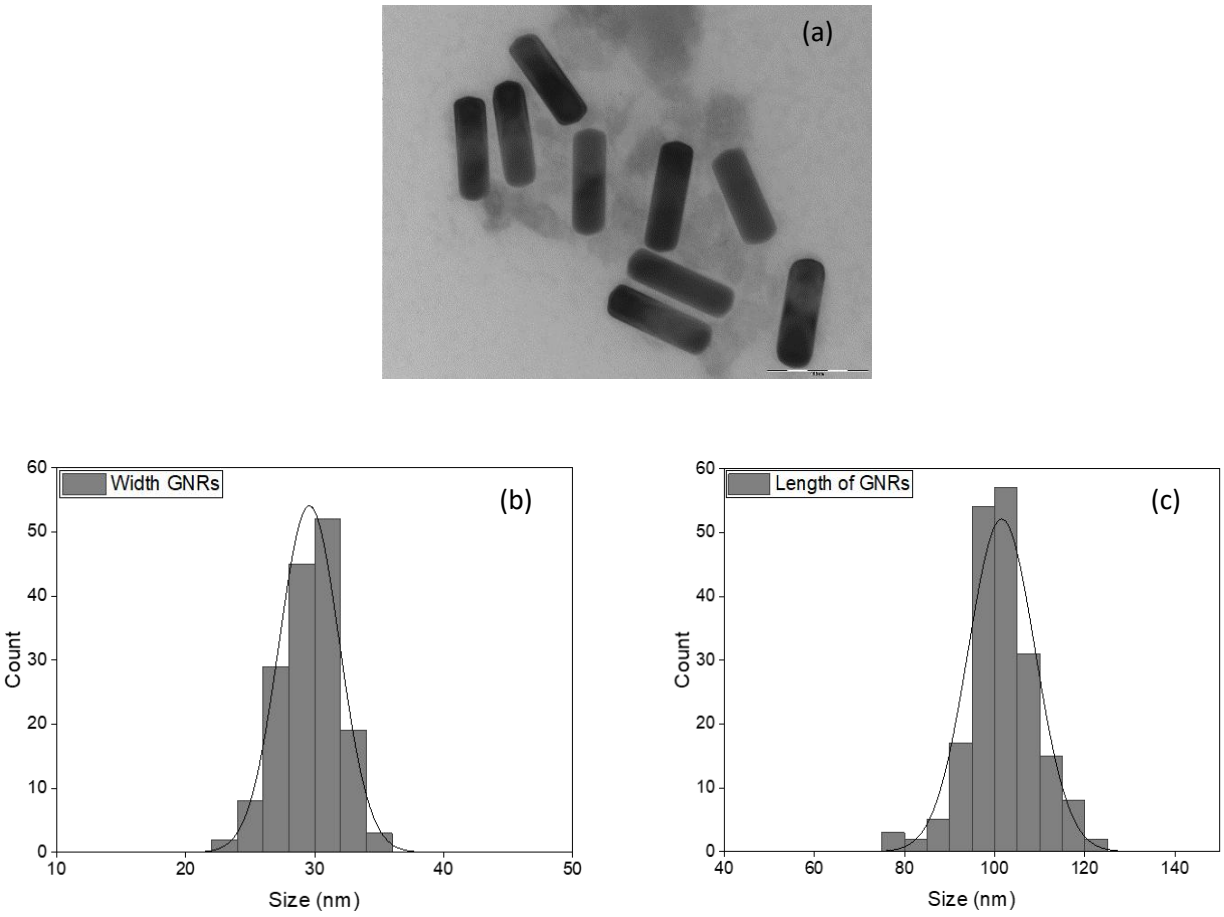

Figure 4.13. (a) TEM images of GNRs in a scale bar of 100 nm. (b and c) The histogram of long-axis (length) and short-axis (width) of GNRs, respectively with an aspect ratio of 3.48.

TEM image of GNRs after coating by silica is shown in Figure 4.14. There is excellent silica decoration around GNRs, and the thickness of the silica shell is approximately 12 ± 2.3 nm [28].

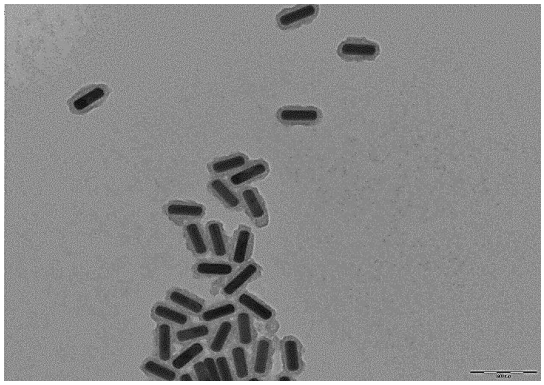

Figure 4.14. TEM images of GNRs coated by silica in a scale bar of 200 nm.

6.4.3. XRD analysis

Typical XRD pattern of GNRs prepared by the seed-mediated growth method is illustrated in Figure 4.15. Diffraction peaks at 2θ (37.91, 44.06, 64.39) corresponded to planes (111), (200), (220) were indexed to the gold metal with face centered cubic structure, according to the Figure 4.15. The lattice constant calculated from the diffraction peak (111) is a = 4.088 Å which agrees with another research [29, 30].

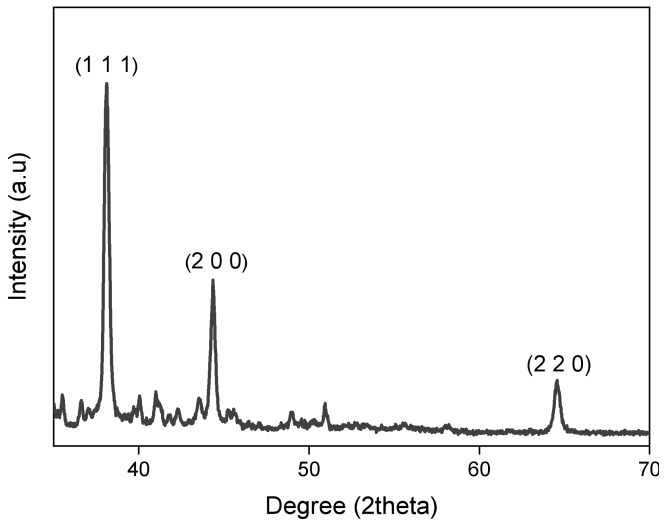

Figure 4.15. XRD patterns of CTAB-GNRs.

6.4.4. Zeta anaylsis

The silica shell was confirmed by Zeta measurements of the GNRs dispersed in water. GNRs without shell of silica (green curve (a)) had a positive surface charge of +39 mV (due to the positively charged head groups of the CTAB bilayer on the surface of GNRs) , whereas silica coated GNRs displays a negative Zeta potential of -19 mV (red curve (b))[31]. The zeta potential of GNRs with and without silica shell is shown in Figure 4.16.

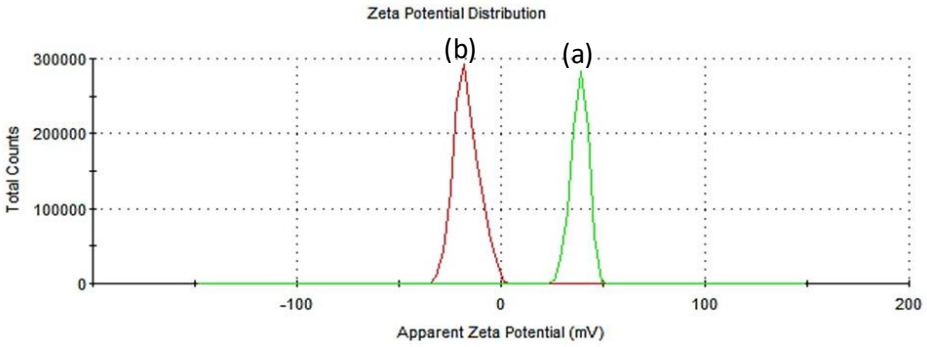

Figure 4.16. Zeta potential of GNRs before and after silica shell (a) and (b), respectively.

D. Section 4

7. Introduction

To ensure that NPs will not have harmful side effects on living organisms' toxicity measurement is required [32]. It should be noted that the cell viability responses of NPs can vary depending on their physicochemical properties such as size, shape, material composition, used dose, and cell type [22, 33-34]. Therefore, the toxicity assay for each particle must be performed prior to *in vivo* application due to the distinct biological response of each particle to the cells.

7.1. Materials

3-(4,5-Dimethylthiazol-2-yl)-2,5-diphenyltetrazolium bromide (MTT) powder, Dulbecco′s Modified Eagle′s cell culture media (DMEM) were purchased from Sigma and Gibco, respectively. B16-F10 (Melanoma) mammalian cell were purchased from the USA Cell Line Bank.

7.2. Methods

7.2.1. In vitro cytotoxicity studies (MTT assay)

The cytotoxicity of PEG coated MNPs was tested using a bacterial strain of *Escherichia Coli* Rosetta (in chapter 2 [5]), and no cytotoxicity was observed even at 0.5 mg/ml. However, because bacteria and eukaryotic cells (human or murine cell lines) have different mechanisms, an *in vitro* measurement on B16-F10 mammalian cells was performed to ensure biocompatibility of PEG coated MNPs. The MTT colorimetric assay was used to investigate the viability of PEG-MNPs. For the biological studies, the DMEM cell culture media was supplemented with 1 wt% antibiotic-penicillin/streptomycin (Cultilab), 10 wt% fetal bovine serum (sterile FBS-Gibco) in a humidified 37 °C incubator. B16-F10 melanoma cells line were seeded (2×10^4) into 24-well plates for 24 hours [31] and then PEG-MNPs nanoparticles with concentrations of 1, 5, 10, 20, 100 μg/ml was added. In addition, as a control, a set of wells comprised only cells in DMEM medium, without the MNPs. Finally, a microplate reader (MULTISKAN GO) was used to

measure the cell viability assay with MTT at wavelengths of 570 and 690 nm. To determine the percentage viability of the cells, the ratio of mean absorbance of quadruplicate readings of sample wells (containing PEG-MNPs) to the absorbance of control wells is multiplied by 100.

7.3. Results

Figure 4.17 depicts the MTT assay results for various concentrations used toward B16-F10 cell lines (melanoma) at three different days: 24 hours (a), 48 hours (b), and 72 hours (b). The difference in cell growth and viability of PEG-MNPs samples compared to the control was negligible, Figure 4.17. Based on the obtained results until concentration of 0.1 mg/ml can be considered safe to use *in vivo* application [35-36].

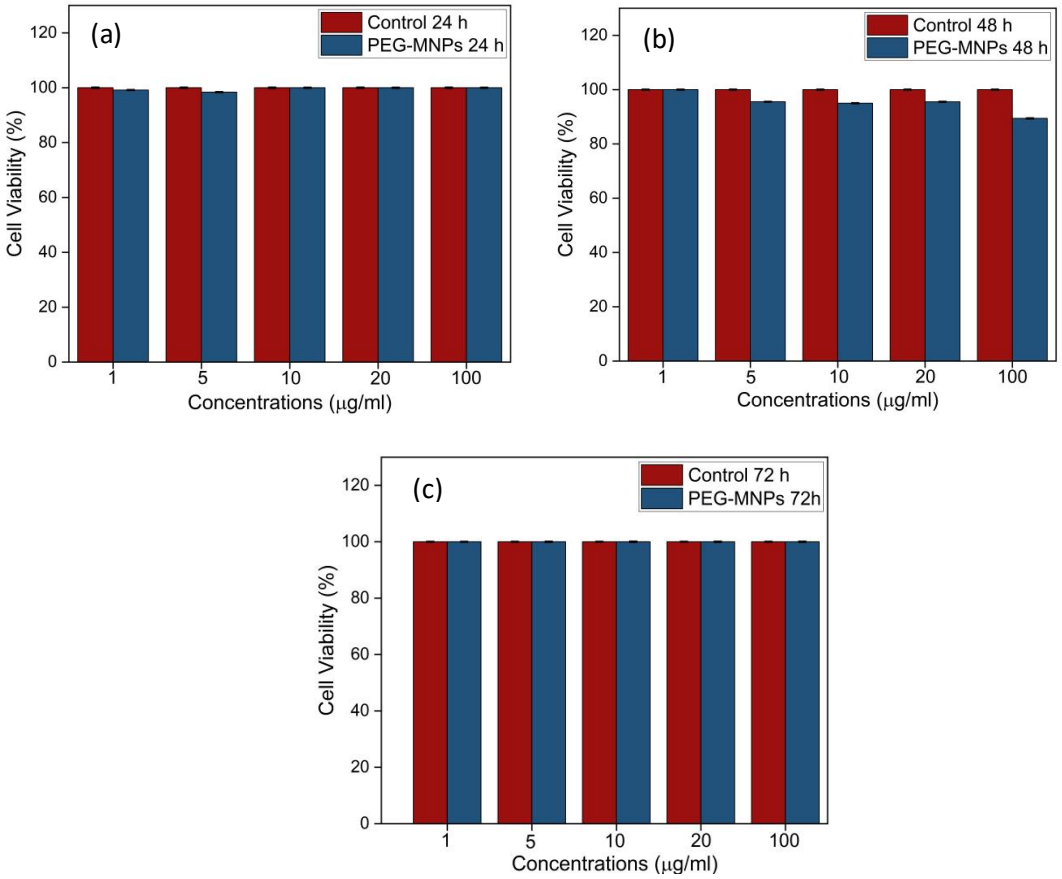

Figure 4.17. Cell viability studies of B16-F10 cells after incubating for 24h (a), 48h (b) and 72 h (b) with varying concentration.

General conclusion

The synthesis and characterization of MNPs and GNRs for biomedical applications are described in this thesis. The naked MNPs were synthesized using a convenient, reproducible, and optimized coprecipitation route, thereafter polyethylene glycol as a ligand was used in a post synthesize. At room temperature, both naked MNPs and covered with PEG demonstrated superparamagnetic behavior. Magnetic and structural characterizations of PEG-capped MNPs revealed improved magnetization whereas retaining the same cubic spinel structure as bare MNPs. Furthermore, using PEG as a ligand for MNPs increased their biocompatibility toward bacterial *E. coil* by up to 0.5 mg/ml. The benefits of PEG coated MNPs mentioned above are favored in biomedical applications. Furthermore, the naked and coated MNPs were assessed as contrast agents for magneto-motive ultrasound imaging in phantom studies and evidenced a relatively large movement with only 0.35 wt%. The potential of both samples of MNPs as heat generators in magnetic hyperthermia was also investigated, and MNPs covered with PEG demonstrated higher heating efficiency than bare MNPs. The demonstration of appropriate physical and chemical properties of the used MNPs promotes their use in diagnostic and therapeutic applications.

Moreover, a mixture of Ci-$MnFe_2O_4$ and CTAB-GNRs was suggested to act as multifunctional NPs due to their magnetic and optical properties simultaneously. Because of their opposite surface charges, this integration could result in the formation of nanoclusters while maintaining superparamagnetic properties. We observed that this combination amplified the contrast of magneto-motive ultrasound imaging in proportion to increasing GNRs concentration over using only MNPs. Meanwhile, this combination almost maintained its beneficial impact on photoacoustic imaging and hyperthermia platforms.

Finally, we did take advantage of the optimized coprecipitation route to produce highly stable sodium citrate covered MNPs with relatively high saturation magnetization and absence of aggregation. Furthermore, we used the thermal decomposition method to produce highly monodispersed MNPs with well-defined shape, size and large saturation magnetization, and the

desired results were obtained through various characterizations. In addition, due to the nature toxicity of CTAB, additional functionalization by silica was proposed here, which not only boosts thermal stability but also greatly improves biocompatibility. Meanwhile, it should be stated that an appropriate ligand exchange for small uniform MNPs coated with oleic acid will be conducted as a subsequent step to make them hydrophilic and functional in biomedical fields. Following that, by selecting appropriate aspect ratios, silica-GNRs will be mixed with hydrophilic MNPs to achieve a proper deposition of MNPs around silica-GNRs, and their potential in photoacoustic imaging, magneto-motive ultrasound imaging, and magnetic hyperthermia also will be investigated.

References

1. Arsalani S, Guidelli EJ, Araujo JFDF, Bruno AC, Baffa O. Green Synthesis and Surface Modification of Iron Oxide Nanoparticles with Enhanced Magnetization Using Natural Rubber Latex. ACS Sustain Chem Eng 2018; 6:13756–65.

2. Silva-Silva MJ, Mijangos-Ricardez OF, Vázquez-Hipólito V, Martinez-Vargas S, López-Luna J. Single and mixed adsorption of Cd(II) and Cr(VI) onto citrate-coated magnetite nanoparticles. New pub: Balaban 2014 ; 57:4008–17.

3. Bertorelli R, Botella P, Nieciecka D, R˛ Ekorajska A, Cichy D, Kó P, et al. Synthesis and Characterization of Magnetic Drug Carriers Modified with Tb3+ Ions. Nanomaterials 2022, 12, 795; 12:795.

4. Li L, Mak KY, Leung CW, Chan KY, Chan WK, Zhong W, et al. Effect of synthesis conditions on the properties of citric-acid coated iron oxide nanoparticles. Microelectron Eng 2013;110:329–34.

5. Arsalani S, Hadadian Y, Mazon EE, Guidelli EJ, Kava E, Ramos AP, et al. Uniform size PEGylated iron oxide nanoparticles as a potential theranostic agent synthesized by a simple optimized coprecipitation route. J Magn Magn Mater 2022;564:170091.

6. Cheraghipour E, Javadpour S, Mehdizadeh AR. Citrate capped superparamagnetic iron oxide nanoparticles used for hyperthermia therapy. J Biomed Sci Eng 2012; 2012:715–9.

7. Rahman OU, Mohapatra SC, Ahmad S. Fe3O4 inverse spinal super paramagnetic nanoparticles. Mater Chem Phys 2012;132:196–202.

8. Bertorelli R, Botella P, Nieciecka D, R˛ Ekorajska A, Cichy D, Kó P, et al. Synthesis and Characterization of Magnetic Drug Carriers Modified with Tb3+ Ions. Nanomaterials 2022, 12, 795 2022; 12:795.

9. Noqta OA, Sodipo BK, Aziz AA. One-pot synthesis of highly magnetic and stable citrate coated superparamagnetic iron oxide nanoparticles by modified coprecipitation method. Functional Composites and Structures 2020 ; 2:045005.

10. Oh J, Feldman MD, Kim J, Condit C, Emelianov S, Milner TE. Detection of magnetic nanoparticles in tissue using magneto-motive ultrasound. Nanotechnology 2006; 17:4183.

11. Mehrmohammadi M, Oh J, Ma L, Yantsen E, Larson T, Mallidi S, et al. Imaging of iron oxide nanoparticles using magneto-motive ultrasound. Proc IEEE Ultrason Symp 2007; 652–5.

12. Chen Z. Size and Shape Controllable Synthesis of Monodisperse Iron Oxide Nanoparticles by Thermal Decomposition of Iron Oleate Complex.2012;42:1040–6.

13. Xu C, Sun S. Monodisperse magnetic nanoparticles for biomedical applications. Polym Int 2007; 56:821–6.

14. Park J, An K, Hwang Y, Park JEG, Noh HJ, Kim JY, et al. Ultra-large-scale syntheses of monodisperse nanocrystals. Nature Materials 2004;3:891–5.

15. Xu C, Sun S. Monodisperse magnetic nanoparticles for biomedical applications. Polym Int 2007;56:821–6.

16. Arsalani S, Oliveira J, Guidelli EJ, Araujo JFDF, Wiekhorst F, Baffa O. Synthesis of radioluminescent iron oxide nanoparticles functionalized by anthracene for biomedical applications. Colloids Surf A Physicochem Eng Asp 2020;602:125105.

17. Hufschmid R, Arami H, Ferguson RM, Gonzales M, Teeman E, Brush LN, et al. Synthesis of phase-pure and monodisperse iron oxide nanoparticles by thermal decomposition. Nanoscale 2015 ;7:11142–54.

18. Hadadian Y, Masoomi H, Dinari A, Ryu C, Hwang S, Kim S, et al. From Low to High Saturation Magnetization in Magnetite Nanoparticles: The Crucial Role of the Molar Ratios between the Chemicals. ACS Omega 2022; 7:15996–6012.

19. Luo B, Song XJ, Zhang F, Xia A, Yang WL, Hu JH, et al. Multi-functional thermosensitive composite microspheres with high magnetic susceptibility based on magnetite colloidal nanoparticle clusters. Langmuir 2010; 26:1674–9.

20. Mahdavi M, Ahmad M bin, Haron MJ, Namvar F, Nadi B, Ab Rahman MZ, et al. Synthesis, Surface Modification and Characterisation of Biocompatible Magnetic Iron Oxide Nanoparticles for Biomedical Applications. Molecules 2013, 18, 7533-7548.

21. Nikoobakht B, Wang ZL, El-Sayed MA. Self-Assembly of Gold Nanorods. Journal of Physical Chemistry B 2000; 104:8635–40.

22. Wang L, Jiang X, Ji Y, Bai R, Zhao Y, Wu X, et al. Surface chemistry of gold nanorods: origin of cell membrane damage and cytotoxicity. Nanoscale 2013; 5:8384–91.

23. Chen YS, Frey W, Kim S, Kruizinga P, Homan K, Emelianov S. Silica-coated gold nanorods as photoacoustic signal nanoamplifiers. Nano Lett 2011; 11:348–54.

24. Chen YS, Frey W, Kim S, Homan K, Kruizinga P, Sokolov K, et al. Enhanced thermal stability of silica-coated gold nanorods for photoacoustic imaging and image-guided therapy. Optics Express, 18:8867–78.

25. Vega MS, Brisset F, Laurent G. Optimized Silica Shell Synthesis Surrounding Gold Nanorods for Enhanced Spectroscopies. Plasmonics 2021; 16:635–42.

26. Ye X, Zheng C, Chen J, Gao Y, Murray CB. Using binary surfactant mixtures to simultaneously improve the dimensional tunability and monodispersity in the seeded growth of gold nanorods. Nano Lett 2013; 13:765–71.

27. Pellas V, Blanchard J, Guibert C, Krafft JM, Miche A, Salmain M, et al. Gold Nanorod Coating with Silica Shells Having Controlled Thickness and Oriented Porosity: Tailoring the Shells for Biosensing. ACS Appl Nano Mater; 4:9842–54.

28. Wu WC, Tracy JB. Large-scale silica overcoating of gold nanorods with tunable shell thicknesses. Chemistry of Materials 2015; 27:2888–94.

29. Abbasian M, Mahmoodzadeh F, Salehi R, Amirshaghaghi A. Chemo-photothermal therapy of cancer cells using gold nanorod-cored stimuli-responsive triblock copolymer. New Journal of Chemistry 2017 ; 41:12777–88.

30. Tsutsui Gen Tsutsui G, Huang Shujuan Huang S, Sakaue Hiroyuki Sakaue H, Dong Pham V, Hoang H, et al. Synthesis and optical properties of colloidal gold nanoparticles. J Phys Conf Ser 2009; 187:012026.

31. Yu C, Varghese L, Irudayaraj J. Surface modification of cetyltrimethylammonium bromide-capped gold nanorods to make molecular probes. Langmuir 2007; 23:9114–9.

32. Lewinski N, Colvin V, Drezek R. Cytotoxicity of Nanoparticles. Small 2008; 4:26–49.

33. Pujalté I, Passagne I, Brouillaud B, Tréguer M, Durand E, Ohayon-Courtès C, et al. Cytotoxicity and oxidative stress induced by different metallic nanoparticles on human kidney cells; 8:1–16.

34. Abakumov MA, Semkina AS, Skorikov AS, Vishnevskiy DA, Ivanova A v., Mironova E, et al. Toxicity of iron oxide nanoparticles: Size and coating effects. J Biochem Mol Toxicol 2018; 32:e22225.

35. Balivada S, Rachakatla RS, Wang H, Samarakoon TN, Dani RK, Pyle M, et al. A/C magnetic hyperthermia of melanoma mediated by iron/iron oxide core/shell magnetic nanoparticles: A mouse study. BMC Cancer 2010; 10:1–9.

36. Yu M, Huang S, Yu KJ, Clyne AM. Dextran and Polymer Polyethylene Glycol (PEG) Coating Reduce Both 5 and 30 nm Iron Oxide Nanoparticle Cytotoxicity in 2D and 3D Cell Culture. International Journal of Molecular Sciences 2012,13, 5554-5570.